Modification of a Dilution Refrigerator for In-Field SQUID Magnetometry of $Dy_2Ti_2O_7$

by

Christopher Ian Mitchelitis

A thesis
presented to the University of Waterloo
in fulfillment of the
thesis requirement for the degree of
Master of Science
in
Physics

Waterloo, Ontario, Canada, 2015

I hereby declare that I am the sole author of this thesis. This is a true copy of the thesis, including any required final revisions, as accepted by my examiners.

I understand that my thesis may be made electronically available to the public.

Abstract

The pyrochlore oxide family is a well known class of geometrically frustrated magnets with novel properties such as residual entropy at low temperatures and monopole-like quasiparticle excitations. One member of this family, $Dy_2Ti_2O_7$, is a well characterized material with both theoretical and experimental agreement for the dipolar spin ice model [38]. One consequence of this model are the ice rules, where due to local $\langle 1\,1\,1\rangle$ Ising like anisotropy, and ferromagnetic dipolar coupling between spins in the magnetic ion sublattice, it is energetically favorable for two spins to point into the center of each tetrahedra and two to point out [19]. This simple rule is simultaneously the cause of the residual entropy, and the cause of monopole-like quasi-particle excitations. These properties of the spin ice state have been measured extensively in $Dy_2Ti_2O_7$, and have been accurately quantified through a.c. susceptibility [64, 50, 35, 36, 57] and heat capacity measurements [48] from high temperature down to 1 K. Below 1 K, there is still work to be done in these materials, for example, explaining a recent heat capacity result which suggest an ordered state in $Dy_2Ti_2O_7$ at low temperature [46], and the development of a consistent theory behind the Arrhenius relaxation seen in a.c. susceptibility measurements below 1 K [64].

In addition to the interesting behavior of the spin ice state in zero applied magnetic field, there exists the possibility of the Kagome ice state forming in these materials when a magnetic field is applied along the [1 1 1] crystallographic direction [54, 21]. The Kagome ice state has been reported to have many interesting properties, with many of these being measured in $Dy_2Ti_2O_7$; for example, two plateaus in the magnetization along the [1 1 1] direction for different applied magnetic fields along [1 1 1] [54], and multiple heat capacity peaks at low temperatures [21]. One measurement that isn't well characterized is the a.c. susceptibility in the Kagome ice state, and so for this purpose, a dilution refrigerator was successfully modified for in-field SQUID susceptibility measurements using a Niobium SQUID gradiometer with a 8.5 T superconducting magnet. With the modifications in place, the dilution fridge reached a temperature below 10 mK, with in-field temperature control better than 1 part in 10,000 below 100 mK.

A full characterization of the new setup was performed through a zero field a.c. susceptibility measurement of $Dy_2Ti_2O_7$. This measurement was done between 525 mK and 1.2 K, in a bandwidth of 1 mHz to 1 kHz, and the results are compared to previously published work. Next, the magnetic field was turned on, and the fridge was found to be capable of taking SQUID susceptibility data in a 1 T field, thus achieving the ultimate goal of the design. In-field a.c. susceptibility was measured on the same $Dy_2Ti_2O_7$ crystal as the zero field data between 625 mK and 1.2 K, with fields between 0.4 T and 1 T along [1 1 1], in a bandwidth of 10 mHz to 1 kHz.

It was found that the zero field a.c. susceptibility data qualitatively reproduced the results of previous measurements in the Arrhenius region below ~ 1 K, with the main difference being that the barrier to relaxation was 10.9 K $\pm$ 0.3 K for this sample as opposed to the 9.79 K [64] and 9.19 K $\pm$ 0.34 K [50, 49] measured previously. The full-width-half-max of the χ'' peaks were found to be between 1.4-1.7 decades in the Arrhenius region, in agreement with the previously measured 1.35-1.6 decades on a different $Dy_2Ti_2O_7$ sample [64]. In addition, the dynamical correlation functions of the a.c. susceptibility data were calculated and were found to have the same stretched exponential form at short times, leading into an algebraically long time tail at longer times, as was measured in $Dy_2Ti_2O_7$ previously [50]. The stretch factors of the stretched exponential region were found to be between 0.73-0.77, in agreement with the previously measured 0.7-0.8 [50]. These results showed the accuracy of the new dilution refrigerator setup in zero field, and showed that the theory which best describes the a.c. susceptibility data in the low temperature Arrhenius region is still the theory developed in [50].

It was found that the magnetic relaxation frequencies of $Dy_2Ti_2O_7$ decreased in value as the magnetic field was increased along [1 1 1] for all temperatures measured. The relaxation frequencies dropped by almost a decade in frequency compared to the zero field data at the highest field measured, 1 T. Arrhenius relaxation was observed below 1 K at 400 mT, 500 mT, 600 mT, and 700 mT, with the same barrier to relaxation of approximately 10.9 K as the zero field barrier. The existence of an Arrhenius relaxation regime in the Kagome ice state can be deduced from current theoretical models, however a barrier to relaxation that is the same as the zero field barrier, and also attempt frequencies which steadily drop in value as the field increases along [1 1 1], are interesting results. The increase in the characteristic relaxation times was found to fit to an exponential as a function of applied field, suggesting a modification to the equation derived in [50] for the relaxation times in this regime in $Dy_2Ti_2O_7$.

Finally, a heat capacity measurement of the double peak superconducting transition of the f-wave superconductor UPt_3 was performed on the new dilution refrigerator setup. This was done between 250 mK and 650 mK, in order to quantify its low temperature heat capacity capabilities. The results are shown in Appendix A. The data was found to be extremely clean, with voltage noise on the thermometer connected to the UPt_3 crystal limited by the low noise preamplifier used to measure its resistance value. The double peak superconducting transition was resolved, and the main properties of the transition were found to agree with previously measured results on UPt_3.

Acknowledgements

Dedication

I dedicate this thesis to my family, who provided me with the drive needed to see this through to the end.

Table of Contents

List of Tables

List of Figures

Chapter 1

Introduction

Frustration is a well studied property in many different materials. In frustrated materials, competing interactions, which individually have unique ground states configurations that minimize the total system energy, have interaction energy scales on the order of each other. When this occurs, the system can result in no unique ground state configuration, usually when subject to certain geometrical constraints. One of the first experimental observations of frustration arose in the proton configurations in the hexagonal phase of water ice [17, 43]. These interactions can have many origins, with the usual cause of frustration being electromagnetic interactions on a unique geometric lattice. Many of the novel properties associated with frustrated materials take shape at low temperatures, where the system is forced to enter into a highly degenerate ground state, resulting in novel properties such as finite entropy at zero temperature, called residual entropy. In frustrated magnets, magnetic interactions between spins in a material are the cause of the frustration. The study of frustration in spin glass, spin liquid, and spin ice materials is motivated by the potential application of the theories to other systems with numerous ground state configurations.

In recent years there has been much interest in the magnetic properties of the pyrochlore oxide family, with chemical equation $R_2B_2O_7$. When a trivalent rare earth ion such as Dy^{3+} is placed on the R site and a non-magnetic tetravalent ion such as Ti^{4+} is placed on the B site, these materials can exhibit many interesting properties at low temperatures; such as residual entropy attributed to magnetic frustration caused by competing dipolar and anti-ferromagnetic interactions on the pyrochlore lattice [19]. Such a model is called the dipolar spin ice model, and materials following these dynamics are called dipolar spin ice, with $Dy_2Ti_2O_7$ being a well studied member. The dipolar spin ice model leads to ground state excitations in the form of fractionalization of magnetic moments into monopole quasipar-

ticle defects [10]. These low temperature dynamical properties have been studied in great detail through heat capacity measurements [25], neutron scattering [40], thermal transport [27], magnetization [50], and a.c. susceptibility [64] in the last few years. A multitude of questions remain open in the study of these magnetically frustrated pyrochlore oxides, with most pertaining to deviations from theoretical models at low temperatures ($T \lesssim 1K$). Two important examples of this are the recent measurement of deviation in the residual entropy of $Dy_2Ti_2O_7$, known as Pauling's entropy, at low temperatures [46], and the lack of a consistent theoretical model predicting the value of parameters measured in the low temperature Arrhenius ($T \lesssim 1K$) region in a.c. susceptibility measurements [64]. An interesting phenomena can occur in these materials when a large magnetic field is applied along the [111] crystallographic direction of the pyrochlore structure, the development of a phase dubbed the Kagome ice state. The phase is best explained by realizing the pyrochlore structure can be viewed as stacked layers of triangular lattice planes and Kagome lattice planes along the [1 1 1] direction. As the field is increased, 3 spins in each tetrahedron of the pyrochlore lattice minimize their Zeeman energy by having a spin component pointing towards the applied field direction, however one spin has a component opposing the applied field. This field opposing spin is minimizing its energy with respect to the effective exchange between spins in the tetrahedra. In $Dy_2Ti_2O_7$, this arrangement occurs near a field value of 0.5 T. At this field value, the spins in the triangular layers are pinned to point along the direction of the applied field, and magnetization measurements have shown this results in a plateau in the magnetization along [1 1 1] [54]. In this plateau region, the Kagome ice state exists, and the system becomes frustrated in a 2-D Kagome lattice with the ice rules still being obeyed. This phase has been measured experimentally in $Dy_2Ti_2O_7$ [54], $Ho_2Ti_2O_7$ [44] and $Tb_2Ti_2O_7$ [31].

The focus of this thesis will be on a.c. susceptibility measurements of $Dy_2Ti_2O_7$, which are an intuitive way to probe the dynamics of a system with such complex spin interactions. The leading model for the low temperature Arrhenius region of the a.c. susceptibility is that developed in [50]. Here, the dynamics in this region are attributable to a complex interaction of monopoles with crystal impurities. The a.c. susceptibility in the Arrhenius region should then drastically change as the system is moved into the Kagome ice state, where monopole excitations become confined to 2-D sheets, and this could result in some very interesting properties. Motivated by this, the goal of this thesis was to modify a dilution refrigerator setup for in-field a.c. susceptibility measurements to quantify the a.c. susceptibility in the low temperature, Arrhenius region of $Dy_2Ti_2O_7$ in the Kagome ice state.

Chapter 2 of this thesis will discuss the theory behind dilution refrigerators for a reader not familiar with their operation, since the design of a new dilution refrigerator setup was

such a critical part of the research in this thesis. Chapter 3 will discuss the theory behind spin ice and Kagome ice, also explaining some recent results in the theory of monopole excitations in $Dy_2Ti_2O_7$. Chapter 4 will explain the experimental details of the measurement made in this thesis. First, the design and installation of all new components on a dilution refrigerator setup in order to take in-field a.c. susceptibility and heat capacity data. Next, the use of a Niobium SQUID gradiometer to take a.c. susceptibility data on $Dy_2Ti_2O_7$ both in zero field and in-field. Chapter 5 will explain the experimental results of the a.c. susceptibility measurement on $Dy_2Ti_2O_7$, first in zero field, then in-field. The zero field data was compared to literature in order to characterize a new $Dy_2Ti_2O_7$ sample, and also show the accuracy of the new dilution refrigerator setup. Next, a magnetic field was applied along the [1 1 1] direction of the $Dy_2Ti_2O_7$ material, causing it to move into the Kagome ice state, and the a.c. susceptibility was measured. This was done between 625 mK and 1.2 K, in fields between 400 mT and 1 T along [1 1 1], and these results are compared to the zero field results. The in-field results are explained to have important implications to future theories of monopoles in the Kagome ice state, and they have important experimental consequences to heat capacity measurements in the Kagome ice state of $Dy_2Ti_2O_7$. Appendix A covers some of the theory of the unconventional f-wave superconductor UPt_3, and shows a specific heat measurement made on a high quality crystal of this material on the new dilution refrigerator setup. The double peak superconducting transition of this material was resolved which showed the accuracy of the specific heat measurement, and the results are compared to other literature.

Chapter 2

Dilution refrigerators

2.1 Theory

$^3He/^4He$ dilution refrigerators have been around since the 50s/60s, and have proven to be a reliable way to reach millikelvin (mK) temperatures in a reasonable time frame for a reasonable cost. There are many other options available for cooling materials down to mK temperatures from room temperature, such as ^3He refrigerators and adiabatic demagnetization refrigerators, each with their own benefits. Adiabatic demagnetization refrigerators for example, are 'dry' fridges, called so because they consume no liquid Helium or liquid Nitrogen in their operation, making cooling them down much simpler. At the same time, they only provide around 1/100th the cooling power of a standard dilution fridge, and can only stay cold for ~ 1 day before the sample stage needs to be warmed and re-cooled. ^3He refrigerators are usually 'wet' fridges, which need liquid Helium and liquid Nitrogen to operate. Depending on whether the fridge is designed as a one-shot or a continuous flow operating fridge, these can stay cold for a few days to indefinitely respectively. In the case of a $^3He/^4He$ dilution refrigerator, you get the best of all the specs at an increased operational cost and complexity to the operation. This is offset by the ability to reach mK temperatures for indefinite periods, at the expense of high liquid Helium costs which are dependent on the Helium boiloff of the fridge and Helium dewar. For example, a 10 L/day boiloff rate for a dilution fridge setup (as the one set up in this thesis), can be filled with ~ 80 L of liquid helium from a standard 100 L helium storage dewar within an hour, and run for 8 days continuously, with little to no change to the sample stage temperature. The liquid Helium bath is necessary for cooling the vacuum can and incoming pipes from room temperature down to near 4 K (with some temperature gradient along the way), and also

to run the 1 K Pot of the fridge, which will be explained later. Nowadays there are dilution refrigerators which combine pulse tube cooler technology to precool the incoming $^3He/^4He$ gas which allows for cryogenic liquid free ('dry' fridge) and continuous mode operation, at the expense of vibrational noise in the system.

Much of which fridge to choose for a specific application depends on how low a temperature you want, what cooling power you want at that temperature, how long you need to stay there for a data set, how isolated you need the setup to be from noise sources, and how expensive each setup is. Frustrated magnetic materials exhibit many novel dynamics in the low mK temperature range, and from 1 K down have internal thermal time constants on the order of many hours to possibly days, as measured through magneto-caloric measurements [46]. Thus, the only option available for a thorough study of these materials is the dilution refrigerator option, and in this thesis, a 'wet' dilution fridge setup was built. Only this type of fridge will be discussed below. For more in-depth theory than what is presented here, suggested reading is Pobell [45] and Richardson and Smith [52].

$^3He/^4He$ dilution refrigerators take advantage of an endothermic reaction, the mixing of ^3He into a diluted $^3He/^4He$ mixture, at low temperatures. In Figure 2.1, we have the phase diagram of the λ-transition of superfluid ^4He in $^3He/^4He$ mixtures of various ^3He concentrations. At around 870 mK, a phase separation occurs between normal fluid ^3He and ^4He, and superfluid ^4He with Fermi liquid ^3He. At very low temperatures, much of the lighter ^3He exists in a pure phase on top of a diluted $^3He/^4He$ phase due to the difference in density of the two mixtures, and the concentration of ^3He varies in the diluted phase with temperature. A very unique thing happens in the diluted phase at low temperatures, namely, there exists a finite solubility of ^3He in ^4He, even in the limit of $T \to 0$, with a value close to 6.6% ^3He [63]. This property isn't explained classically, and relies on the quantum mechanical properties of ^3He and ^4He.

Below the λ transition, ^4He is a superfluid, which means the bosonic ^4He atoms condense into their Bose-Einstein condensate ground state. At these low temperatures, the ^3He atoms have a ground state defined by a system of interacting fermions. The Van der Waals potential between the ^3He atoms is the same as that for the ^4He atoms, however the ^3He atoms have a smaller mass, resulting in larger zero-point motion for ^3He versus ^4He. This means that the ^3He atoms are closer to the ^4He atoms than to other ^3He atoms, meaning ^3He-^4He bonding has a higher energy than ^3He-^3He bonding. This means that even as $T \to 0$, ^3He will dissolve in ^4He, resulting in the 6.6% concentration minima. In addition to this, according to Landau two-fluid theory, the concentration of superfluid ^4He increases as the temperature decreases, meaning more ^3He atoms become bound to ^4He atoms as the temperature is lowered, and thus the distance between ^3He atoms becomes larger. In this model, at low temperatures the ^4He forms a superfluid background which
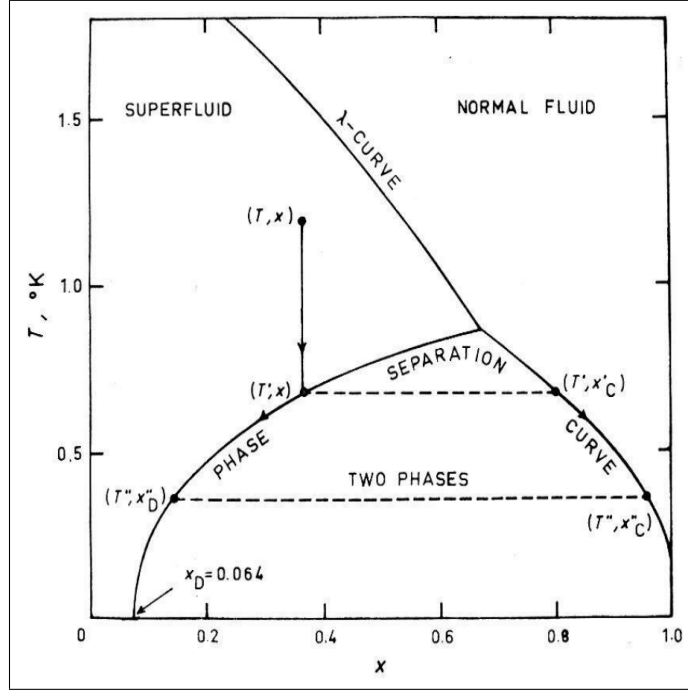
Figure 2.1: The phase diagram of the λ-transition in ${}^3He/{}^4He$ mixtures as a function of temperature and concentration of ${}^3He$. From [32].

causes the ${}^3He$ atoms to separate to the point where they act as a Fermi liquid with an effective mass that varies slightly with the concentration of ${}^3He$, but is very close to the mass of ${}^3He$ ($m^\star = 2.5m_{{}^3He}$); i.e. a Fermi gas. Within this model, the heat capacity in the dilute phase is the heat capacity of a nearly ideal Fermi gas (since the ${}^4He$ contribution is minimal due to Bose-Einstein condensation), and the heat capacity of the high concentration ${}^3He$ phase is the heat capacity of a Fermi liquid. Thus, there is a difference in heat capacity between the dilute phase and the concentrated phase, which results in a difference in the entropy of the two phases. The heat capacity in the dilute phase can be calculated using the fact that the Fermi temperature of the dilute phase is 0.38 K at a concentration of 6.6% ${}^3He$, and is well described by a Fermi gas [45]. The heat capacity of the concentrated phase has been measured experimentally [45]. Using these values one finds the heat capacity goes as $106T\frac{J}{mol_{He^3}K}$ in the dilute phase and $22T\frac{J}{mol_{He^3}K}$ for the concentrated phase, both at low temperatures. Since both materials follow $C \sim T$, the enthalpy difference between the two phases at the phase boundary can be calculated easily, this is done in Equation 2.1.

6

$$\Delta H = T(S_D - S_C) = T(\int_0^T \frac{C_D}{T}dT + \int_0^T \frac{C_C}{T}dT) = 106T^2 - 22T^2 = 84T^2 \frac{J}{mol_{He^3}K} \quad (2.1)$$

As can be seen, the enthalpy of mixing at low temperatures is positive in value, meaning the mixture of ^3He into the $^3He/^4He$ diluted phase is an endothermic reaction. A combination of this mixing being endothermic, and the solubility of ^3He into ^4He being finite even in the limit of $T \to 0$, means that this mixing results in cooling all the way down to $T \to 0$, and can be done indefinitely due to the finite solubility. These two facts are the key behind what makes a dilution refrigerator work. Also, the cooling power is proportional to T^2 for the dilution process, where as it is proportional to $e^{\frac{1}{T}}$ for evaporative cooling found in ^3He fridges for example. Thus, in the limit of very low T, it is able to beat out evaporative cooling processes in terms of cooling power, and therefore base temperature.

2.2 Standard operation

To take advantage of the cooling effect described above, the dilution refrigerator design comes into play. The dilution refrigerator consists of 5 main components which act together in such a way as to form the $^3He/^4He$ phase boundary inside of the mixing chamber, and also to send pure ^3He through this phase boundary to provide cooling. These 5 components are the 1 K pot, the mixing chamber, the still, the counterflow heat exchangers, and finally the impedances. A typical dilution refrigerator setup is shown in Figure 2.2.

Before any $^3He/^4He$ mixture is sent into the dilution fridge it is cooled to 4.2 K and sits in vacuum so that the heat loads on all of the different components of the fridge are not so high that they prevent the dilution fridge from running. The fridge is sealed in a vacuum can and pumped to zero pressure where it is then surrounded by an exchange gas between the vacuum can and fridge which has a low freezing temperature (Neon at $\sim 20K$ for example). This exchange gas is used to provide thermal conductivity between the fridge and the bath space, which is then cooled to 77 K by having the whole area outside of the vacuum can sit inside of a dewar filled with liquid Nitrogen. Liquid Nitrogen has a larger latent heat than liquid Helium by a factor of about 60, and in addition, liquid Nitrogen is about 10 times cheaper, making it more economical to use over liquid Helium to cool from 300 K to 77 K. Most of the heat capacity of the various materials used on the dilution fridge (Copper, stainless steel, etc), is removed by the liquid Nitrogen pre-cooling so the liquid Helium transfer is much more efficient (less liquid is evaporated into gas to cool the
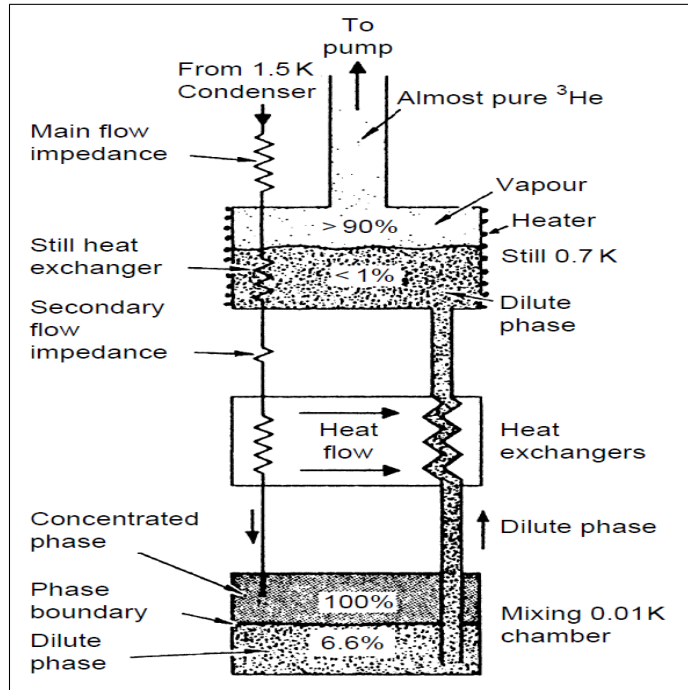
Figure 2.2: A standard 'wet' dilution refrigerator setup, from [45].

fridge). The liquid Nitrogen is then removed from the bath space through a blow-out tube, and liquid Helium is slowly transferred into the bath space. The transfer is done slowly to take advantage of not only the latent heat of ^4He but also its enthalpy change going from 4 K to 300 K. Once the whole fridge has equilibrated to a temperature of 4.2 K, the exchange gas has frozen out, and the mix can now be sent into the fridge.

The $^3He/^4He$ mixture is first sent into the dilution unit through the 'return' side of the fridge. The mixture passes through the 1 K pot where the mix is cooled to around 1 K, which removes the heat of condensation from the $^3He/^4He$ mix liquefying. The 1 K pot is a volume with an impedance leading to the main ^4He bath space through a filter, which continually fills as the ^4He inside the volume is pumped on. At a vapor pressure of around 1 mbar, achieved by pumping on the volume with an external pump, the 1 K pot sits at around 1 K. The $^3He/^4He$ mixture is then sent through the primary impedance which is usually a fine capillary tube designed to impede the incoming $^3He/^4He$ mix to the point where the return side pressure is in the range of a few hundred mbar, which guarantees liquification of the ^3He at the temperature of the 1 K pot, around 1 K. Next, the mix passes through a heat exchanger connected to the still, which sits at around 500-800 mK. The

8

still cools the incoming gas, and it then travels to a secondary impedance which is there to prevent re-evaporation of ^3He. The mix then passes through a second heat exchanger for more precooling, which is thermally connected to cold gas coming out of the dilute phase inside the mixing chamber to the still. Next, the mix flows into the mixing chamber where the two phases of the $^3He/^4He$ mix reside. An osmotic pressure difference is created by the differing concentrations and differing temperatures of the $^3He/^4He$ mix inside the mixing chamber and the still. This pressure drives pure ^3He through the concentrated phase into the dilute phase, creating cooling at the mixing chamber. A tube connects the diluted phase to the still, with a set of heat exchangers as mentioned before, which cool the mix leading into the mixing chamber. In the still, there sits more $^3He/^4He$ mix, and now a second property of ^3He and ^4He is exploited, namely ^3He has a higher vapor pressure than ^4He at the still temperature of roughly 0.5-0.7 K. This means, that if the still side is pumped on, then mostly ^3He will evaporate and not ^4He if the correct pressure is maintained. This allows nearly pure ^3He to be pumped away from the still, generating a strong osmotic pressure difference which drives the mixing in the mixing chamber, and also allows for the ^3He to be pumped away and recirculated into the return side of the fridge. This dilution process can be repeated indefinitely, creating a cycle of cooling which holds down to $T \to 0$.

There are very technical details to the operation and construction of dilution refrigerators, such as how heat exchangers are designed, but the above description describes the important characteristics of most 'wet' dilution refrigerators. Once a dilution unit has been built and tested, the quality of data produced by it is determined by the design of the various components connected to it. This includes deciding how to shield the unit from various noise sources, and reducing heat loads on the 1 K pot, still, and mixing chamber. Radiation shielding, heat sinking, temperature control, vibration isolation, electromagnetic field shielding, and low dewar boiloff are important design characteristics which really separate one dilution refrigerator from all the rest. In this thesis, a new dilution refrigerator setup was designed trying to optimize the above features for in-field heat capacity and a.c. susceptibility measurements, and was used to study the magnetically frustrated spin ice material $Dy_2Ti_2O_7$, a material which is described in depth next.

Chapter 3

Spin ice and Kagome ice

3.1 Magnetic frustration and spin ice

3.1.1 Theory

Magnetic frustration is a general term used to describe systems whereby a combination of magnetic interactions, and other constraints such as geometry, create ground state complexities. One typical sign of frustration is a large ground state degeneracy, which results in residual entropy. Consider the classical example of magnetic frustration, a system of anti-ferromagnetically coupled Ising spins on a 2-D triangular lattice, shown in Figure 3.1. As one can see in (a), since the spins are Ising like, they can only point up or down, but due to anti-ferromagnetic interactions, they also want to point opposite to each other to minimize their energy. Two spins in each triangle can anti-align but the third one cannot decide between pointing up or down, as both cost the same energy. Thus, the system has a degeneracy owing to the Ising nature of the spins and the anti-ferromagnetic interaction; in other words, the system is magnetically frustrated as it cannot decide what state to go into to minimize total energy. This degeneracy grows with system size (number of triangles), and has a ground state entropy of 0.323R [62], which persists down to zero temperature, called a residual entropy. For comparison, in the same figure, (b) and (c) show there are only 2 possible ground states if the spins are instead classical vector spins with the same geometry and exchange interaction which shows the importance of needing all of the 3 features, the Ising nature, the exchange nature, and also geometry to have the magnetic frustration in this case. The concept of residual entropy was first measured experimentally in water ice, whose ground state degeneracy arises from proton configurations in the

hexagonal phase [43]. In this phase, each O^{2-} ion is surrounded by four other O^{2-} ions in a tetrahedral fashion, with four covalently bonded protons (H^+ ions) that sit between O-O bonds. Two of these protons are forced to be 'near' to the O^{2-} ion, and two are forced to be 'far' owing to the interactions in H_2O, which result in the Bernal-Fowler ice rules [19]. The protons being forced into two-near and two-far configurations throughout the whole tetrahedral lattice results in a large entropy which can be estimated as follows. Each O-O bond can have either a near or far proton, and for N O^{2-} ions there are 2N unique bonds, so in total there are 2^{2N} possible proton configurations for the whole system. Of the 2^4 configurations of protons around each O^{2-}, only 6 are energetically favorable, so there is a 6-fold degeneracy, reducing the number of configurations per proton by a weighting of $\frac{6}{2^4} = \frac{3}{8}$ per O^{2-} ion. Thus, the total number of configurations is $2^{2N}(\frac{3}{8})^N = (\frac{3}{2})^N$ giving a configurational residual entropy of $S(T = 0) = k_B ln((\frac{3}{2})^N) = Rln(\frac{3}{2})$. This residual entropy of $Rln(\frac{3}{2})$ is given the name Pauling's Entropy, after the 1935 result by Pauling [43], which was later measured to be within $1 - 2\%$ of the experimental value [17]. Water ice was one of the first examples of a system exhibiting residual entropy, however it is not due to magnetic frustration. A similar type of degeneracy is seen however in the pyrochlore oxide family, which arises from magnetic frustration.
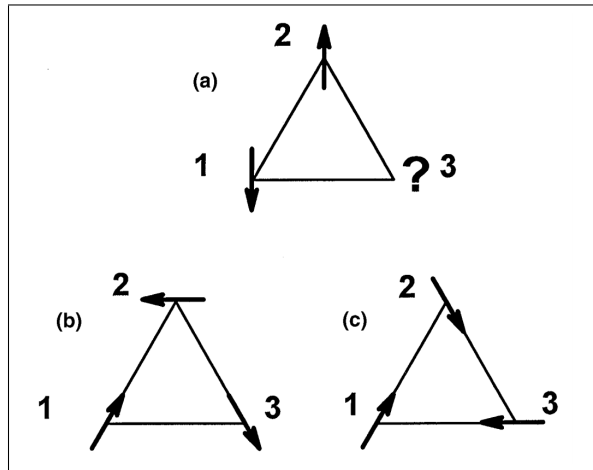
Figure 3.1: The anti-ferromagnetically coupled Ising spins on the triangular lattice (a). In (b) and (c), we have the two degenerate ground states for classical vector spins on the 2-D triangular lattice. This shows the importance of not only the anti-ferromagnetic exchange, but also the geometry of the problem, and the importance of Ising-like spins. From [13].

The pyrochlore oxides are a family of materials with chemical equation $R_2B_2O_7$, where both R and B can be magnetic or non-magnetic ions. The pyrochlore lattice is face centered

cubic with a tetrahedral basis cell of four sites, and can be viewed as a lattice of corner sharing tetrahedra. The R and B ions form two pyrochlore sublattices in the face centered cubic structure. One subclass of these materials is the insulating pyrochlore oxides where the R ion is chosen to be a rare earth ion such as Dy^{3+} or Ho^{3+}, and B is a non-magnetic ion such as Ti^{4+}. This subclass is the focus of the work presented in this thesis, specifically, the case of R being a Dy^{3+} ion and B being a Ti^{4+} ion, resulting in the pyrochlore oxide known as $Dy_2Ti_2O_7$. In this case, any reference to the pyrochlore lattice refers to the sublattice of the magnetic Dy^{3+} ions. Magnetic frustration arises from anti-ferromagnetic exchange and ferromagnetic dipolar interactions between spins on the pyrochlore lattice, and Ising anisotropy along the local $\langle 1\,1\,1 \rangle$ axis caused by crystal field effects. The model that describes this system is known as the dipolar spin ice model, as shown in [16], with hamiltonian given by Equation 3.1.

$$H = -J \sum_{<i,j>} S_i^{z_i} \cdot S_j^{z_j} + Dr_{nn}^3 \sum_{j>i} [\frac{S_i^{z_i} \cdot S_j^{z_j}}{|r_{ij}|^3} - \frac{3(S_i^{z_i} \cdot r_{ij})(S_j^{z_j} \cdot r_{ij})}{|r_{ij}|^5}] \qquad (3.1)$$

The spin of the Dy^{3+} ions, namely $J_{Dy} = \frac{15}{2}$, results in a $(2J_{Dy}+1)$ fold degeneracy to the possible electronic ground state of the Dy^{3+} ions, which could complicate the solution to the above Hamiltonian considerably. It has been found however that crystal field excitations lift this degeneracy with a crystal field gap energy of $\sim 200K$ and result in a pure $\left| J = \frac{15}{2} | m_J = \pm\frac{15}{2} \right\rangle$ ground state doublet along the local $\langle 1\,1\,1 \rangle$ direction. In other words, the Dy^{3+} spins on the corners of the tetrahedra in the pyrochlore lattice are Ising-like, and either point 'in' or 'out' along the local $\langle 1\,1\,1 \rangle$ direction [19]. Using this fact, one can then write down the dipolar spin ice model in terms of components pointing along the local $\langle 1\,1\,1 \rangle$ direction, which is along z_i for Equation 3.1. In addition to this, looking at Equation 3.1, there is an exchange term J and a dipolar term D which both compete to determine the nature of the effective exchange between the spins on the tetrahedra. In $Dy_2Ti_2O_7$, one can look at the competing effect of J and D within the nearest neighbor model, which upon the substitution $\hat{z}_i \cdot \hat{z}_j = -\frac{1}{3}$ and $(\hat{z}_i \cdot \hat{r}_{ij})(\hat{r}_{ij} \cdot \hat{z}_j) = -\frac{2}{3}$ for the pyrochlore lattice modifies Equation 3.1 to Equation 3.2 [19], where the terms going beyond nearest neighbor have not been included.

$$H = \sum_{<i,j>} (\frac{J}{3} + \frac{5D}{3})\sigma_i^{z_i}\sigma_j^{z_j} = J_{eff} \sum_{<i,j>} \sigma_i^{z_i}\sigma_j^{z_j} \qquad (3.2)$$

As can be seen in Equation 3.2, the hamiltonian is now that of an effective anti-ferromagnetic exchange (for $J_{eff} > 0$) with Ising variables $\sigma_i^{z_i}$ that can take on values

± 1, which has been shown to be magnetically frustrated and possess Pauling's entropy from [3]. More precisely, the residual entropy is $\frac{R}{2}ln(\frac{3}{2})$ for the spin ice state, which follows from Pauling's argument but with each of the N O^{2-} ions mapping to 2N spins when going from water ice to the spin ice state. The condition for spin ice can then be read off as $(\frac{J}{3}+\frac{5D}{3}) > 0$, or more accurately as $(\frac{J}{3}+\frac{4.53D}{3}) > 0$ when interactions past nearest neighbors are considered [19]. The term $\frac{J}{3} + \frac{5D}{3}$ is sometimes given the name J_{eff}. For $Dy_2Ti_2O_7$, $\frac{J}{3} = -1.24K$ and $\frac{5D}{3} = 2.35K$, which gives $J_{eff} = 1.11K$, thus $Dy_2Ti_2O_7$ is a spin ice at sufficiently low temperatures. J_{eff} really shows the importance of the dipolar interactions in the dipolar spin ice model because without dipolar interactions ($D = 0$), J_{eff} would be negative. A negative J_{eff} means the ground state of the system would be an ordered Néel state where the spins on the corners of the tetrahedra either point all-in or all-out [19]. $4J_{eff}$ in this dipolar spin ice picture can be interpreted as the energy to flip a spin from the 'in' state to the 'out' state in the nearest neighbor model. To summarize, the dipolar spin ice model claims that dipolar interactions compete with anti-ferromagnetic exchange causing an effective ferromagnetic exchange between spins ($J_{eff} > 0$). The system can then be shown to map to an effective anti-ferromagnetic exchange between Ising variables when considered on the pyrochlore lattice, which results in magnetic frustration [19].

3.1.2   Experiment

The dipolar spin ice model has been characterized in multiple materials now, with $Dy_2Ti_2O_7$ and $Ho_2Ti_2O_7$ being the 2 'idealized' spin ice materials. These materials differ from each other mainly in the value of J_{eff}, and a complication of nuclear hyperfine interactions in $Ho_2Ti_2O_7$. The specific heat peaks corresponding to the spin ice state for both materials are shown in Figure 3.2, with Pauling's entropy found for both materials [48, 6]. Another interesting result of the dipolar spin ice model is the idea of a phase transition to an ordered state at low temperature, predicted through monte carlo simulations using loop algorithms described in [37]. A novel computation technique called a loop algorithm was used to allow spin flips in a monte carlo simulation in a temperature range where the barriers to spin flips became much larger than the thermal energy available. This algorithm predicted a first order phase transition at low temperatures in $Dy_2Ti_2O_7$, which is shown in Figure 3.3. The full phase diagram from these dipolar spin ice model simulations, and others from [38], are shown in Figure 3.3. In [37], it is mentioned that the phase transition was not expected to be observed in $Dy_2Ti_2O_7$ due to long times associated with real spins flipping with the large thermal barriers. They also mention, that other perturbative effects H' to the dipolar spin ice hamiltonian on the order of $\frac{H'}{D_{nn}} \lesssim 0.08$, where $D_{nn} = 1.4$ K, could affect the existence of this phase transition. A phase transition was found some time later

13

in [46], close to the expected location of this phase transition found through simulations. This result is shown in Figure 3.4, where deviations from Pauling's entropy is seen, a sign of a possible phase transition. While the authors of [46] were not able to conclude that the upturn was due to the same phase transition explored through simulations in [37], it does give one possible explanation. Another possible explanation is a spin glass phase transition, which has been explored experimentally in [26]. The reason why the transition was not seen before was due to a drastic increase in the internal time constant of $Dy_2Ti_2O_7$ in the low temperature regime, with internal time constants which were found to be directly correlated to magnetic relaxation time constants found through a.c. susceptibility data. This correlation is seen in the inset in Figure 3.4 (b). This result will become important for the consequences of the in-field data measured in this thesis.

(a) $Dy_2Ti_2O_7$ specific heat   (b) $Ho_2Ti_2O_7$ specific heat
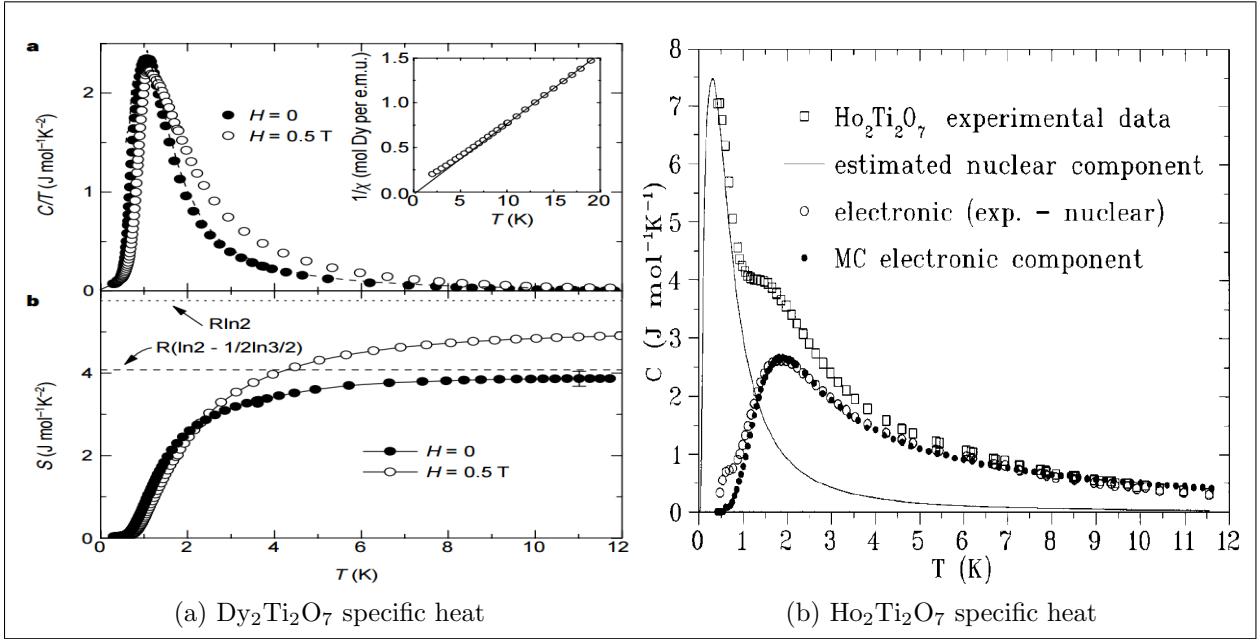
Figure 3.2: The specific heat data of [48] for $Dy_2Ti_2O_7$ (a), and the specific heat data of [6] for $Ho_2Ti_2O_7$ (b). Both data sets show a phase transition at low temperatures with an entropy equal to Pauling's entropy for spin ice.

14

(a) Loop algorithm simulation

(b) Simulated spin ice phase diagram
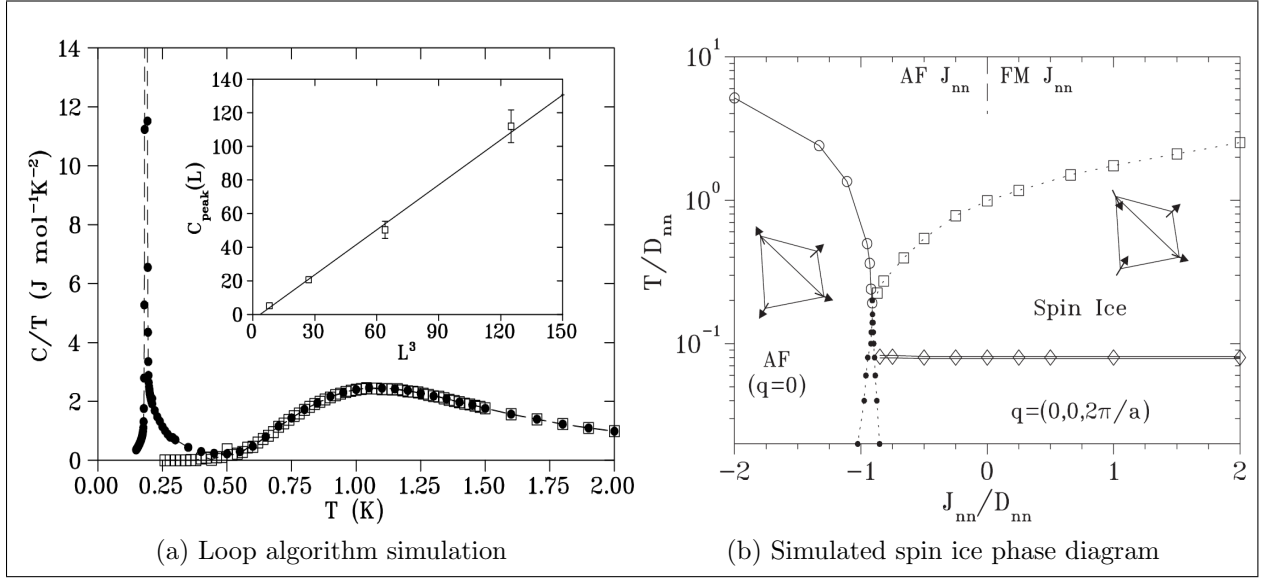
Figure 3.3: The $Dy_2Ti_2O_7$ heat capacity simulation of [37], showing a phase transition at low temperatures in (a). The dipolar spin ice phase diagram from [38] in (b).

(a) Specific heat data

(b) Thermal time constant data
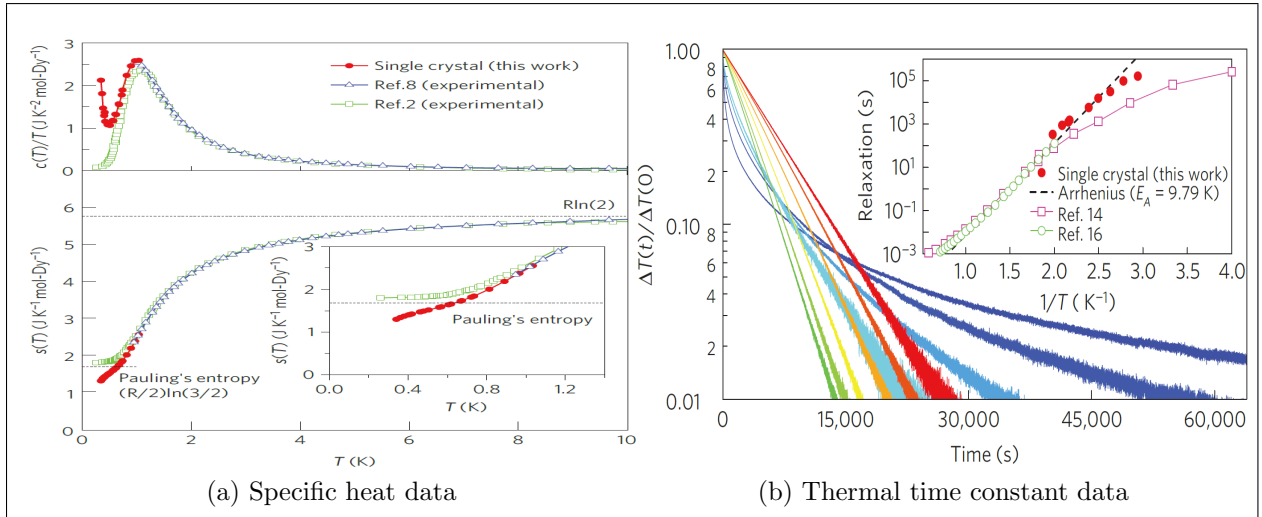
Figure 3.4: The specific heat data for $Dy_2Ti_2O_7$, from [46], in both (a) and (b). In (a), an upturn in specific heat at low temperature is seen, consistent with deviation from Pauling's entropy. This specific heat peak is close to the expected location from the simulations in [37]. In (b), the correspondence between the thermal relaxation times and magnetic relaxation times obtained through a.c. susceptibility measurements is shown, in the inset.

While the dipolar spin ice model has been very successful in explaining many of the properties found in $Dy_2Ti_2O_7$, some questions still remain. The questions relevant to this thesis pertain mostly to low temperature ($T \lesssim 1K$) behaviors measured through a.c. susceptibility. The idea of low temperature discrepancies from the dipolar spin ice model will be motivated by two a.c. susceptibility measurements done in the last couple of years in zero field. These discrepancies will then be shown to motivate the idea of magnetic monopole excitations in the next section. These two measurements are the measurements of [64] and [50], which relate to the low temperature magnetic relaxation times, and dynamical correlation functions respectively. The dynamical correlation functions, $C(t)$, are defined as $C(t) = < M(0)M(t) >$ where M is the magnetization of the sample, and t is time.

The role of the relaxation time in a system of interacting dipoles is most easily viewed in the single Debye relaxation model. In this model, the real (χ') and imaginary (χ'') components of the a.c. susceptibility (where $\chi(w) = \chi'(w) + i\chi''(w)$) are related to a characteristic relaxation time of the system denoted as τ. Such a relation is given in Equation 3.3, where χ_S represents the high frequency susceptibility (value of χ' at frequencies much larger than the characteristic relaxation time), and χ_T is the low frequency d.c. susceptibility (value of χ' at frequencies much smaller than the characteristic relaxation time). In the single Debye model, the rate of polarization of a material in a field is proportional to the polarization, through a proportionality constant τ, i.e. $\dot{P}(t) = -\frac{1}{\tau}P(t)$, which gives rise to Equation 3.3. Then, τ is interpreted as a characteristic time taken for the dipoles in the system to go between two different states of polarization. This value can be extracted from a.c. susceptibility data as $\tau = \frac{1}{2\pi f_{peak}}$ where f_{peak} is the frequency corresponding to the location of the peak of the χ'' curve. In most real systems, there is a distribution of times taken to go between these so called metastable states of polarization, usually due to magnetic disorder. This results in a broadening in the full-width-half-max value of the χ'' curve, or equivalently, as deviation from a semi-circular shape in the Argand plots of the a.c. susceptibility data, called Cole-Cole plots. In these cases, the susceptibility curves become better represented by other functional forms than the single Debye model. Some other well known functional forms are the Cole-Cole equation, the Cole-Davidson equation, the Havriliak-Negami equation, and Equation 5.2, as used in this thesis. These characteristic times have different meanings in different materials, and they usually have non-trivial dependence on temperature, field, etc., and can be used to characterize a magnetic material. One such dependence is called thermally activated Arrhenius relaxation where the relaxation time follows the functional form $\tau = \tau_0 e^{\frac{\Delta}{k_B T}}$ where Δ is called the barrier to relaxation, and τ_0 is a constant called the characteristic relaxation time, which can have a number of meanings depending on the system being studied.

$$\chi'(\omega) = \chi_S + \frac{\chi_T - \chi_S}{1 + (\omega\tau)^2}$$

$$\chi''(\omega) = \omega\tau\left(\frac{\chi_T - \chi_S}{1 + (\omega\tau)^2}\right)$$

<div align="right">(3.3)</div>

There are three regions of magnetic relaxation behavior in $Dy_2Ti_2O_7$, as found through looking at the magnetic relaxation time as a function of temperature. Above 12 K, there is an Arrhenius regime with a barrier of 200 K owed to the gap from the ground state doublet to higher level electronic states [14], where there are both Ising spins and non-Ising spins in the pyrochlore lattice. This region is well outside the data of this thesis. After this region, between $\sim$1-12 K, there is a quasiplateau region, with a initial region owed to quantum tunneling between the ground state doublet and higher level electronic configurations [14], followed by an Arrhenius region with a barrier to relaxation of $2J_{eff}$. This barrier to relaxation is owed to half the cost of flipping a spin in the nearest neighbor dipolar spin ice model [30]. The region after the quasiplateau, around $(T \lesssim 1K)$, is the least understood region. The only current explanation that agrees well with experimental data is that of monopole dynamics (which are discussed in the next section). In [64], the a.c. susceptibility of $Dy_2Ti_2O_7$ and $Ho_2Ti_2O_7$ was measured in zero field in this $(T \lesssim 1K)$ region, and it was found that the characteristic magnetic relaxation time had an Arrhenius form with an energy barrier of 9.8 K for $Dy_2Ti_2O_7$ and 10.8 K for $Ho_2Ti_2O_7$. These values correspond to $9J_{eff}$ and $6J_{eff}$ for $Dy_2Ti_2O_7$ and $Ho_2Ti_2O_7$ respectively. This data is shown in Figure 3.5.

Simulations were performed using the dipolar spin ice model [23], as seen in Figure 3.5, to explain this behavior in $Dy_2Ti_2O_7$. While the simulations agreed with the quasi-plateau region, they disagreed strongly with data below $\sim 1K$, which was expected to have a barrier to relaxation of $6J_{eff}$ as was found previously for $Ho_2Ti_2O_7$. Instead of $6J_{eff}$, it was found that the barrier was $9J_{eff}$ for $Dy_2Ti_2O_7$ in the data of [64], indicating some discrepancy in the dipolar spin ice model. The discrepancy arises from the fact that these barriers should have been the same value of $6J_{eff}$ for $Dy_2Ti_2O_7$ and $Ho_2Ti_2O_7$, where J_{eff} is different for each material [23].

After this work, d.c. magnetization data was taken on $Dy_2Ti_2O_7$ in this third low temperature regime in [50]. This data is shown in Figure 3.6. This data characterized the low temperature magnetic properties of $Dy_2Ti_2O_7$ through measurement of the dynamical correlation function, $C(t)$. Their magnetization data was found to decay with a stretched exponential behavior in zero field at short times, and with a long algebraic tail at long times, deviating from the expected simple exponential predicted from the dipolar spin ice model. Numerical simulations were performed in [50] which were able to explain the
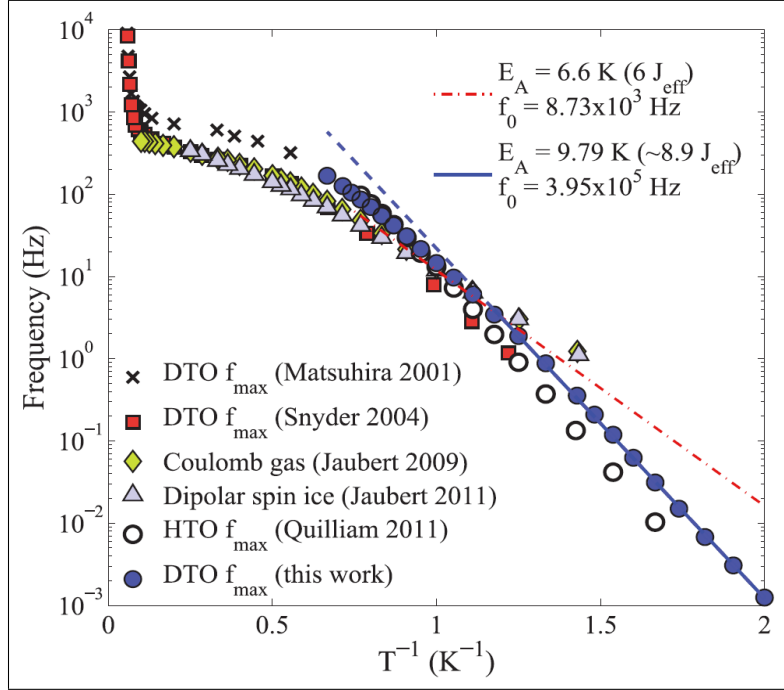
Figure 3.5: The a.c. susceptibility magnetic relaxation times for $Dy_2Ti_2O_7$ obtained from [64], compared to the simulations from [23] and other previous work. The measured times differ from the simulated values obtained through a dipolar spin ice model simulation, and the barrier to relaxation differs between $Dy_2Ti_2O_7$ and $Ho_2Ti_2O_7$ as $9J_{eff}$ and $6J_{eff}$ respectively.

observed data as a complicated interaction of monopole excitations (which are discussed in the next section) with each other, and also with impurities in the $Dy_2Ti_2O_7$ non-magnetic sub lattice. These impurities were given the name 'stuffed sites'. These are sites where a Dy^{3+} ion is sitting on the site of a non-magnetic Ti^{4+} ion. To date, the work of [23] has succeeded in explaining the quasi plateau region, and the work of [50] has been the only one capable of explaining the Arrhenius behavior observed below that regime. These measurements will later be referenced when discussing the zero field a.c. susceptibility data obtained in this thesis, as well as explaining some possible consequences of the in-field data. In the temperature range of the data in thesis ($T < 1.2K$), the only model consistent with experimentally observed a.c. susceptibilty data is the one which considered the role of monopole dynamics and impurities in $Dy_2Ti_2O_7$ from [50]. Thus, these excitations are important for all data in this thesis, and they are explained in detail next.
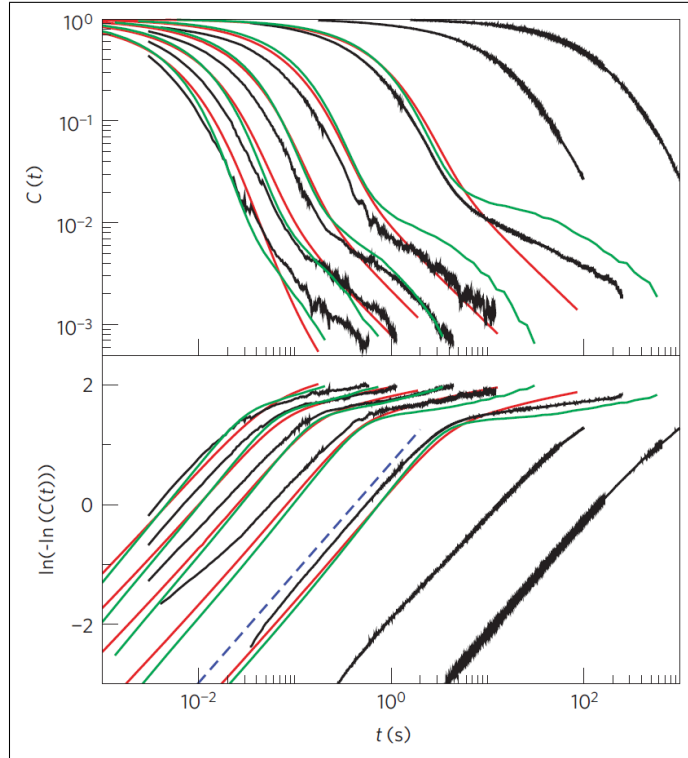
Figure 3.6: The correlation functions below 1 K in $Dy_2Ti_2O_7$ from [50]. The black data is experimental, showing that the correlation function is not a simple exponential as expected within the dipolar spin ice model. The green lines are monte carlo simulations, where the stretching was attributed to impurity effects known as stuffed sites. The agreement between experiment and simulations is very convincing.

3.2 Monopole excitations

One consequence of the previously described magnetic frustration arising within the dipolar spin ice model is the idea of monopole excitations, described well by Castelnovo in [10]. With the ice rules being obeyed, 2 spins point in and 2 spins point out of each tetrahedra in the pyrochlore lattice in the spin ice state. One can think of this as being the ground state of the crystal at low temperatures, then, a thermal excitation would be a single spin flip which breaks the ice rules to form 3-in-1-out and 3-out-1-in states within tetrahedron. The result of one of these single spin flips is a non zero divergence of the magnetic field intensity H and the magnetization M, which leaves $\nabla \cdot B = 0$ in each of the two tetrahedra connected to the flipped spin. It can be shown that these divergences map to magnetic

Dipolar Spin Ice	Dumbbell/Monopoles
2-in-2-out ground state	Vacuum
3 in-1 out defects (local excitations)	Quasi-particles (monopoles)
Dipolar Interactions	Coulomb Interactions
between magnetic dipoles	between magnetic monopoles
Pyrochlore lattice	Diamond lattice
Canonical Ensemble	Grand Canonical Ensemble

Table 3.1: Differences between the dipolar spin ice model and the interacting monopole picture used in most simulations, from [23].

monopole quasiparticles residing in each of the tetrahedra connected to the flipped spin, and that the divergences are consistent with standard electromagnetic theory [30]. The system looks mathematically like a monopole and antimonopole pair have formed, with both being confined to the crystal lattice. This is best viewed through the dumbbell model, as shown in Figure 3.7. The spins in the pyrochlore lattice are replaced by a rod of twice the length from the center of each tetrahedra to the corner, with a positive and negative magnetic charge on either end. Thermal excitations (in zero field) create a 1-in 3-out and 1-out 3-in state, which corresponds to the dumbbell flipping, revealing excess magnetic charge inside of the two tetrahedra connected by the flipped spin; i.e. a monopole and antimonopole pair has formed. These excitations have been theorized to be able to move freely throughout the crystal (i.e. finite energy cost to move them indefinitely far apart) through a network of spin flips, connected by a Dirac string [10]. Due to this freedom, and the weakly interacting nature of the monopoles, models of diffusive brownian motion have been used to explain the movement of monopoles [50]. Many models of recent low temperature a.c. susceptibility data have turned to dynamics of monopole quasiparticles interacting with one another through a magnetic analog of a $\frac{1}{r}$ Coulomb potential on a diamond lattice. These models have been met with varying levels of success. The diamond lattice arises from the monopoles existing in the centers of each tetrahedron on the pyrochlore lattice (within the dumbbell model), and the centers of the pyrochlore lattice correspond to a diamond lattice. The main differences between the dipolar spin ice model and the monopole picture is given by Table 3.1 from [23].

One of the first successes of the monopole picture was explaining a liquid-gas type transition observed with a magnetic field along the [1 1 1] direction in $Dy_2Ti_2O_7$ near 0.9 T, explained well in [21]. When a magnetic field is applied along the [1 1 1] direction in $Dy_2Ti_2O_7$, a state known as the Kagome ice state forms (which will be discussed in the
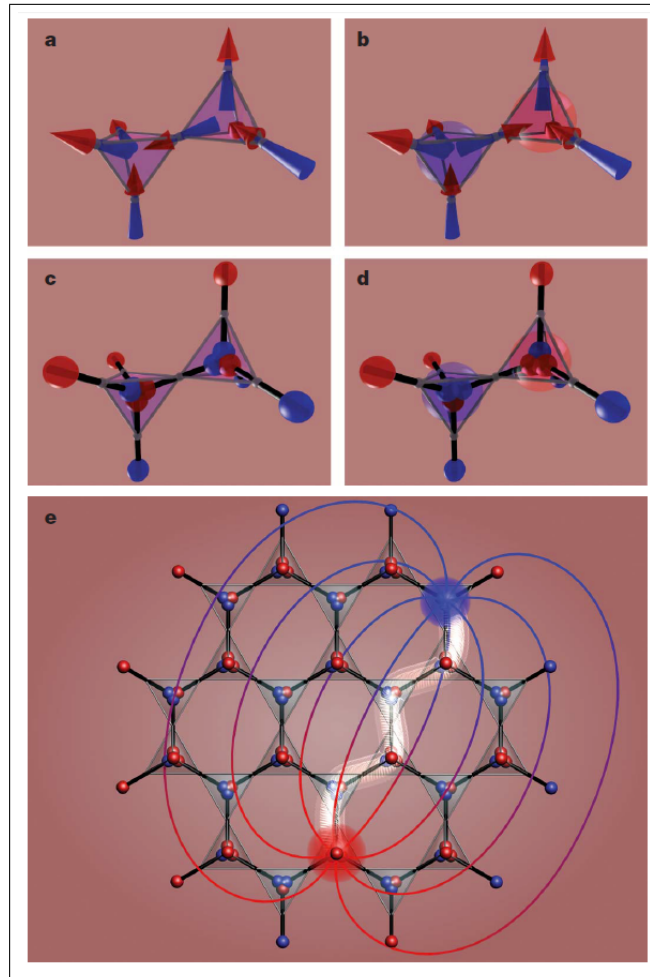
Figure 3.7: The dumbbell model as described in [10]. Image 'a' shows the standard spin ice state, following 2-in 2-out ice rules, and in 'c', the dumbbell model mapping for this is shown. In 'b' the 2-in 2-out rule is broken corresponding to a flipped spin, and the corresponding mapping to the dumbbell model is shown in 'd'. In 'e', the author is showing a monopole-antimonopole pair which has separated, connected by a network of flipped spins shown in white called a Dirac string.

next section), as well as a monopole crystal state where the spins are forced into 1-in-3-out or 1-out-3-in states throughout the pyrochlore lattice. Both states arise from the Zeeman energy gain of the magnetic ion spins in the pyrochlore lattice, owed to the applied field. At around 0.9 T, the monopole crystal state forms and is characterized by a first order

phase transition at low enough temperature, as observed through heat capacity [4]. This transition was not expected to be first order from the dipolar spin ice model, as mentioned in [10], but the result could be explained by looking at the system as monopoles interacting through a magnetic coulomb potential. This followed from work on lattice models of ionic systems [10]. The movement from the dipolar spin ice model, to a model of monopole quasiparticles interacting through a magnetic Coulomb interaction, motivated the use of Debye-Hückel theory for Coulomb liquids in explaining a number of heat capacity results. This model was used to explain heat capacity measurements of $Dy_2Ti_2O_7$ in [40] and [9]. In both cases, application of this model was met with some degree of success. The monopole picture has also been used to explain data from other measurement techniques than heat capacity. Dirac strings have been observed in neutron scattering on $Dy_2Ti_2O_7$ [40] by controlling their density and orientation with an applied field along the $[0\,0\,1]$ crystallographic direction. Thermal relaxation and transport measurements from [27] were used to support the idea of monopole/antimonopole pair creation in $Dy_2Ti_2O_7$. Onsager's theory of electrolytes has been used to describe magnetization measurements of $Dy_2Ti_2O_7$ in [18]. Also, in the related field of artifical spin ice, monopoles have been observed in real space on an artifical kagome lattice [39].

While the monopole picture has proven useful to explain heat capacity, neutron scattering, thermal transport and magnetization data, it initially fell short for a.c. susceptibility data. Simulations performed in [30] and [23] used the monopole picture to try to explain the quasi-plateau region and the low temperature ($T \lesssim 1K$) Arrhenius region of a.c. susceptibility data. The main difference between these two simulations is described in Table 3.1. Both models however failed to capture the quasi-plateau region data of [56] in the low temperature limit, and deviated even more from measurements performed in [64]. It was not determined why these deviations occured for both the dipolar spin ice dynamics simulation and also the monopole dynamics simulation, and also why the barrier to relaxation in this region was experimentally determined to be $6J_{eff}$ for $Ho_2Ti_2O_7$ and $9J_{eff}$ for $Dy_2Ti_2O_7$. It was expected that $Dy_2Ti_2O_7$ and $Ho_2Ti_2O_7$, being sister compounds, would have the same barrier of either $6J_{eff}$ or $9J_{eff}$ in this region according to the dipolar spin ice model. One possible explanation for the difference between the two measured values is the nuclear hyperfine interaction in $Ho_2Ti_2O_7$, as mentioned in [64]. Debye-Hückel theory was also employed to explain the quasi-plateau region, from [9], and was met with a similar level of success, disagreeing with the results of [64]. A compilation of these different models is shown in Figure 3.8.

A much more successful theoretical explanation for the Arrhenius region came later in the work of [50]. Here, simulations were performed using the dipolar spin ice model similar to [23] but with three main differences. First, monte carlo simulations were performed
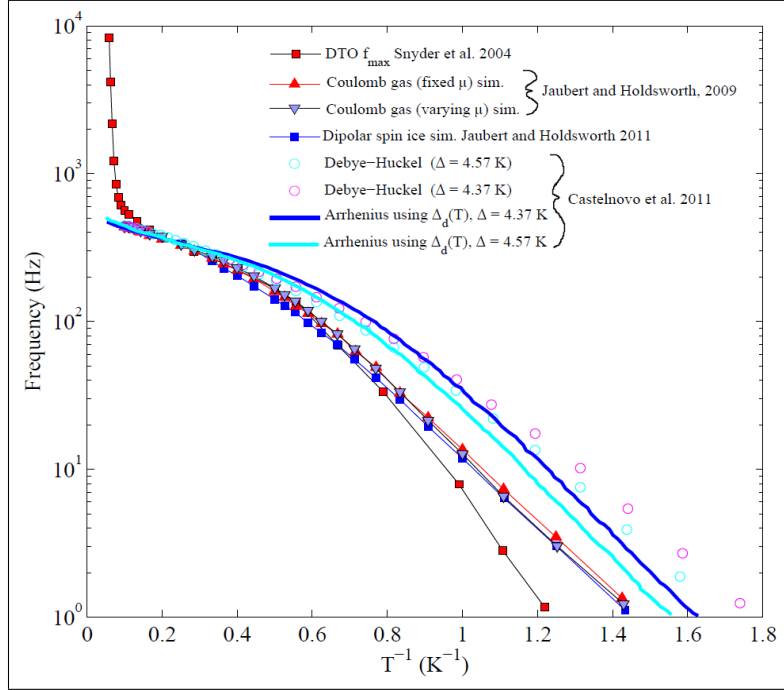
Figure 3.8: A compilation of various theoretical attempts to explain the $T \lesssim 1K$ Arrhenius relaxation in $Dy_2Ti_2O_7$ using the mapping from dipolar spin ice model to the dumbbell model, from [65]. None of the models agree very well with the experimental data of [57] at temperatures below roughly 1 K.

using open boundary conditions, which was done to take into account possible surface effect corrections such as charge build up [50]. This mathematical choice caused the stretched exponential behavior observed in the correlation function simulations. Next, the lattice was filled with $\sim 0.3\%$ impurities known as stuffed sites, which are sites where a magnetic Dy^{3+} ion sits on the site of a non-magnetic Ti^{4+} ion. The influence of these stuffed sites was to act as locations which trapped monopole excitations due to an increase in the spin flip cost near a stuffed site, and also to increase monopole density near the stuffed site due to a lowered spin flip cost in adjacent tetrahedra [50]. Their effect in the simulation resulted in the long-time algebraic tail observed in the dynamical correlation function. Finally, the magnetic relaxation times τ were assumed to be proportional to one over the density of monopoles $\frac{1}{\rho}$, where $\rho^{-1} \propto e^{\frac{4.5K}{T}}$, a result from Debye-Hückel theory [9]. In addition to this, the characteristic relaxation time, τ_0, was assumed to be proportional to one over the density of monopoles so that the full relaxation time equation in the low temperature limit became $\tau \propto \rho^{-2} \propto e^{\frac{9K}{T}}$. These mathematical choices made the simulated

correlation functions agree with experimental data, and also predicted the correct barrier to relaxation. The agreement between theory and experiment is shown in Figure 3.6. This agreement between theory and a.c. susceptibility data in the low temperature Arrhenius region is the best to date, and motivates the idea that defects and surface effects have an important role in this regime for $Dy_2Ti_2O_7$, and that the low temperature regime is strongly dependent on monopole dynamics. If this is the case, it would be interesting to see how the Arrhenius regime changes in the case of a drastic difference in monopole dynamics and impurity levels. The latter is the study of other work, but the former is done in this thesis by changing the dimensionality of the monopole dynamics from 3-D to 2-D by measuring the Arrhenius regime in the Kagome ice state of $Dy_2Ti_2O_7$. The Kagome ice state is described in detail next.

3.3   Kagome ice state

The Kagome ice state is a state which forms within the dipolar spin ice model when a magnetic field is applied along the [1 1 1] crystallographic direction in the pyrochlore lattice. The pyrochlore lattice can be viewed as stacked triangular lattice layers and Kagome lattice layers along the [1 1 1] direction, as seen in Figure 3.9 (a), from [8]. When a magnetic field is applied along the [1 1 1] direction, the spins parallel to the [1 1 1] direction in the tetrahedral basis cell, which are the spins in the triangular layers, gain a significant Zeeman energy when a magnetic field is applied along this direction. This results in it becoming more and more energetically favorable for them to align with the field. As these triangular lattice spins become pinned, the system is different from the spin ice state even though the ice rules are still being obeyed. This is due to the fact that in the spin ice case, the triangular layer spins could have pointed either towards the [1 1 1] direction or away from it, but are now instead forced to point along one direction, the direction of the applied field. Due to this, in the limit of low applied field, there are 3 spins in each tetrahedron which are minimizing their Zeeman energy with respect to the applied field and one spin that is not. This spin has a component opposing the applied field due to it minimizing its energy with respect to the ferromagnetic exchange J_{eff} within the dipolar spin ice model; i.e. it is still obeying the ice rules. This is seen in Figure 3.9 (a). In the limit that the applied magnetic field does not give a Zeeman energy greater than J_{eff} to the Kagome plane spin which is opposing the field, the ice-rules are obeyed in each tetrahedra [38]. When all the spins in the triangular layers are pinned along [111], with the ice-rules still being obeyed in each tetrahedra, this state is dubbed the Kagome ice state. While in this state, the triangular layers decouple from the Kagome layers energetically, and the system looks like stacked

layers of 2-D Kagome lattices. Within each triangle of the Kagome lattice, there are 2-in-1-out or 1-out-2-in states corresponding to whether or not the triangular layer pinned spin is pointing into the tetrahedra to align with the field, or whether it is pointing out of the tetrahedra to align with the field. This is shown in Figure 3.9 (b).
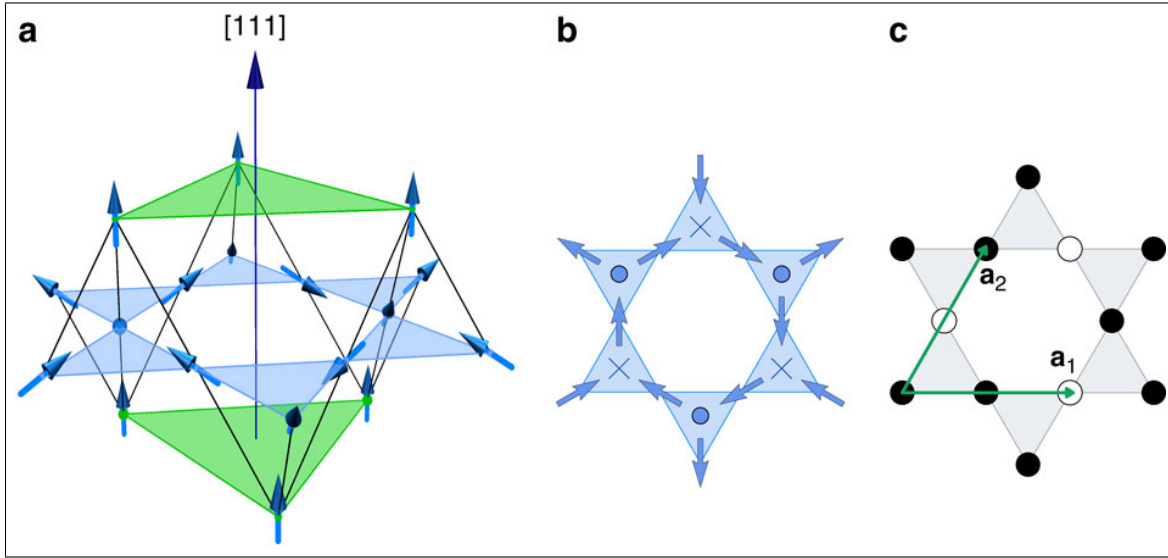
Figure 3.9: Crystal structure of $Dy_2Ti_2O_7$ as viewed along the $[1\,1\,1]$ crystallographic direction, in the Kagome ice state, in 'a'. In the Kagome ice state, the triangular layer spins are pinned to point along $[1\,1\,1]$, and the ice rules are obeyed within each tetrahedra. In 'b', each triangle in the Kagome layers have 1-in-2-out or 2-in-1-out states, corresponding to whether or not the triangular layer spin is pointing into, or out of, the tetrahedra. From [8].

A number of interesting results follow from the Kagome ice picture. First off, the transition into and out of the Kagome ice state as magnetic field is increased results in two plateaus in the magnetization, both of which have been measured in $Dy_2Ti_2O_7$ [54]. These can be seen in Figure 3.10 (b). The first plateau arises from the idealized case of the Kagome ice state mentioned above, where the triangular layer spins are pinned along $[1\,1\,1]$ and the Kagome layers are filled with 2-in-1-out or 1-in-2-out spin states. In this case, the magnetization saturates and the spins are no longer able to increase their component along $[1\,1\,1]$; that is, until a Zeeman energy is given to the Kagome plane spin which has a component opposing the field (labelled as $[\bar{1}\,\bar{1}\,1]$) which is greater than the effective ferromagnetic interaction J_{eff}. Strong evidence of this picture is the fact that the experimental plateau region occurs near 0.5 T for $Dy_2Ti_2O_7$, which is close to the critical

field where the Zeeman energy given to the $[\bar{1}\,\bar{1}\,1]$ spin opposing the field is equal to J_{eff}; i.e. $(\frac{1}{3})g_J J u_B(\mu_0 H_{eff}) = 1.12K \simeq J_{eff}$ [16], where $g_J J$ is 10 $\frac{\mu_B}{Dy}$. Also, the low field magnetization plateau has an experimentally measured magnetization value of 3.33 $\frac{\mu_B}{Dy}$ along the $[1\,1\,1]$ direction [16], which can be calculated from [38], shown in Equation 3.4. The second magnetization plateau arises when the applied field has been increased to the point where the Zeeman energy given to the $[\bar{1}\,\bar{1}\,1]$ spin is greater than J_{eff}. In this case, the field opposed spins in each tetrahedra flip to minimize their Zeeman energy, thus breaking the ice rules and causing each tetrahedra to go into either a 3-in-1-out or 1-in-3-out state. This magnetization plateau has been experimentally found to have a value of 5.0 $\frac{\mu_B}{Dy}$ [16], which can also be calculated from [38], and is shown in Equation 3.5. This state is called the saturated state, or also the monopole crystal state, as each tetrahedra begins to form 3-in-1-out or 3-out-1-in states, meaning the system is eventually composed entirely of monopole excitations. These excitations alternate between monopoles and antimonopoles between neighboring tetrahedra. This effect has been measured in [4], as a first order phase transition measured through heat capacity occuring around 0.9 T along $[1\,1\,1]$.

$$M_{kagome} = \frac{1}{4\sqrt{3}}([1\,1\,1] + [\bar{1}\,1\,1] + [1\,\bar{1}\,1] + [\bar{1}\,\bar{1}\,1]) \cdot \frac{1}{\sqrt{3}}[1\,1\,1] \cdot 10\frac{\mu_B}{Dy} = 3.33\frac{\mu_B}{Dy} \qquad (3.4)$$

$$M_{saturated} = \frac{1}{4\sqrt{3}}([1\,1\,1] + [\bar{1}\,1\,1] + [1\,\bar{1}\,1] + [1\,1\,\bar{1}]) \cdot \frac{1}{\sqrt{3}}[1\,1\,1] \cdot 10\frac{\mu_B}{Dy} = 5.0\frac{\mu_B}{Dy} \qquad (3.5)$$

The Kagome ice state is interesting due to the decoupling between the Kagome planes and the triangular planes. In this state, the $[1\,1\,1]$ pinned spins are no longer able to flip and so monopole defects are confined to 2-D sheets, as seen in Figure 3.11 from [25]. Since the monopoles become confined to 2-D sheets, if they are indeed diffusively moving quasi particles interacting with a $\frac{1}{r}$ Coulomb potential in 3-D, one could theorize the Coulomb interaction between them to change to a logarithmic Coulomb potential in 2-D. This idea has been considered in [41], where a 2-D logarithmic Coulomb potential model was used to derive a possible scaling form for the real and imaginary part of the a.c. susceptibility in the Kagome ice state. The scaling law form is given in Equation 3.6. Here, $\gamma = b\sqrt{\frac{w_1}{w}}$ with $b = \frac{1}{4}$, and w_1 is a characteristic frequency described in [41] which is related to the diffusion constant of monopole excitations in the 2-D Kagome lattice, and their correlation length, and $a = (0, 0, 1, \frac{3}{2}, -\frac{1}{2})$, $b = (0, 0, \frac{1}{2}, 1, \frac{1}{2})$.

26

(a) Phase diagram   (b) Magnetization plateaus
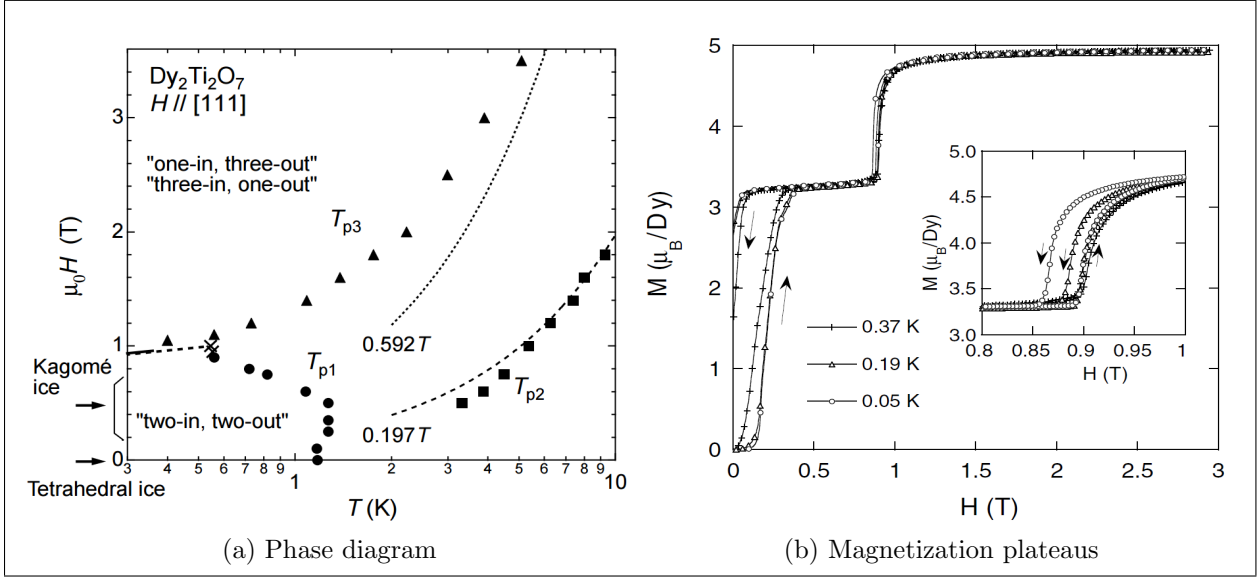
Figure 3.10: The Kagome ice phase diagram for $Dy_2Ti_2O_7$ from [21] in (a) and the magnetization plateaus along the [1 1 1] direction measured in $Dy_2Ti_2O_7$ from [54] in (b).

$$\frac{X'(w)}{X(0)} \simeq 1 - \frac{\gamma^3}{8}[K_1(\gamma) + K_3(\gamma)]$$

$$\frac{X''(w)}{X(0)} \simeq \frac{\gamma^2}{8\pi}[G_{1,5}^{4,1}\left(\frac{\gamma^4}{2^8}\ \middle|\ \begin{matrix}0\\a\end{matrix}\right) - G_{1,5}^{4,1}\left(\frac{\gamma^4}{2^8}\ \middle|\ \begin{matrix}0\\b\end{matrix}\right)]$$

(3.6)
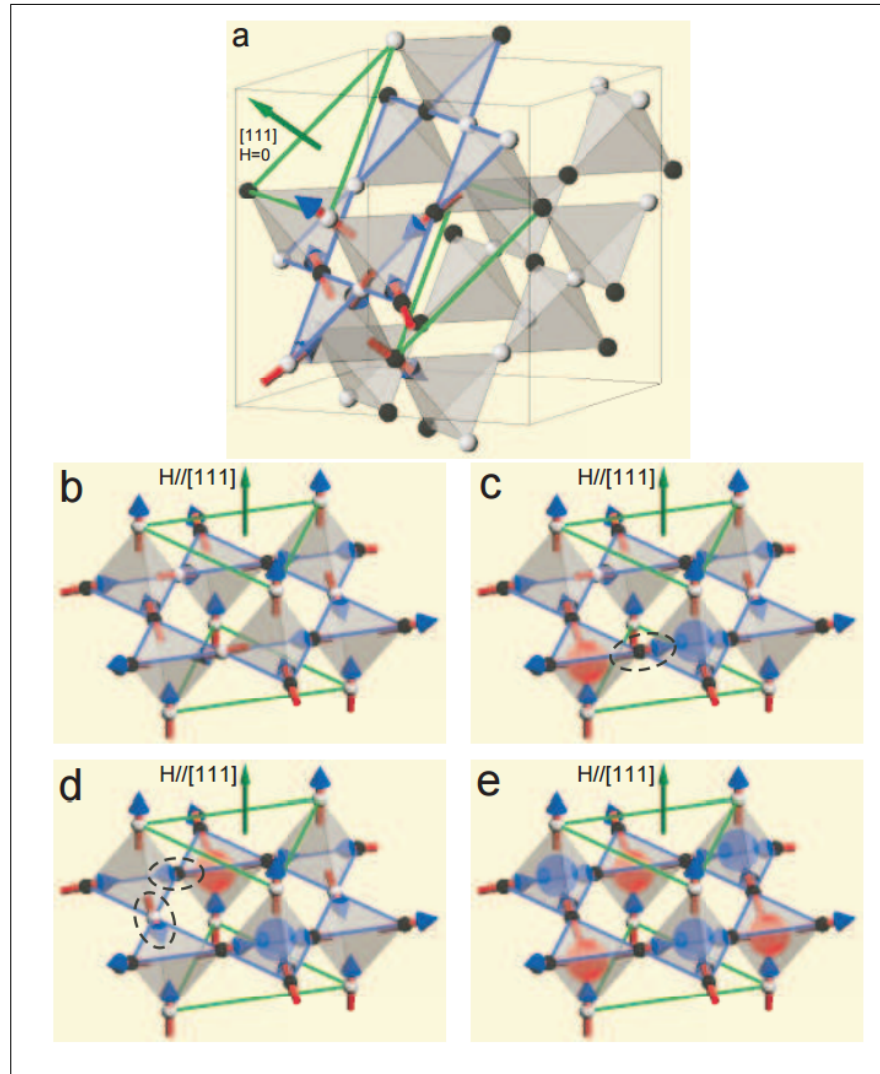
Figure 3.11: Monopole dynamics in the Kagome ice state, from [25]. In 'a', a cutout of the pyrochlore lattice is taken and shown in 'b' along the [1 1 1] direction. In 'c', a monopole-antimonopole defect has formed due to a spin flip excitation which breaks the ice rules, represented by red and blue spheres. In 'd', the monopoles have moved apart along the Kagome plane by flipping two spins denoted by dashed circles. In 'e', the monopole crystal state is shown.

One result important to this thesis is recent heat capacity measurements in the Kagome ice state of $Dy_2Ti_2O_7$, shown in Figure 3.12, from [25]. In [25], it was found that the low temperature heat capacity in the Kagome ice state of $Dy_2Ti_2O_7$ fits to an Arrhenius form with a barrier close to the energy cost to create a pair of monopole defects in zero field, namely $4J_{eff}$. This barrier is found to change linearly with applied field, and this linear change is interpreted as a changing cost to create a pair of monopoles. This changing energy cost was interpreted as arising from the additional Zeeman energy given to the Kagome plane spins when in the Kagome ice state [25]. Also in [25], the density of monopoles in the Kagome ice state was studied through neutron scattering data and explained through a monte carlo simulation. They showed that the density of monopoles increases drastically near the liquid-gas phase transition temperature at a field value of around 0.9 T. This was expected due to the monopole crystal state forming. The behavior of the monopole density in the Kagome ice state far below this transition point however, was not studied in detail.
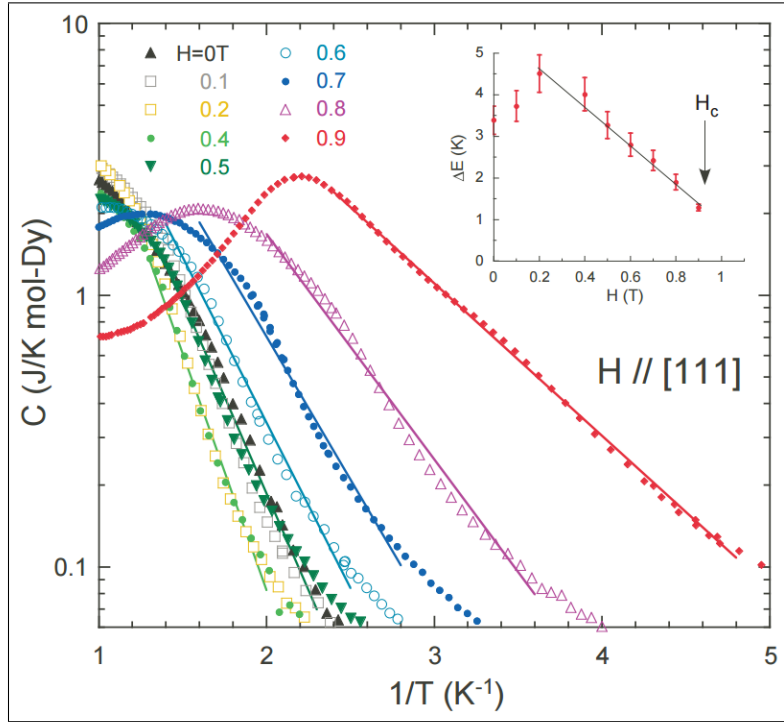
Figure 3.12: Heat capacity measurements performed on $Dy_2Ti_2O_7$ in the Kagome ice state from [25]. A linearly changing barrier to relaxation is observed as a function of applied field along [1 1 1], and it is attributed to the Zeeman energy of the applied field changing the cost to create a monopole pair defect.

29

3.4 Summary

As mentioned above, the dipolar spin ice model was a success in explaining many behaviors measured experimentally in the insulating pyrochlore oxides, which includes $Dy_2Ti_2O_7$. When a magnetic field is applied along the $[1\,1\,1]$ crystallographic direction, such a model indicates the existence of a Kagome ice state, and also a monopole crystal state. Magnetocaloric measurements and magnetization measurements performed thus far agree with this picture [21],[54]. In regards to a.c. susceptibility, the magnetic monopole picture is one possible explanation for Arrhenius relaxation in $Dy_2Ti_2O_7$ below $\sim 1K$ in zero field. If monopoles are indeed responsible for this Arrhenius region of the magnetic relaxation in $Dy_2Ti_2O_7$, then one can imagine a picture where the barrier to relaxation and attempt frequency of $Dy_2Ti_2O_7$ would change as one moves into the Kagome ice state. This could occur due to the monopoles becoming confined to 2-D sheets, as theorized in [25], or through the Zeeman energy given to the Kagome plane spins causing a changing monopole creation cost, as measured in [25]. This thesis focuses on merging the monopole picture into the framework of the Kagome ice state by looking at the a.c. susceptibility in the low temperature Arrhenius relaxation regime of this state. If monopole-monopole interactions dominate in this region, one would expect a significant change to the zero-field data both qualitatively and quantitatively, as the system moves into the Kagome ice state. This was accomplished by developing a SQUID magnetometer setup on a new $^3He/^4He$ dilution fridge, and measuring the characteristic relaxation times in $Dy_2Ti_2O_7$ along $[1\,1\,\overline{2}]$ near and into the Kagome ice state. Such a measurement gives insights into the nature of monopole interactions in this material, and can provide useful information which can be used to develop future theories.

Chapter 4

Experimental details

4.1   Dilution refrigerator

A large portion of time was spent setting up a dilution refrigerator capable of taking both heat capacity and a.c. susceptibility data down to 50 mK or less, in fields up to 1 T. This was achieved by taking a currently existing dilution refrigerator setup from Janis and fitting it with custom components designed for this purpose. The following are key aspects of setting up the refrigerator.

- Installation of a new 350 lb dewar designed by Kadel Engineering which could support a 100 lb superconducting magnet in the liquid Helium bath space.

- Installation of a superconducting magnet which could reach fields up to 8.5 T given 77.5 A.

- Design and installation of a new vacuum can and radiation shield that could fit concentrically into the superconducting magnet's 5.25 inch high field region bore.

- Machining and installation of all the copper stages running from the mixing chamber down through the magnet's compensated region into the high field region.

- Soldering and installation of all the wiring and coaxial cable for thermometry, heat capacity, and a.c. susceptibility.
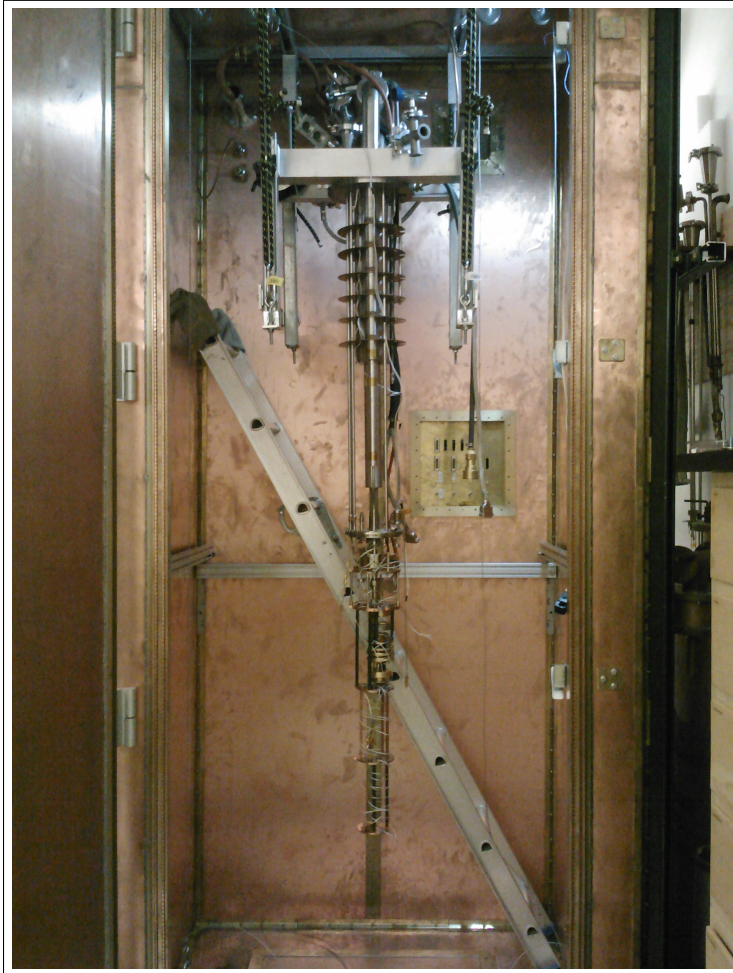
Figure 4.1: The dilution unit modified for in-field SQUID magnetometry. The unit sits inside of an RFI/EMI shielded enclosure on a unistrut frame. The vibration isolation is provided by suspending the whole unit from bungee cords, which can be seen in this image.

The dilution fridge was a 100 μmol unit pre-installed on a unistrut frame in a Universal Shielding Corp. RFI/EMI shielded enclosure, shown in Figure 4.1. This enclosure acts as a Faraday cage and prevents electric fields from reaching the experiments inside the dewar, which would create noise. The dewar shown in Figure 4.2 is designed to hold a 100 lb superconducting magnet inside of the Helium bath, and raises and lowers within this shielded room using a removable floor panel and a system of lead counterweights. A 100 lb superconducting magnet from CryoMagnetics Inc. was loaded into the dewar from beneath on a hydraulic jack. The magnet reaches 8.5 T for a current of 77.53 A, and has a field homogeneity of $\pm 0.1\%$ over 1 cm, and has an inductance of 55.3 H. A very important feature of this magnet is the compensated region, where counter-wound leads negate the effect of the main field in a region of around 12 inches, to an accuracy of 5 mT or less along the length
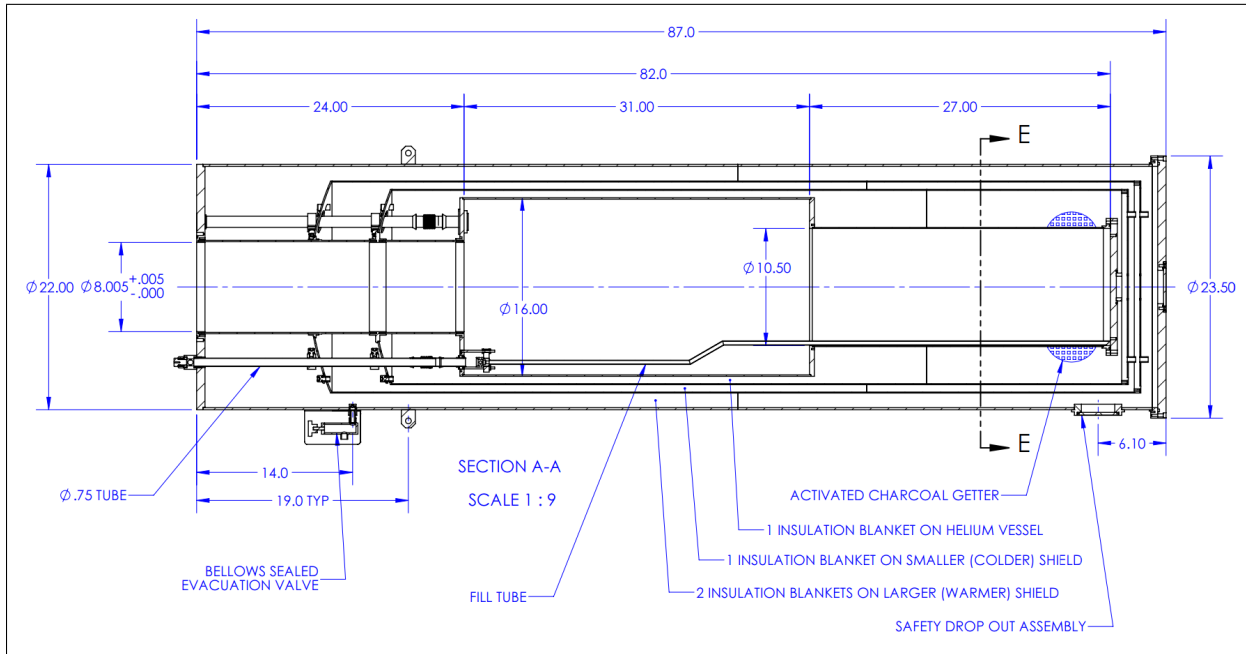
Figure 4.2: The dewar designed by Kadel engineering. The superconducting magnet is loaded vertically through a flange on the bottom of the dewar into 10.5 inch x 27 inch space in the liquid Helium bath.

of the compensated region. This region is important as it allows for heat capacity and a.c. susceptibility measurements to be made in close to zero field, even when the main field is turned on. Also, this region is absolutely necessary in order to run Germanium resistance thermometers on the mixing chamber. This is due to the large magneto resistance of Germanium resistance thermometers. A RuO_2 thermometer on the mixing chamber which came calibrated from Janis was measured at 5 different temperatures between 100 mK - 300 mK in zero field, and then compared to the resistance values at the same 5 temperatures in a 0.5 T field. During this test, the temperature control was determined using a Germanium resistance thermometer calibrated by Lakeshore Cryotronics, which sat in the magnet's compensated region. The zero field and in-field RuO_2 resistance values were the same to within less than $40\mu K$, which was at the noise level of the temperature control on the thermometry. This showed the Germanium resistance thermometer which was determining the temperature was minimally effected by the main field, showing the success of the compensated region. This test relies on the fact that the magneto resistance of Germanium resistance thermometers is much larger than that of RuO_2 thermometers, which allows for the effect of the field on the Germanium resistance thermometer to be quantified using a

33

RuO_2 thermometer. The effect of the compensated region was also seen qualitatively in a cool down where one SQUID gradiometer was operated in the compensated region, and another SQUID gradiometer was operated in the high field region only a few inches away. A 0.5 T field was turned on, and the SQUID in the compensated region had the same noise levels on it as it did when the magnet was shut off, and the bias point of it didn't change when the field was increased to 0.5 T. The gradiometer in the high field region however had significantly more noise, with d.c. offsets, and a different bias point. This showed qualitatively that the compensated region was working. Lead tinned brass leads with dimensions 72 inch x 1/4 inch x 1/32 inch each were soldered onto the magnet leads and fed through the top of the dewar along with 0.032 inch diameter copper wires of the same length for the persistence mode switch leads and voltage taps for the magnet. All of the leads were set up with electrical feed-throughs on flanges connected to the Helium recovery system which provided Helium vapor cooling to reduce the boiloff of the dewar. The magnet leads were connected to a power supply through a single 25 pin connector which ran through the shielded room and split into 12 pins per magnet lead; at a 5 A per pin rating this setup with the current wiring can go to 60 A max. The 25 pin connector was chosen so that all of the cabling could be run through a set of 25 pin Pi filters mounted to the side of the EMI/RFI shielded room, which prevents high frequency electromagnetic noise from getting into the room. The magnet was positioned in the center of the dewar with machined Aluminum legs. The boil-off of the dewar was measured to be 10.2 L/day, not including loses from ramping the magnet (which arise from running the persistent mode switch).

Once the magnet was installed and all the final dimensions were measured, a new vacuum can and radiation shield was machined at the University of Waterloo science technical services machine shop. The vacuum can is shown in Figure 4.3. The vacuum can and radiation shield were made of 0.065 inch 304 stainless steel sheets and 0.032 inch Copper sheets respectively. Both had 2 bevels to fit into the compensated region of the superconducting magnet through a 6 inch bore, and then fit into the high field region of the magnet through a 5.25 inch bore. A thin fiberglass plate was machined with a star pattern and installed at the base of the radiation shield to prevent the vacuum can from contacting the radiation shield over the vacuum can's long 43 inch length. The vacuum can and radiation shield are separated 1/4 inch from each other radially, and the radiation shield is separated from the fridge by 1/4 inch radially. The radiation shield also had a thin slice down the entire length to reduce Eddy current heating as the field is ramped. The slice was taped over with coated copper tape that is thermally conductive to some degree, and radiation reflective, but not electrically conductive, thus blocking radiation from the vacuum can while reducing Eddy current heating. A schematic of the concentric nature of the dilution

fridge setup is also shown in Figure 4.3, showing the tight fit of all components, allowing for maximal working area for samples while running. An important point to notice is that the thermometry for the fridge sits inside the field compensated region.

The Copper stages for samples and thermometry from the previous dilution unit no longer fit the new vacuum can and radiation shield. All of the plates and legs were removed from the previous setup, and customized pieces were machined at the science technical services student shop at the University of Waterloo. There are 3 plates in total running from the mixing chamber down to the high field region, as seen in Figure 4.1. The first plate held the thermometry and the heaters for temperature controlling all the stages, and sits very near to the mixing chamber. Two copper links connect this plate to the mixing chamber, to provide the cooling for all the stages. This plate is inside the compensated region of the superconducting magnet as mentioned. The second plate sits ~ 10 inches away and allows for heat capacity cells and SQUIDS to sit inside of the compensated region of the magnet. Next, the third plate which is ~ 8 inches away from the second one sits inside of the non-compensated region, approximately 3 inches away from the high field region. This final plate was filled with threaded holes for holding SQUID susceptometers and heat capacity cells, and was bored out in 3 locations to prevent Eddy current heating.

After all of the above changes were made, the dilution fridge was cooled and ran. Unfortunately, on the first cooldown, it was found that there was a significant leak on the dilution unit, as seen in a spike in the fridge's thermometry around 2 K, near the superfluid transition point of ^4He. Approximately 6 months of work was spent locating leaks on the fridge. Some electrical feedthroughs on the top of the fridge were leaking at the $1e^{-5}Pa\frac{m^3}{s}$ level instead of the $1e^{-8}Pa\frac{m^3}{s}$ level claimed by the manufacturer. The o-rings on the feedthroughs were replaced and one of the feedthroughs removed, which fixed that leak. A series of leaks were found in the gas handling system as well, which involved replacing valves and o-rings. Next, it was found that the dilution unit itself was leaking at the $1e^{-9}Pa\frac{m^3}{s}$ level at room temperature. An external cylinder of ^4He gas was connected to the gas handling system and each component of the gas handling system, along with the fridge, was leak checked. It was found that by plotting out the leak checker level as a function of time, the leak on the dilution unit peaked around 45 minutes after ^4He was let into the return side of the fridge, and only 5 minutes after ^4He was let into the still side. The time lag was taken as evidence of the leak being on the mixing chamber or still. This is due to the fact that these are both after the two impedances on the return side of the dilution unit, and so any gas sent in at room temperature would take a longer time to make it through these fine capillaries, and then out through a leak in the mixing chamber or still. It was found by trial and error that the mixing chamber was leaking (found by beginning to replace all Indium seals on the dilution unit), and the replacement of an Indium seal on
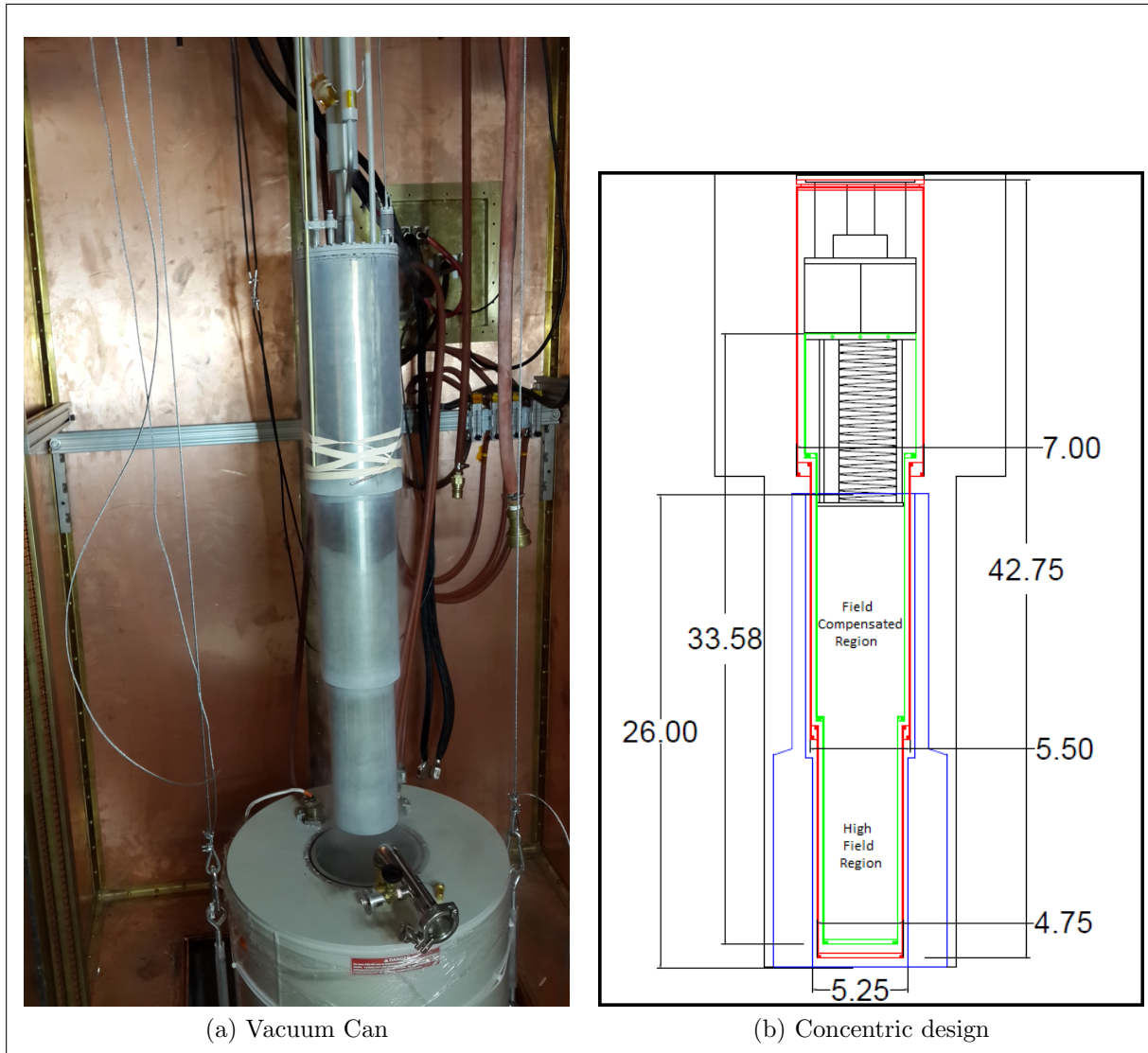
Figure 4.3: The vacuum can built by the science technical services machine shop at the University of Waterloo in (a) just pulled out from the liquid Helium bath. A schematic of the concentric design of the dilution fridge setup in shown in (b), showing the vacuum can in red, radiation shield in green, and magnet in blue. Relevant measurements are shown in inches, and the field-compensated and high-field regions are shown.

the mixing chamber fixed the leak. Once the Indium seal was replaced, no leak could be detected at the $1e^{-12}Pa\frac{m^3}{s}$ level, and no spikes were seen in the fridges thermometry near

2 K from then on.

On the next cooldown, it was found that the mixing chamber was only reaching a base temperature of 400 mK with just the rotary pump pumping on the still side, and the sample stages were sitting at 600 mK. By measuring the circulation rate with a Helium mass flow meter, it was found that the $^3He/^4He$ mix was circulating at only 20 $\mu mols$ per second, instead of the dilution units spec of approximately 100 $\mu mols$ per second. It was decided then to warm up and strengthen the link between the sample stages and the mixing chamber to reduce the observed thermal gradient, and also to run with a vapor booster diffusion pump on the still side to improve the circulation rate of the fridge. In addition to running with the diffusion pump, some bellows leading to the dilution unit were reduced in length and increased in diameter to improve the conductance of the pipes leading to the fridge. It was also found that an 8 inch pneumatic gate valve opening the diffusion pump to the still side was broken, and so it had to be rewired and the compressed air lines leading to it, reinstalled. The gas handling system is shown in Figure 4.4. All the pumps, valves, compressed air lines, etc., are internal to the enclosure.

On the third cooldown, the diffusion pump was opened to the still side of the fridge and the liquid nitrogen cold traps between the diffusion pump and the return side immediately blocked up. It was found that the diffusion pump had a leaking fitting from a residual gas analyzer port. The gas handling system didn't come with lines to clean the mix outside of running it through the ^3He circulation path of the dilution unit, which is not an option once the cold traps have blocked. After warming up, the gas handling system was fitted with new Copper lines which allow a second 100 L safety volume for the $^3He/^4He$ mix to go in the event something goes wrong with the system. These lines also added a path to circulate and clean the mix with the main still side rotary pump through cold traps in the room, without running through the circulation path of the dilution unit. This installed manifold is presented in Figure 4.5.

On the fourth cooldown, with the diffusion pump in place and working, and the gas handling system and dilution unit working properly, the mixing chamber reached a temperature of below 10 mK (240 $k\Omega$ on a RuO_2 resistance thermometer calibrated by Janis). At this temperature, the RuO_2 calibration curve ended, and the sample stages reached 50 mK, the lowest point on the calibration curve of a Germanium resistance thermometer. This cooldown is shown in Figure 4.6. After all of the difficulties in getting the fridge going, the first working cooldown lasted 1 month and the next cooldown lasted 3 months. With these two cooldowns, all the data described in this thesis was obtained. A number of additions were added to the setup once it was operational, with importance given to vibration isolation.

37
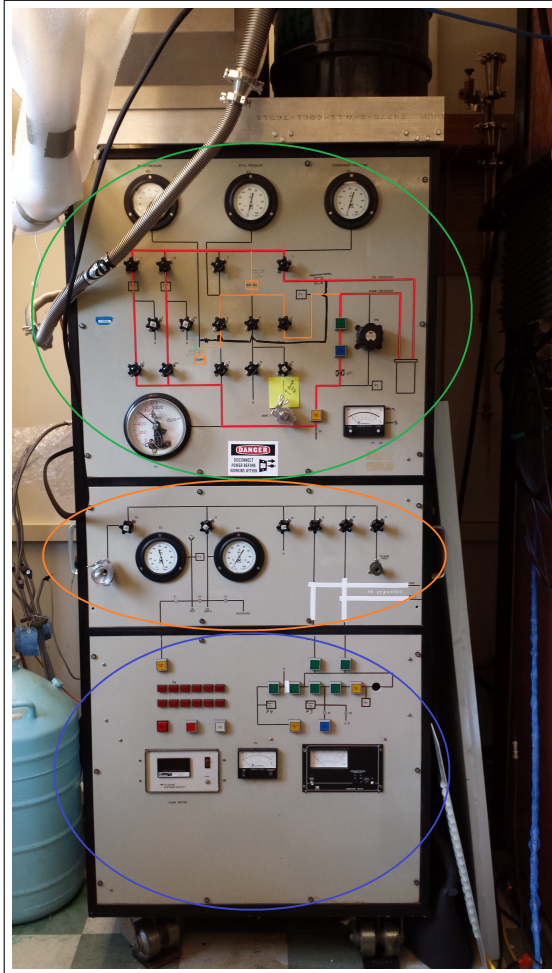
Figure 4.4: The gas handling system for the dilution refrigerator. The green oval highlights the main control panel for sending the $^3He/^4He$ mix into the fridge. The red line highlights the circulation path of the mix, which starts at the still side of the fridge, travels through the diffusion pump and rotary pump, then through liquid Nitrogen and liquid Helium cold traps, then finally into the return side of the fridge. The orange line shows the path of the safety in case of a system fault, where a bypass valve opens and both sides of the fridge vent to storage tanks. The orange oval is a panel responsible for over pressuring the 1 K pot during a liquid Nitrogen transfer, and for pumping out different spaces of the gas handling system. The blue oval is the control panel for the 1 K pot pump and the gate valve in front of the diffusion pump. It also has a Helium mass flow meter.

With the fridge now running very well, it was found that none of the SQUID magnetometer data could be taken below 0.1 Hz, in zero field. A combination of magnetic noise and vibrational noise were determined to be the cause. To reduce magnetic noise, a 100 lb μ-metal shield manufactured by The Mushield Company in Londonderry, New Hampshire was installed on the dilution fridge setup, using aluminum posts on the edges of the dewar. This shield can be seen in Figure 4.7. It was found after installation of this shield that the SQUID a.c. susceptibility could be taken down to 10 mHz in zero field, but was still noisy down to the 1 mHz level. The low frequency a.c. susceptibility noise at this point was most likely due to low frequency temperature fluctuations from lack of vibration isolation on the fridge. At the time, there was no vibration isolation at all. To achieve resolution down to the 1 mHz level, vibration isolation was installed on the fridge in the form of

Figure 4.5: The manifold installed on the gas handling system. The purple arrow leads to the return side of the fridge. By closing valve 3, and opening valve 2, the mix can be sent to backup storage tanks on the top of the gas handling system, (indicated by the green arrow). Here, they can be circulated through external cold traps without running through the dilution unit. With valve 3 open, 2 closed, and 1 open, the fridge is in normal operation mode but with an extra safety, namely the red arrow which leads to the back of the rotary pump of the gas handling system. In the event of the pressure at the back of the rotary pump exceeding 5 psi, a pressure relief valve indicated by the blue arrow opens which will vent the mix to the backup storage tanks on the top of the gas handling system.

bungee cords. To get good vibrational isolation from bungee cords, the natural frequency of the system should be 1 Hz or less, and the bungee cords must be stretched close to their elastic limit at equilibrium, to provide hysteretic damping of the vibrational energy by deformation. The whole dilution fridge setup consists of a 100 lb fridge, a 350 lb dewar, a 100 lb superconducting magnet, and a 100 lb μ-metal shield. Considering everything but the μ-metal shield, this 550 lb load was suspended from four points to the ceiling of the EMI/RFI shielded room, using elbows and steel eye loops attached to knotted bungee cords. With the bungee cords in place, the 100 lb μ-metal shield was added to the setup, and a displacement in the the cords of 0.4 inches was measured. Viewing the setup as a simple harmonic oscillator (a mass attached to a spring), a change of 100 lb in weight divided by 4 (four points of bungee cord contact) creating a displacement of 0.4 inches,
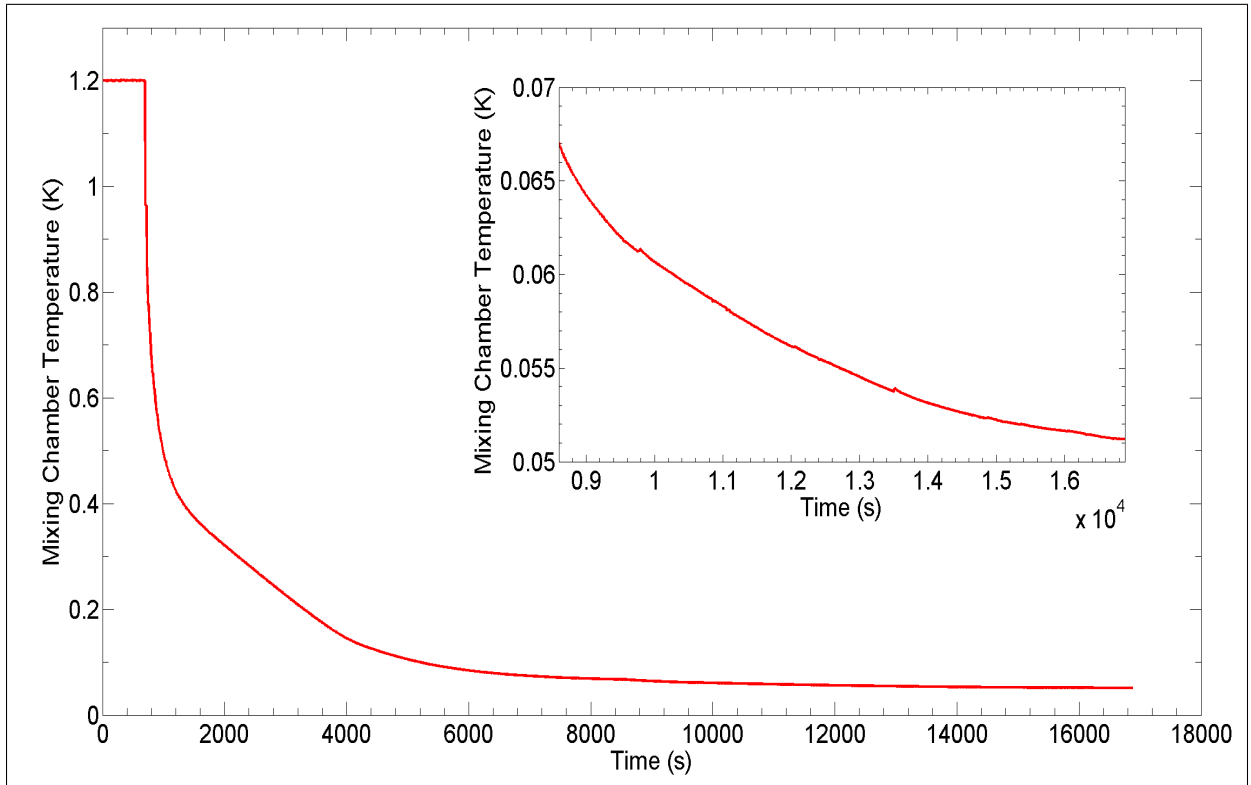
Figure 4.6: A full cooldown of the dilution refrigerator set up in this thesis from 1.2 K, as measured by a Germanium resistance thermometer on the sample stage. The inset is a zoom in on the base temperature, showing the fridge temperature at 51 mK and cooling. The calibration for the Germanium resistance thermometer stopped at 50 mK.

with a 650 lb end load, results in a natural frequency of approximately 1 Hz. In tests done on the bungee cord, it was found that at a stretch factor of approximately 1.5 times the initial length of the bungee cord, the cord was near the end of its elastic limit. At this length, the cord can be used for hysteretic damping, where deformation of the bungee cord is used to dissipate vibrational energy. With the addition of the μ-metal shield, the bungee cords were stretched to a value very close to this 1.5 times the initial length. With the system having a natural frequency of approximately 1Hz, with a bungee cord stretch length of 1.5 times the initial length, vibration isolation was successfully added to the setup. A thorough analysis of the vibration isolation properties of bungee cord setups can be found in many engineering textbooks, such as [53]. The bungee cord setup increased the bandwidth of the zero field a.c. susceptibility measurement by a decade (from 10 mHz

40

Figure 4.7: The dilution refrigerator sitting inside of the dewar during a cooldown. The arrow colors are as follows: Dark blue: RFI/EMI shielded room with removable floor. Green: Mumetal shield. Orange:liquid Helium dewar. Brown:Gas manifold in the back of the room connecting the dewar to a system of pipes at the back of the room, which come over the roof and lead to the Helium recovery system. Red: Lead counterweights which wrap around pulleys located at the top of the room. Purple: Hard to see bungee cords holding the 650 lb load up on a unistrut frame, there are 2 sets of bungees in the front and 2 sets at the back. Light blue:The unistrut frame holding everything up, which is connected to a unistrut reinforced ceiling through the bungee cords when in operating mode, or through the counterweights when not operating.

down to 1 mHz), showing it was successful.

After the μ-metal shield was installed and the vibration isolation was installed, the zero field a.c. susceptibility was able to be taken down to 1 mHz reliably in zero field. The main cause of this was attributed to improved temperature control on the mixing chamber stages from adding vibration isolation, and also improving grounding. A few smaller improvements were made to the setup, such as a 2 psi pressure relief valve was placed between the Helium recovery system and the dewar of the fridge to reduce pressure variations in the dewar bath space caused by pressure variations in the Helium recovery system. All of the above changes also affected the in-field a.c. susceptibility, they allowed the in-field data to go from 100 mHz down to around 10 mHz. Two temperature control

scans of the mixing chamber at 70 mK, taken over 3.5 hours, are shown in Figure 4.8. One data set is in zero field, and the other is in a 600 mT field. They are offset from each other by 200 μK for clarity. The noise levels were close to the limit of the preamplifier noise used in a model 3708 Lakeshore temperature control preamp/scanner, which was used to scan between resistance measurements on multiple thermometers. The zero field temperature control was noisier than the 600 mT temperature control, due to the 600 mT scan having more optimized PID settings in the temperature control feedback loop. The temperature control is good to 1 part in 5,000 for the zero field data, and 1 part in 10,000 for the in-field data, showing the fridge has good temperature control both in zero field, and in-field.
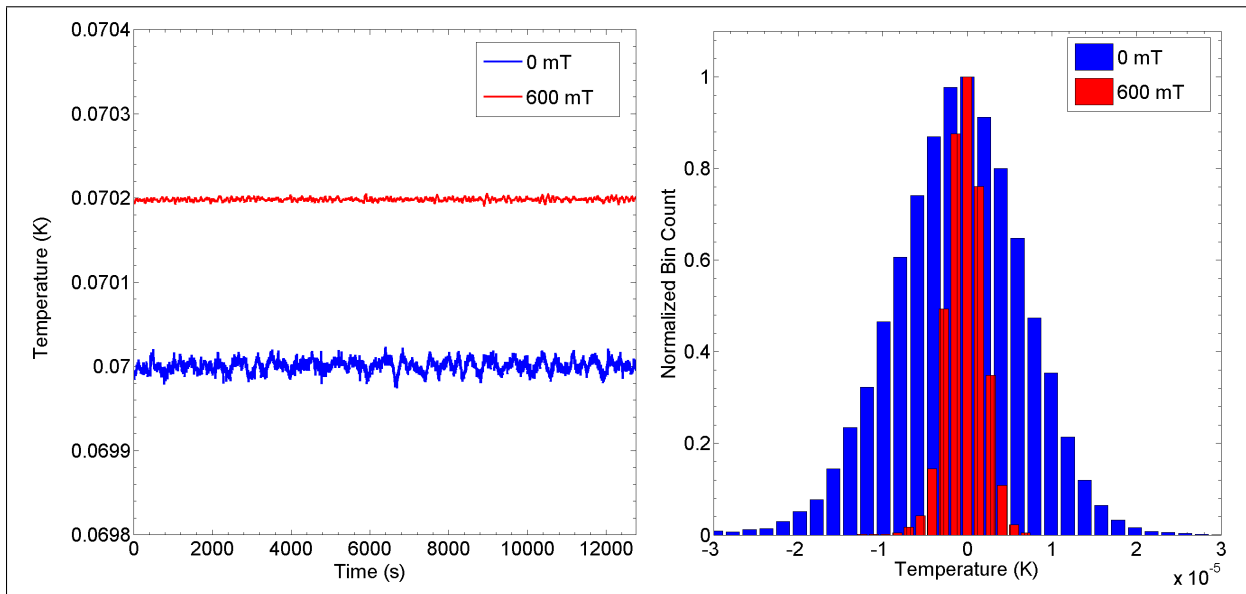
Figure 4.8: Left figure: mixing chamber temperature versus time at 70 mK, in zero field and a 600 mT field. The two data sets are offset from each other by 200 μK. Right figure: histogram of the data in the left figure, in zero field and a 600 mT field. In this plot, the temperature is set to be equal to 0 at 70 mK. The temperature control is good to 1 part in 5,000 for the zero field data, and 1 part in 10,000 for the in-field data. The zero field data is noisier due to the PID settings that were chosen on the temperature controller.

When the 8.5 T magnet was turned on and ramped, very little effect was seen on the dilution refrigerator mixing chamber temperature. As mentioned, the radiation shield had a slice down the whole length to reduce Eddy current heating while ramping the field, and the in-field copper stage where the samples sat was bored out to reduce Eddy current heating as well. As can be seen in Figure 4.9, at a ramp rate of 18 mT/minute (which was

a factor of ~ 10 faster than the ramp rate used for the a.c. susceptibility data taking in the next section) from 400 mT to 500 mT, the fridge temperature changed by approximately 9 mK at 725 mK. The heater power changed by around 20 μW, and the temperature control recovered fully in only a few minutes after ramping, showing that the field ramping had minimal effect on the fridge. In addition to the mixing chamber recovering quickly from the field ramping, the still and 1 K Pot saw no effect when the field was ramped, as expected, as seen in Figure 4.10. The still remained at $\sim$590 mK and the 1 K Pot remained at $\sim$1.38 K during the field ramping, no change to their temperature was observed. This is expected since the still and 1 K Pot were approximately 3-4 feet away from the high field region of the magnet, meaning the fields effect is smaller, and they also have a large cooling power. While the value of 9 mK doesn't give much insight into whether or not the setup has small Eddy current heating (since it's relative to fridge stage design and fridge cooling power), it does show that for the specific design described in this thesis, the fridge is very stable to field ramping. At slower ramp rates, such as the ones used for all the in-field data taking in this thesis, the largest temperature change seen when ramping the field was approximately 1 mK, at 600 mK.
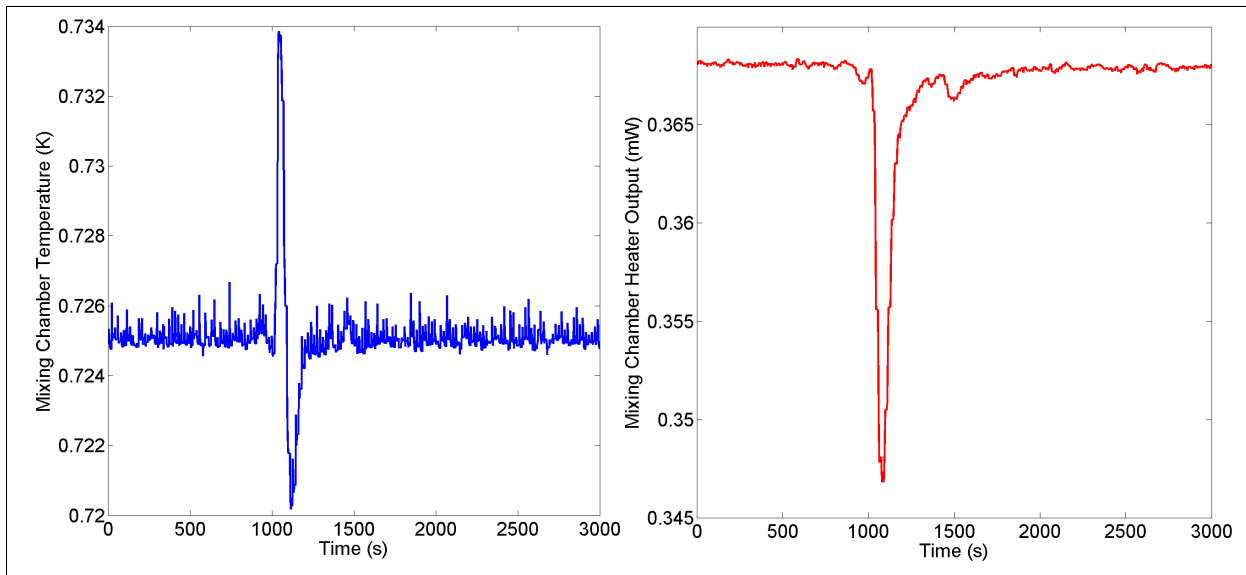
Figure 4.9: Left figure: mixing chamber temperature versus time, right figure: mixing chamber heater power versus time. Both data sets were taken while ramping the 8.5 T magnet from 400 mT to 500 mT at a rate of 18 mT/min at 725 mK, which begins close to the 1000 s mark. The temperature control recovered in only a few minutes, showing the mixing chamber was minimally effected by such a large ramp rate.

43
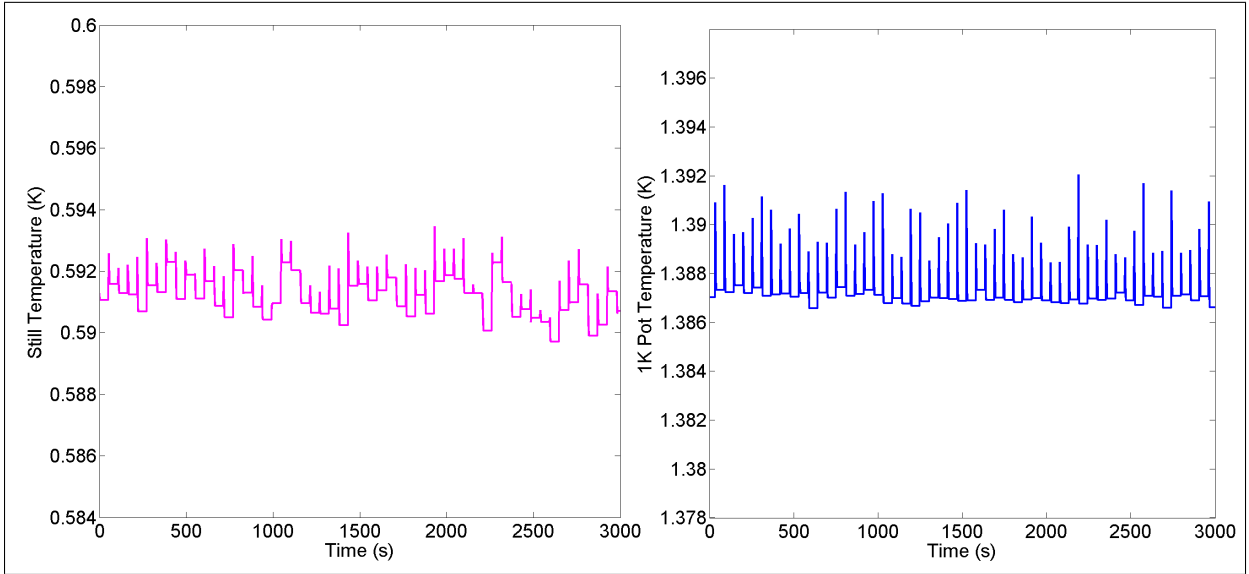
Figure 4.10: Left figure: still temperature versus time, right figure: 1 K pot temperature versus time. Both data sets were taken while ramping the 8.5 T magnet from 400 mT to 500 mT at a rate of 18 mT/min at 725 mK, which begins close to the 1000 s mark. No change in temperature is observed for either during the field ramping.

In summary, a dilution refrigerator setup was modified for in-field heat capacity and a.c. susceptibility data taking. The setup was shown to be very successful, as seen in the cooling curve of Figure 4.6. The expected circulation rate of 100 $\mu mols/s$ was achieved, and the base temperature of the fridge was measured to be under 10 mK, based on a RuO_2 thermometer calibration from Janis. The temperature control of the sample stage, based off a calibrated Germanium resistance thermometer, was found to be better than 0.1% at all temperatures measured for both the a.c. susceptibility data, and also the heat capacity data of this thesis (shown in Appendix A). Sufficient magnetic and vibrational isolation was added to the fridge to allow zero field susceptibility data to be taken down to 1 mHz, and in-field susceptibility data to be taken down to 10 mHz. Some improvements that could be made to the setup in the future are listed below, and it is expected that with these changes, the a.c. susceptibility data could be extended down to 1 mHz in-field.

- Optimize the $^3He/^4He$ mix ratios and amounts for this dilution unit. This could improve the cooling power of the fridge, resulting in better temperature control.

- Increase the thermal conductivity of the copper link between the mixing chamber and the sample stages. As mentioned above, when the fridge was below 10 mK,

the sample stage still sat around 50 mK with a very small cooling rate, as seen in Figure 4.6. Improving the link could improve the cooling power on the sample stage and thus improve temperature control.

- Design a way to rigidly connect the vacuum can to the magnet during a cool down. This should reduce relative vibrational motion between the magnet and the dilution unit, and reduce low frequency susceptibility noise.

- Reduce the heat load on the still. The fridge achieved a circulation rate of $100 \mu mols$ per second, but this was done with only 0.1 mW of still heater power on average throughout the fridge temperature range, instead of the 1-3 mW expected for a normal still design. This indicates a large heat load on the still, which can be improved by for example, running the 1 K Pot with a larger pump to reduce the 1 K Pot temperature from 1.4 K to 1.2 K. Also, the heat load could be coming from the fiberglass piece that was machined to prevent the radiation shield from touching the vacuum can over the long length of the cans. This piece could be reduced in thickness to reduce thermal conductivity, thus reducing the heat load on the still (the radiation shield is thermally coupled to the 4 K vacuum can through the fiberglass, and is thermally coupled to the still). This would increase the still heater range, which gives more control over the circulation rate and should lead to better temperature control as the circulation rate could be optimized as a function of temperature.

- Purchasing a new transfer stick for the dewar, which can be removed during a cool down. Currently, the transfer stick for getting liquid Helium into the dewar has to stay in the transfer port during a cool down. This is because the room is too short to remove it when the dewar is raised and screwed onto the fridge. This transfer stick could be causing Taconis oscillations which increase the boiloff of the dewar, and could be causing vibrational noise in the setup.

4.2 A.c. susceptibility

4.2.1 Measuring a.c. susceptibility with d.c. SQUIDs

All of the a.c. susceptibility measurements were performed in this thesis using a Niobium d.c. SQUID gradiometer. Both gradiometers and standard single pickup loop susceptometers use a d.c. SQUID along with an electronics box running in a feedback mode called a flux-locked-loop. Running in flux-locked-loop mode, the d.c. SQUID becomes a linear

magnetic flux to voltage transducer. A basic description of SQUID susceptometers will be described next, which will lead into the specifics of the d.c. SQUID gradiometer setup used to measure a.c. susceptibility in this thesis. Suggested reading for this topic is [12], who mentions most of what is stated here, as well as more in-depth discussions such as the mathematical equations for the RCSJ model of the d.c. SQUID.

The behavior of Josephson junctions are characterized by the two equations given in Equation 4.1. Here, δ is the phase difference between the cooper pair wavefunctions of the two superconductors on either side of the barrier of the Josephson junction, I_c is the critical current of the junction, where beyond this current value, the junction becomes resistive and a voltage develops across it, and U(I) is the voltage(current) across the junction. Φ_0 is a constant called the flux quantum. If the phase changes in time, then a voltage develops across the Josephson junction, likewise if it does not, then no voltage develops. In the case of a d.c. current applied to the junction, no voltage is measured across the junction due to lack of a dynamical phase $\dot{\delta}$, until the current passes the critical current I_c of the junction, and the junction becomes resistive. The critical current of the junction is much less than the critical currents of the respective superconductors composing the junction. Next, to turn Josephson junctions into a useful device, one can connect two of them in parallel in a ring shape. Magnetic flux lines penetrating a superconducting ring are quantized into integer multiples of flux quanta, i.e. $\Phi = n\Phi_0$ where n is an integer. This is a quantum mechanical effect owed to wavefunction single-valuedness upon choosing one point in the ring, travelling 2π around the ring, and having the same valued wavefunction at the same point. Using the flux quantization of a superconducting ring, and the Josephson relations, one can create the d.c. SQUID, which has many useful applications.

$$I = I_c \sin(\delta)$$
$$\dot{\delta} = \frac{2\pi U}{\Phi_0} \tag{4.1}$$

The application of d.c. SQUIDS relevant to this thesis is magnetic flux measurements. Take the example of magnetic flux penetrating the superconducting ring with 2 Josephson junctions, with the whole ring biased by a current slightly greater than the critical current of the SQUID. This critical current is twice the critical current of each junction, $2I_c$. Since the flux penetrating the ring must be quantized in integer multiples of the flux quantum, a current will be induced in the ring for the case that the penetrating flux is not equal to a flux quantum; i.e $\Phi \neq n\Phi_0$, to make the quantization hold. This current flows around the ring in one direction, the direction where it would oppose the magnetic flux. This means one junction will have a reduced critical current, the junction where the current is flowing

in the same direction as the bias current, and the other junction will have an increased critical current, the junction where the current is flowing in the opposite direction as the bias current. As this flux increases past $\frac{\Phi_0}{2}$, it becomes more energetically favorable for the induced current to switch direction in order to bring the quantized flux to an integer multiple of Φ_0 (i.e. if the applied flux is $0.51\Phi_0$ for example, it is easier for the induced current to add $0.49\Phi_0$ of flux through the loop to get an integer multiple of Φ_0 than it is to screen the applied flux with a flux of $0.51\Phi_0$ from the induced current). The magnetic flux thus modulates the critical current of the SQUID between two values, the current corresponding to a flux of $n\Phi_0$, and the current corresponding to a flux of $(n + \frac{1}{2})\Phi_0$. This effect modulates the voltage across the SQUID if it ran in resistive mode by biasing it at a value slightly greater than $2I_c$. This established the so called $V - \Phi$ curve and I-V curve of the SQUID, both shown in Figure 4.11. The exact shape and values of the I-V and $V - \Phi$ curve of a SQUID is determined through the RCSJ model of a SQUID, described in detail in [12], and also shown in Figure 4.11.

Once the $V - \Phi$ curve is established, a feedback mechanism called a flux-locked-loop can use active P and I controls to maintain the flux through the superconducting loop at a value of $(n + \frac{1}{4})\Phi_0$. Here, the transfer function of the SQUID (i.e. the slope of the $V - \Phi$ curve) is maximized. This means small changes in flux penetrating the SQUID result in the largest changes in voltage measured across the SQUID. Also, the slope changes sign at this point, resulting in the ability to determine the sign of the induced flux. In this way, by monitoring the voltage across the SQUID in such a feedback loop, both the sign of the flux can be resolved, and also flux amplitudes much less than the flux quantum Φ_0. In the case of an a.c. magnetic flux as in a.c. susceptibility measurements, the SQUID output voltage is then a sinusoidal wave. To summarize, to run a d.c. SQUID, a current supply is used to apply a bias current near twice the critical current, I_c, of each junction. Once the d.c. SQUID is biased, and the so called $V - \Phi$ curve is established within the RCSJ model of a d.c. SQUID, then the SQUID can be operated as a linear flux to voltage transducer by running it in a feedback loop.

An electronics box known as a d.c. SQUID controller can apply the bias current to the SQUID, and also a magnetic flux to the SQUID using a small inductively coupled, lithographically plated coil near to it. Magnetic flux is applied to this coil by the SQUID controller, which keeps the flux through the SQUID at a value of $(n + \frac{1}{4})\Phi_0$ in a feedback loop, with P and I control. The voltage signal applied to the coil that is necessary to keep the flux at this value runs between 100 kHz and 2 MHz for the measurements done in this thesis. This voltage signal is linearly proportional to the flux through the loop of the d.c. SQUID, with a proportionality constant that is independent of temperature. This signal is called the flux-locked-loop output. A combination of the operating frequency and the
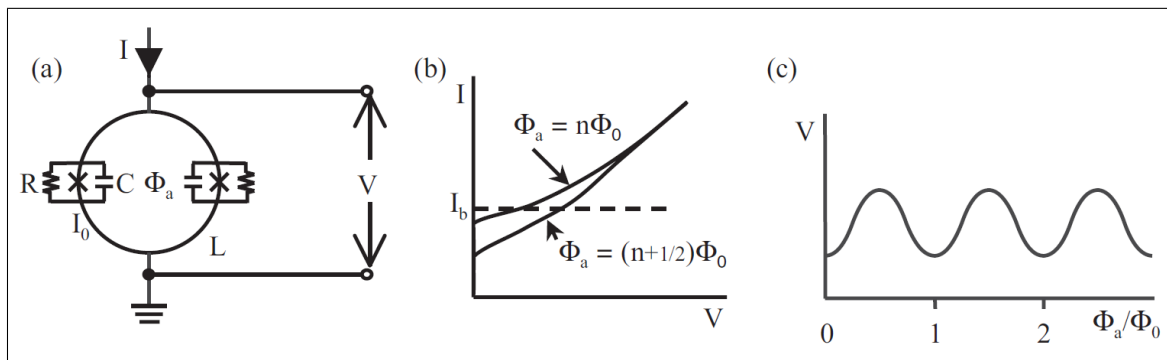
Figure 4.11: In (a), the RCSJ model of a SQUID. In (b), the I-V curve of the d.c. SQUID, and in (c), the $V - \Phi$ curve of the d.c. SQUID. From [12].

slew rate of the preamplifiers involved in the feedback loop set an operational bandwidth for the controller. If any magnetic flux penetrates the SQUID loop at a frequency within the bandwidth of the controllers operation, at an amplitude which isn't high enough to cause the feedback loop electronics to saturate and 'lose lock', then the setup works as an extremely stable and accurate flux to voltage transducer. Such a setup is capable of measuring $\mu \Phi_0$.

It is easy to see now how a sample's magnetic susceptibility can be measured using a d.c. SQUID. By applying a magnetic field with a primary coil to a sample, the sample has induced magnetization that is linearly proportional to the samples magnetic susceptibility in the limit of low applied fields. All data in this thesis is presented in the linear regime of $Dy_2Ti_2O_7$, with excitations between 1-5 mG. The induced magnetization causes a change in magnetic flux through the SQUID, if the sample is inductively coupled to the pickup loop of the SQUID using a hand-wound coil for example. Then, the sample's magnetic susceptibility is linearly proportional to the flux-lock-loop output voltage through constants that are temperature independent and can be combined into one. This constant is some-times called the calibration factor of the SQUID. In a.c. susceptibility measurements, an a.c. signal is applied to the primary coil within the operational bandwidth of the SQUID controller, so that the samples sees an a.c. magnetic field. The change in sample magneti-zation with field is then measured as the flux-locked-loop output of the SQUID controller, and this output will oscillate at the applied frequency with an amplitude linearly propor-tional to the a.c. susceptibility of the material. There will be a component of this signal in phase with the primary coil excitation, called the real part of the susceptibility (χ'), and a component out of phase called the imaginary part of the susceptibility (χ''). The susceptibility then takes the form $\chi(w) = \chi'(w) + i\chi''(w)$. A Stanford research SR830

48

model lock-in amplifier was used in this thesis to both apply the excitation current to the primary coil, and also to measure the flux-locked-loop output amplitude, and break it up into both real and imaginary components for analysis.

Typically when using a one loop d.c. SQUID, one has to set it up inside of a susceptometer which has many layers of shielding. The SQUID and the sample must both sit inside of a copper and lead shield to reduce electric and magnetic field noise respectively. Additionally, the SQUID has to sit inside a second lead shield to reduce magnetic noise from the susceptometer coils. The reason for all this shielding is simple. In a one-loop d.c. SQUID, all of the external magnetic noise in the SQUIDS local system penetrates the one loop and is seen on the SQUID flux-locked-loop output. There is no way of discerning background flux from flux due to your sample in the one loop case. The best you can do is cancel the background noise to the best of your ability before adding in the samples signal. To do this, a well designed susceptometer has at the very least, a primary coil, a trim coil, and a flux transformer, all inductively coupled together. Such a setup is shown in Figure 4.12 (a). The susceptometer is cooled to very low temperature, and to a point where the sample being studied, which sits inside of the flux transformer, has little to no magnetic susceptibility in the frequency bandwidth of interest. The flux transformer consists of two counter-wound coils with the same number of turns per unit length joined at one end, and at the other end they are attached to a third coil which couples inductively to the pickup coil of the d.c. SQUID. In the ideal case of no background magnetic noise, no flux would penetrate the SQUID pickup loop when an excitation is applied to the primary coil, because the sample is not there (frozen out), and the flux transformer coils are perfectly counter-wound with the same number of turns. This would mean that the flux-locked-loop output would be 0 V, but due to background flux noise it won't be. To solve this, the same excitation is applied to the primary coil and to a trim coil across two different current limiting resistors. The values of the current limiting resistors are changed until the flux-locked-loop output is 0 V when the excitation is applied, and the sample is frozen out. This is called balancing the coils.

In the case of a gradiometer, everything is drastically simplified. By having two pickup loops which are counter-wound with one another, and are very closely spaced, any magnetic flux common to both loops with the same amplitude will cause an induced current across the SQUID equal to zero. This provides active noise cancellation. It was found experimentally that the cancellation was better than 1 part in 1000 for the GRAD 2D-10 model gradiometer from the company ezSQUID in Germany. This is on the same order of cancellation as the balancing coils method of a susceptometer, but with less work done. By placing your sample inside one of the pickup loops of the gradiometer, you misbalance this balancing, since the induced flux on one side is now the flux through the coil, and also the change in

magnetization due to the sample. Due to this novel design, the flux through the SQUID in the gradiometer case is due to just the sample and any small external fields which the gradiometer was not able to cancel out. This allows for easy measurement of the samples susceptibility, and such a setup is shown in Figure 4.12 (b). In addition to the simplification in the zero field case, for running susceptibility measurements in a large field, this gradiometer design is an absolute must. This is because the outer shield of the standard susceptometer would change the amplitude and field distribution of the applied field. Without this outer shield, balancing the susceptometer would be way too difficult to do using a trim coil. In the case of a gradiometer, the active noise cancellation is there even with no shield (except for the μ-metal shield external to the fridge and magnet), allowing for the sample to be affected by the field, with the gradiometer still balanced. In addition to this, the gradiometer being made of Niobium and having a thickness of approximately 2-3 nm is important, as the third superconducting critical field (Hc3) of Niobium thin films is on the order of over 1 T for films with a thickness in this range. The exact critical field was not determined for these gradiometers, however a study of critical fields in Niobium thin films is described in [22]. This third critical field is the result of superconductivity remaining on the surface of a bulk superconductor at a critical field much higher than that of the critical field of the bulk. This allows the d.c. SQUID to remain operational, and the a.c. susceptibility to be taken in high fields.

4.2.2   A.c. susceptibility measurement details

A model GRAD 2D-10 gradiometer from the company ezSQUID in Germany was installed on the new dilution refrigerator setup, and ran with a non oxygen annealed single crystal sample of $Dy_2Ti_2O_7$. This sample was grown using the floating zone technique, and was provided by Hiroshi Takatsu at the university of Tokyo. This sample is shown in Figure 4.13. The demagnetization factors of this sample are 0.042 along the $[1\,1\,\bar{2}]$ direction and 0.194 along the $[1\,1\,1]$ direction. These are calculated by assuming a rectangular prism geometry for the sample. Under this assumption, the equation derived in [2] for the demagnetization factor, N, of the general rectangular prism was used. This equation only relies on the dimensions of the sample, and as such it is straightforward to calculate.

The gradiometer used in this thesis had the exact same setup as described in [49], shown in Figure 4.14. A 1mm hole is laser ablated into one pickup loop of the GRAD 2D-10 Gradiometer by the company QuesTech in Texas, to make room for a sample. A small rectangle of silicon was cleaved from a silicon wafer to make a very flat surface, and the flat $[1\,1\,1]$ face of the sample was glued onto it using GE Varnish, making the $[1\,1\,\bar{2}]$, or long direction, along the SQUID pickup coil. The wafer with the sample attached was

(a) Standard Susceptometer   (b) Gradiometer
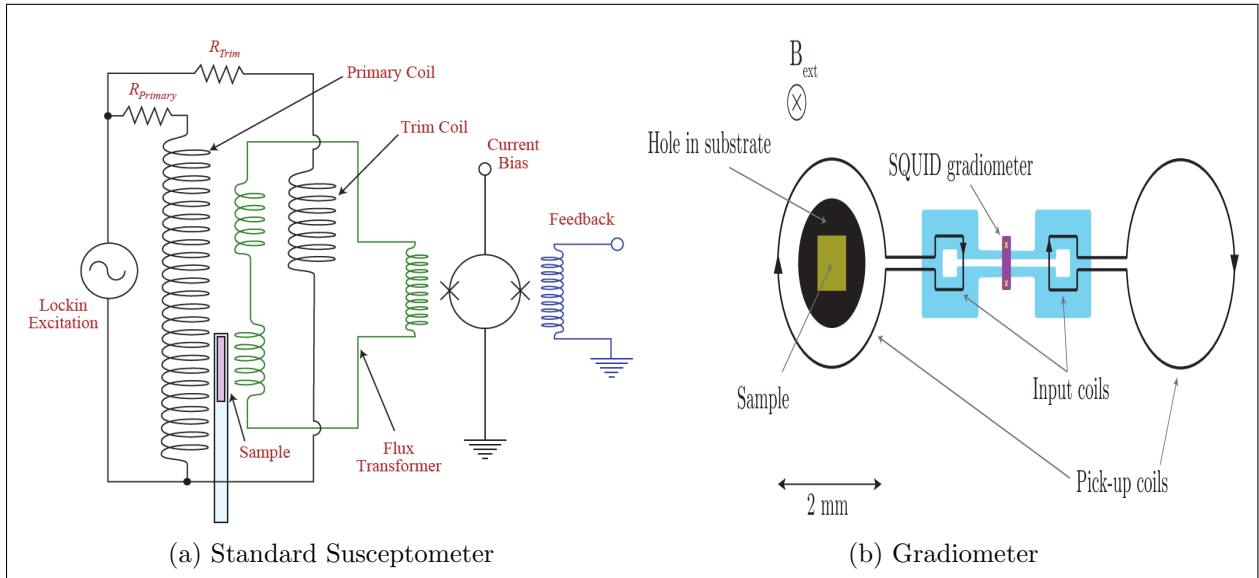
Figure 4.12: In (a), the setup of a standard susceptometer running with a single loop d.c. SQUID is shown, from [65]. In (b), a d.c. SQUID running as a gradiometer, from [49]. The gradiometer setup is drastically simplified from the standard susceptometer, and can run in a magnetic field.
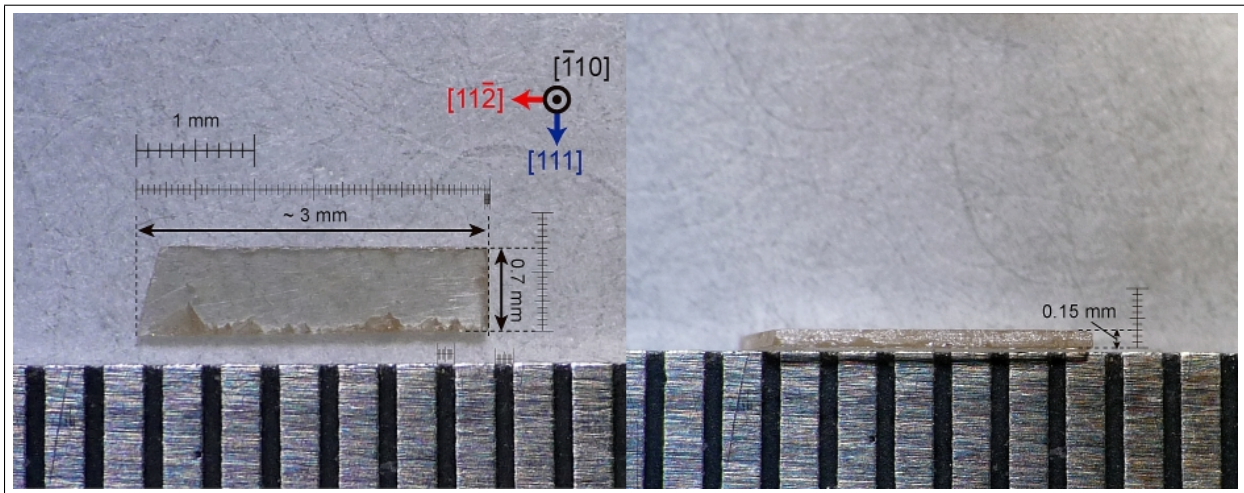
Figure 4.13: $Dy_2Ti_2O_7$ sample provided by Hiroshi Takatsu at the University of Tokyo, showing the measurements, orientation directions, and color of the sample.

then glued flat onto the SQUID Silicon chip using Vacuum Grease. This allowed very accurate alignment of the $[1\,1\,1]$ direction and the $[1\,1\,\overline{2}]$ direction with respect to the d.c. SQUID. A stainless steel threaded rod was used to lower the setup into the homogeneous high field region of the 8.5 T magnet, and a Copper wire was used to heat sink the SQUID setup to the lowest stage connected to the mixing chamber. It is expected that this setup has alignment accuracy as good as the X-ray Laue orientation for the measured $Dy_2Ti_2O_7$ crystal of $1°$. The alignment accuracy is confirmed by studies of on-chip SQUIDs in high magnetic fields. In [11], one such study found that for similar thickness SQUID chips as the one used in this thesis, in a field of 1 T, the SQUID will turn from superconducting to normal if alignment is any worse than approximately $0.5°$. The in-field measurement in this thesis worked at 1 T, putting a qualitative upper bound on the alignment of the SQUID with respect to the applied field.

(a) Gradiometer setup schematic   (b) Gradiometer setup
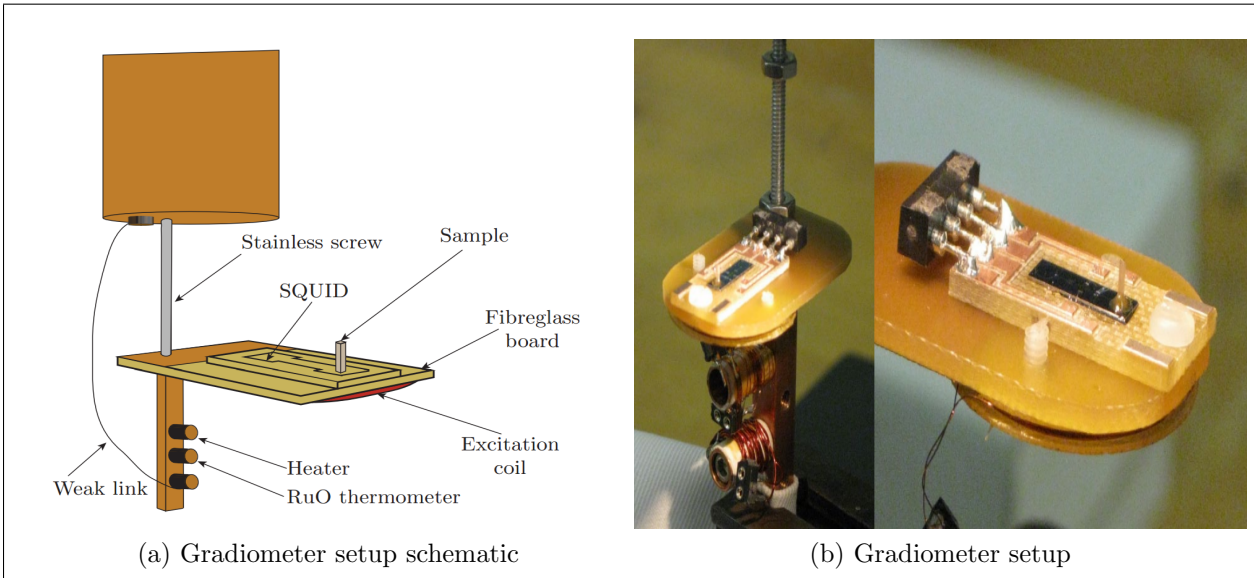
Figure 4.14: The SQUID gradiometer setup used for the zero field and in-field a.c. susceptibility data of this thesis. This gradiometer is the same one described in [49], and both images are from [49].

For the in-field a.c. susceptibility data, the a.c. susceptibility setup was the exact same as the zero field setup. The current supply for the 8.5 T magnet was a Kepco BOP 20-10M model bipolar power supply. The calibration provided from the company who made the 8.5 T magnet was used to determine the applied field values. The field was ramped at a rate of roughly 1-3 mT/minute when switching between field values. The data taking order was, warm to 1.2 K, ramp the field to the next field value, wait approximately 6 hours,

then start taking data and step down in temperature. Each susceptibility data set took approximately 10 hours to go from 1 kHz to 1 mHz (zero field), and approximately 3 hours to go from 1 kHz to 10 mHz (in-field). In addition to this, the sample was given 1 hour to relax to a new fridge temperature with temperature changes of 25 mK. In the in-field $Dy_2Ti_2O_7$ data, no hysteresis was observed in the temperature/field range measured for the given ramp rate.

To determine the calibration constant which linearly converts the flux-locked-loop output voltage of the SQUID to susceptibility units, one can measure a standard on the SQUID setup. A standard is a material with a well known susceptibility value, such as a superconducting Lead sphere, which can then be used to determine the voltage to susceptibility conversion. One can also do a demagnetization correction on the same sample with two different geometries, and determine the calibration constant by assuming the true bulk demag corrected susceptibility of the sample is the same for both geometries. This method is described well in [65]. This method is better than the superconducting sphere method, as the assumption that the bulk susceptibility of a material is the same if it is just cut into two different geometries is more reasonable then assuming perfect geometry of a cut crystal. This method also simultaneously corrects the data for demagnetization effects, and gives the value of the calibration constant. The demagnetization correction corrects for the difference between the measured or apparent susceptibility (χ_a) and the material's true susceptibility (χ) according to Equation 4.2. This correction arises when the induced magnetization of the sample affects the distribution of the applied magnetic field. For an ellipsoid geometry, the effect can be combined into a single constant called the demag factor, N, as shown in Equation 4.2. This method explicitly assumes that two separate cool-downs of the dilution refrigerator, one where the sample has one geometry, and another where it has been cut to have a different geometry, are very similar. Special care must be taken to ensure the only difference between the two data sets on the two sample geometries is the demagnetization effect. In reality there are many effects which can cause the two data sets to differ by more than just this effect, such as misalignment of the crystal during the second cool-down, or changes in the noise levels between the two cool-downs. If one is careful, these effects can be minimized and the demag correction performed, however the data must also be extremely clean for the above method to work. The calibration factor is found in a least squares minimization of the differences between the bulk susceptibilities of the two different geometry samples, and so its success is very sensitive to noise levels. Thus, the in-field data presented in this thesis was not demag corrected due to the large amount of noise in the data. This noise was not completely eliminated even after the addition of the many noise reduction techniques mentioned in the previous section, it was only reduced. The zero-field data was not demag corrected

to keep consistency with comparison to the in-field data, and because of the fact that the zero field Arrhenius region has already been mapped out with a demag correction in other work [64].

The demag correction changes the shape of the susceptibility curves, and shifts their location in frequency space, to an extent which depends on size of the demag factor N. A small demag factor can be achieved by having sample dimensions which are long along the measurement direction, and short along the other two dimensions. In the limit of small N, the demag correction is essentially just a linear shift to the location of the χ'' curves, and the shift is more or less temperature independent. The sample used in this thesis had a demag factor of 0.042 along the measurement direction, which is considered small. This means that the barrier to relaxation, which is calculated off the slope of multiple χ'' peak locations at low temperatures, is expected to not change much after a demag correction. This is because all the points should shift by roughly the same amount. The full-width-half-max, Cole-Cole plots, and the dynamical correlation functions are also expected to be minimally affected by a demag correction, as these values are calculated off the χ'' peak shape. For a linear shift with small N, the shape is not expected to change much.

For the in-field susceptibility data taken in this thesis, there are two demagnetization corrections, one correcting the applied field along the main field direction of [1 1 1], and one correcting the susceptibility measurement along $[1\,1\,\bar{2}]$. The one along the susceptibility measurement direction was not performed in this thesis for reasons mentioned above, but it is expected to minimally affect the main features presented. The correction along [1 1 1] can be performed by assuming the sample is relatively similar to previously measured $Dy_2Ti_2O_7$ crystals, and using the equation $B_{eff} = B_a - 4\pi NM$. In this equation, B_{eff} is the effective field on the sample, B_a is the actual applied magnetic field, N is the demagnetization factor along [1 1 1] (0.194 for this sample), and M is the magnetization of the sample. Since the majority of the in-field temperature scans were taken in the Kagome ice regime, the induced magnetization of the sample along [1 1 1] is expected to be within approximately 10% of $3.33\frac{\mu_B}{Dy}$, which is the Kagome ice state magnetization value as measured in [54]. Using this value for M for all the field values, with N = 0.194, one can find that the effective fields are approximately 25 ±2.5 mT less than the applied fields. Thus, when field scans at 400 mT,500 mT,600 mT and 700 mT are referred to, which are all very close to the Kagome ice state for the temperature range of the data in this thesis, the demag corrected field values are approximately 375 mT, 475 mT, 575 mT, and 675 mT. At 1 T, the samples magnetization is expected to be closer to $4\,\frac{\mu_B}{Dy}$ as measured in [54], giving a true field of approximately 970 mT. The demagnetization effect is clearly important for these materials which have such large magnetic moments, and a demagnetization correction, which could be performed in future work once the in-field noise is reduced, could improve the data

presented here. A proper demagnetization correction is not expected to change the main results presented significantly.

$$\chi' = \frac{\chi_a' - 4\pi N (\chi_a'^2 + \chi_a''^2)}{(1 - 4\pi N \chi_a')^2 + (4\pi N \chi_a'')^2}$$
$$\chi'' = \frac{\chi_a''}{(1 - 4\pi N \chi_a')^2 + (4\pi N \chi_a'')^2}$$

(4.2)

Chapter 5

Experimental results

5.1   Zero field a.c. susceptibility of $Dy_2Ti_2O_7$

Since $Dy_2Ti_2O_7$ is such a well studied material, with a.c. susceptibility curves measured previously from the high temperature limit down to below 1 K, it was easy to compare zero field susceptibility data to other literature. Due to the setup being new, and the sample being new, the a.c. susceptibility was measured in zero field along the $[11\bar{2}]$ direction (along the 3 mm length) of the $Dy_2Ti_2O_7$ crystal shown in Figure 4.13, between 525 mK and 1200 mK. This zero field measurement allowed for a thorough analysis of the characteristics of this new $Dy_2Ti_2O_7$ sample, which were found to be in qualitative agreement with the main features of previously measured results. This simultaneously showed the accuracy of the SQUID magnetometer setup, and also characterized the crystals properties for comparison to in-field behavior. The zero field a.c. susceptibility is presented in Figure 5.1 and Figure 5.4, with the former measured between 600 mK and 1200 mK before the addition of many of the noise reductions to the system (such as magnetic and vibrational isolation), and the latter between 525 mK and 750 mK. The scans before the noise reduction techniques were in place only go down to 10 mHz, where the noise pickup began at the time. In addition to this, there was no background subtraction made on the data of Figure 5.1, due the dilution fridge blocking before it could be taken. As such, only the relaxation times are extracted from this data. They are expected to not change much even after a proper background subtraction as it is clear the background for this case only affects the data significantly after approximately 100 Hz, outside the range of the peaks in χ''.

On a second cooldown, the zero field data was measured again in the range of 525
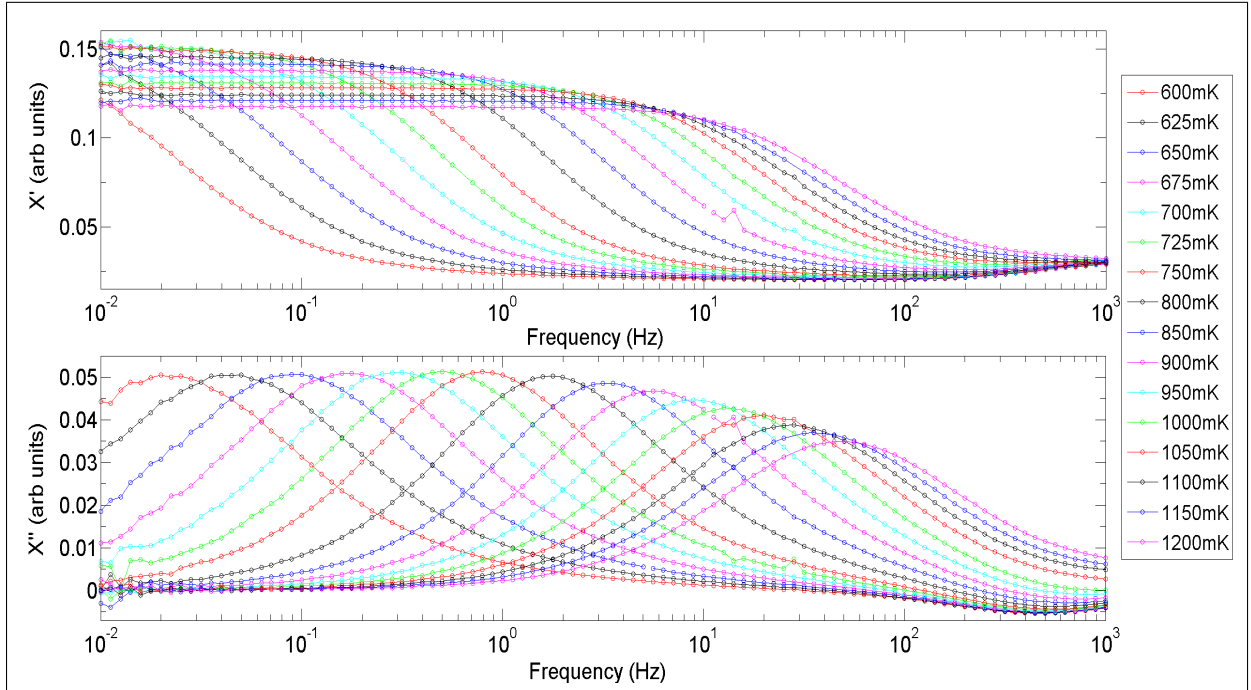
Figure 5.1: Zero field a.c. susceptibility data of $Dy_2Ti_2O_7$ between 600 mK and 1200 mK. measured with a bandwidth of 10 mHz to 1 kHz, before the setup was improved and with no background subtraction. Temperatures are 600 mK on the left (red), increasing in 25-50 mK steps to 1.2 K on the right (magenta).

mK to 750 mK with the the noise improvements allowing the data to be taken down to 1 mHz. This data had a background subtraction made as well. In Figure 5.2, the a.c. susceptibility was measured between 525 mK and 750 mK with the new setup and no background subtraction yet. Deviation from the expected shape is seen in the high frequency regime as before in Figure 5.1, namely around 3 Hz and 400 Hz, where the real and imaginary parts of the susceptibility deviate from 0. It is expected that both χ' and χ'' should go to zero in the high frequency limit (a frequency higher than the characteristic relaxation time of the system, which is the peak in χ''), due to a filtering-like effect of the spins being unable to respond at such quick timescales.

The gradiometer actively cancels noise, but not all flux sources are cancelled perfectly. These sources define a background of flux, which reflects the fact that d.c. SQUIDS see no absolute difference in a zero field background as compared to an in-field background, they only measure a relative difference from some chosen reference due to the periodic
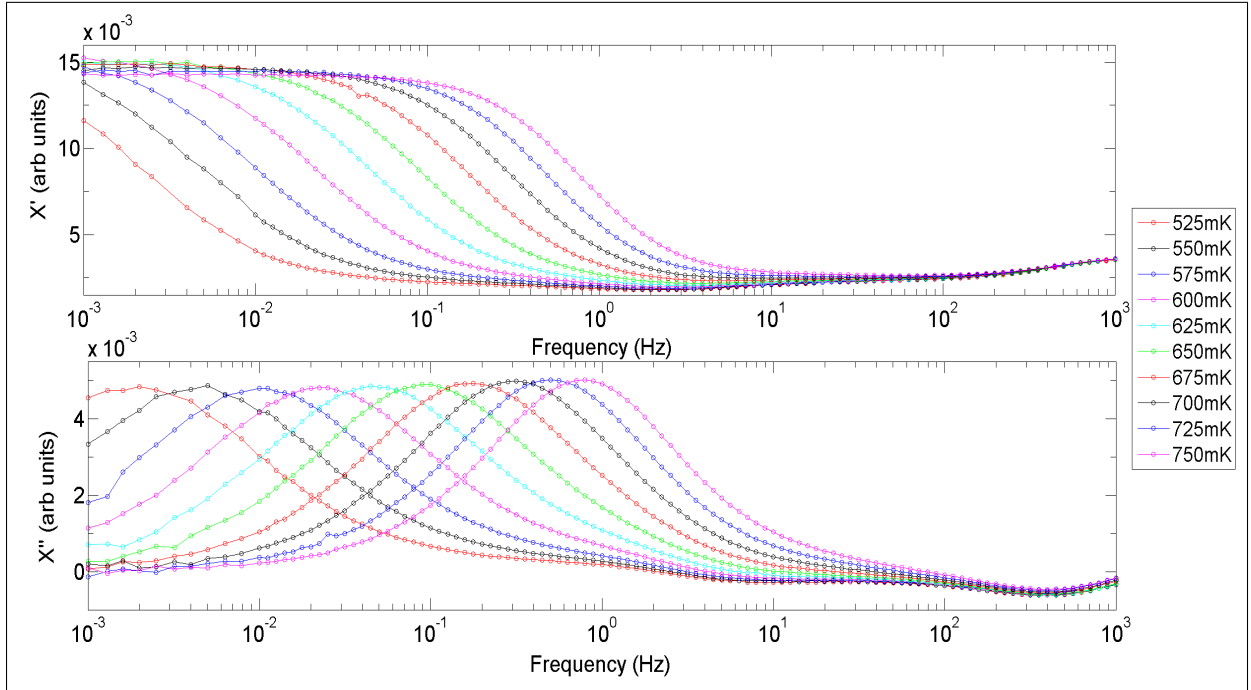
Figure 5.2: Zero field a.c. susceptibility data of $Dy_2Ti_2O_7$ between 525 mK and 750 mK, measured with a bandwidth of 1 mHz to 1 kHz before the background subtraction. Temperatures are 525 mK on the left (red), increasing in 25 mK steps to 750 mK on the right (magenta).

nature of the $V - \Phi$ curve. This background flux should be a constant in temperature and frequency, and constitutes the 'zero' of the SQUID. This means it should be subtracted away point by point from the a.c. susceptibility curves measured at every temperature so that the remaining signal is due to strictly the sample. This is similar to balancing a standard susceptometer with a trim coil as mentioned in the previous section. As mentioned previously, the background is taken by cooling the fridge to a very low temperature, where the sample being studied does not respond to the primary coil field within the bandwidth being measured. In this case, the bandwidth of interest was 1 mHz to 1 kHz. All the background scans in this thesis were performed below 0.1 K, where the magnetic response time of $Dy_2Ti_2O_7$ is expected to be well below 1 mHz. In that case, any SQUID output signal is due entirely to background effects, and can thus be subtracted away. The background scan for the zero field data was taken at 70 mK and is presented in Figure 5.3.

In the background scan, the peaks at around 3 Hz and 400 Hz can be seen in more
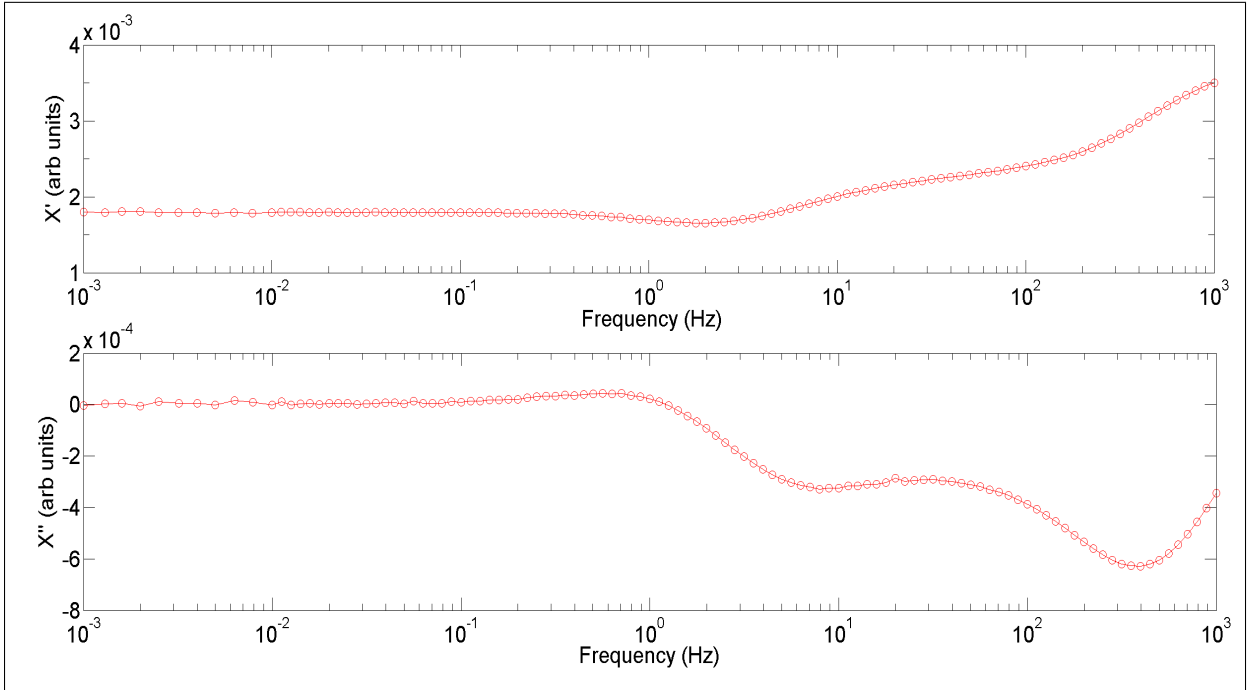
Figure 5.3: The zero field background a.c. susceptibility taken at 70 mK between 1 mHz and 1 kHz. The $Dy_2Ti_2O_7$ spins are frozen out at this point, so any signal is strictly due to background effects.

detail. In the low frequency limit, the signal is completely flat, showing no contributions from the sample, which has a characteristic relaxation time much lower in frequency than the bandwidth of the measurement. This background scan was found to be temperature independent, by measuring it between 100-250 mK in 25 mK steps. This was true for all the zero field scans, as well as the in-field scans presented later. After the background scan is subtracted point by point from the susceptibility data presented in Figure 5.2, the resulting curves are due to just the sample's signal, and these curves are shown in Figure 5.4. After the background is subtracted away, the expected shape of each curve is obtained both in the low and high frequency limits in both χ' and χ'', showing the effectiveness of the background subtraction method.

At this point, it would be a good idea to compare these a.c. susceptibility curves to some other experimental results. A combination of experimental work by Matsuhira et al. [35, 36], Snyder et al. [57] and Yaraskavitch et al. [64] quantified the characteristic magnetic relaxation time of $Dy_2Ti_2O_7$ from 20 K down to 0.5 K. These data sets are shown in Figure 5.5. The measurement made in [36] used a two-tau model to extract the relaxation
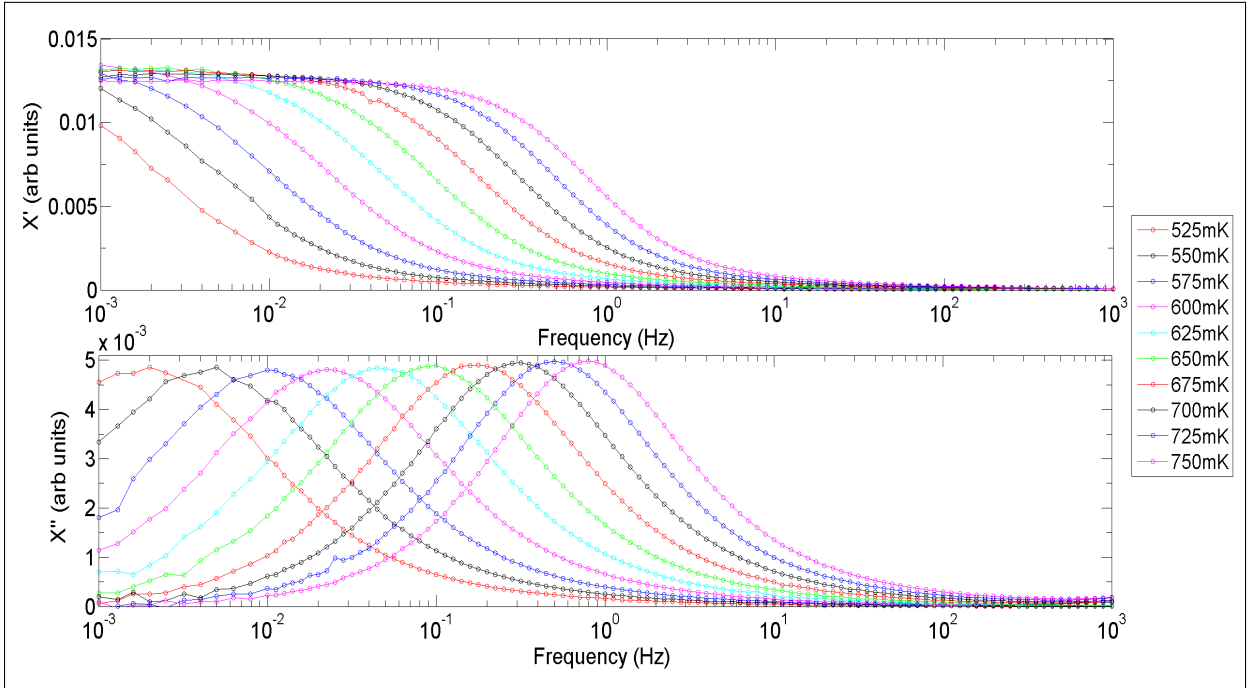
Figure 5.4: Zero field a.c. susceptibility data of $Dy_2Ti_2O_7$ between 525 mK and 750 mK, with a bandwidth of 1 mHz to 1 kHz, after the background subtraction. The expected shape of each curve is restored, showing the effectiveness of the background subtraction method. Temperatures are 525 mK on the left (red), increasing in 25 mK steps to 750 mK on the right (magenta).

times from the a.c. susceptibility data. The data in this thesis was not analyzed in this way, thus this data has been omitted from Figure 5.5 for clarity; however, an important remark is the results of [36] are in nearly perfect quantitative agreement with the results of [64], as discussed more in [49]. Theoretical work done by Jaubert et al. [30, 23] is also plotted in Figure 5.5. This theoretical work attempted to reproduce the experimental low-temperature quantum tunneling region (quasi-plateau region) of the magnetic relaxation through a set of metropolis dynamics simulations. These simulations used the statistics from both the dipolar spin ice model in the canonical ensemble [23], and a Coulomb gas of interacting monopoles in the grand canonical ensemble [30]. The differences between the two models is explained in more detail in section 3.1. The key difference was the dipolar spin ice model simulation considered 3-in-1-out/3-out-1-in excitations out of the 2-in 2-out spin ice ground state on the pyrochlore lattice, whereas the Coulomb gas model simulation looked at monopoles interacting through a magnetic Coulomb interaction on

a diamond lattice. With very different physics, both simulations resulted in the same qualitative shape measured by [56], and agreed with the experimental data fairly well up to around 1.2 K. Below this temperature, the simulations began to deviate from the last few measured points of the data in [56]. The data from [64] deviates even more so from the simulations for both the higher temperatures and lower temperatures of the tunneling regime. The higher temperature disagreement is most likely due to normalization of the simulations to the data of [56], and the lower temperature disagreement is most likely due to demagnetization effects. Incidentally, the data of [56] was also missing a factor of 2π when converting from frequency to relaxation time, resulting in a simple constant shift to all the frequency values. The low temperature shape of the data in [64] was found to be in strong disagreement with the simulations. In addition to this, the barrier to relaxation was expected to be around $6J_{eff} \sim 6.6K$ for the low temperature data, but was found instead to be 9.8 K, in disagreement with both models.
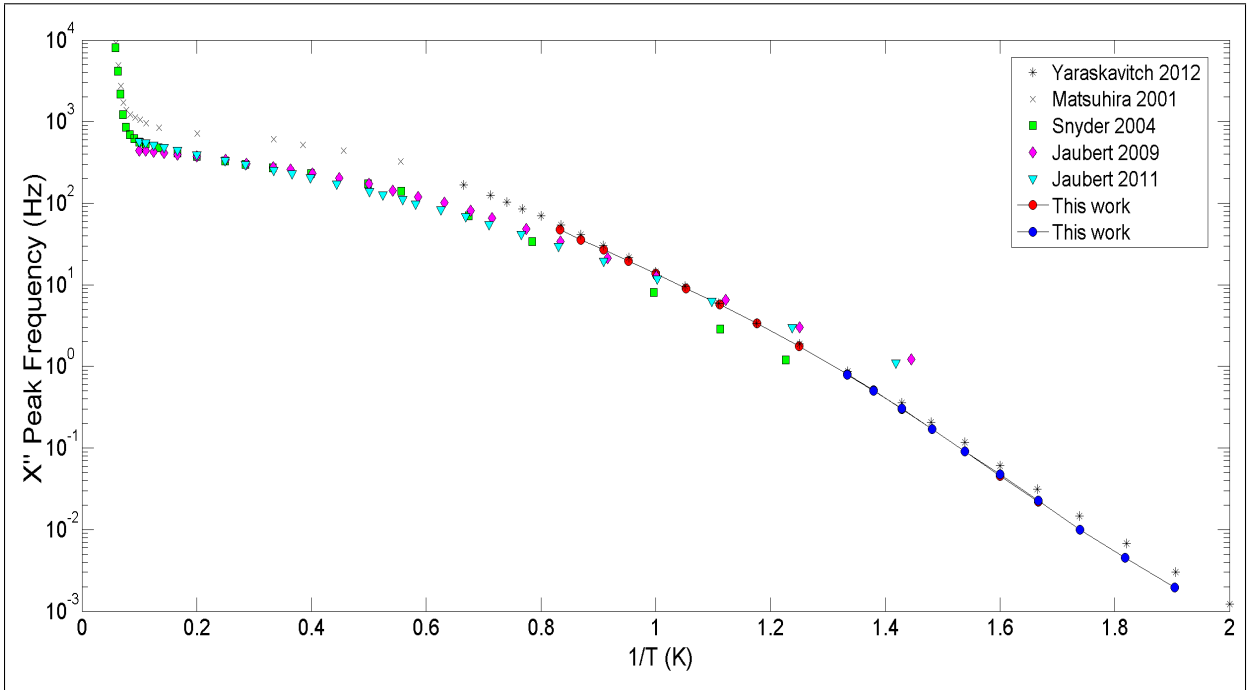
Figure 5.5: Comparison of the characteristic relaxation time measured through the a.c. susceptibility data presented in Figure 5.4 and Figure 5.1 to other works [35] (Matsuhira 2001), [57] (Snyder 2004), [64] (Yaraskavitch 2012), [30] (Jaubert 2009), and [23] (Jaubert 2011).

In Figure 5.5 we see that the agreement with a different $Dy_2Ti_2O_7$ crystal, with a new

61

SQUID magnetometer setup, on a new dilution fridge, is in very good agreement with the data of [64]. The small differences are seen in the high and low temperature limits. Small deviations are seen in the characteristic relaxation time above around 1 K between this data and [64]. This is most likely due to there being no background subtraction in the data from Figure 5.1, and these high temperature points have peaks near to where the background signal is largest. Deviation from [64] is also seen in the low temperature limit, below approximately 750 mK. Data below this temperature is considered the Arrhenius relaxation region for the sample, and it is found that the sample had a barrier to relaxation of 10.9 K $\pm$ 0.3 K, whereas it was 9.8 K for the previously measured data [64]. Having a difference in the barrier to relaxation of around ~ 1 K between this sample and the data of [64] has been observed before, where the barrier to relaxation was found to be 9 K in the Arrhenius regime for a different $Dy_2Ti_2O_7$ sample measured in [50]. The sample measured in [50] was performed on the exact same SQUID magnetometer setup as the data in this thesis, and a barrier to relaxation of 9 K was measured for $Dy_2Ti_2O_7$ in this low temperature Arrhenius regime.

A thorough study of the barrier to relaxation for multiple $Dy_2Ti_2O_7$ crystals with slightly varying properties has not been published to date, so it is unclear whether the barrier to relaxation is sample dependent or due to systematic errors arising from different experimental setups. In the case of the data in this thesis, the most likely cause of systematic errors would be demagnetization effects and temperature offsets in the thermometry of the sample arising from the applied heat used to run the SQUID magnetometer. The d.c. SQUID experiences a heat load of approximately 1 nW while running due to the 10 Ω shunt resistance and 10 μA bias current. This heat load is relatively close to the sample, as seen in the picture of the setup in Figure 4.14. In theory one could calculate at what temperature this heat load would become a problem, however in reality the thermal link between the sample and SQUID due to the General Electric varnish 7301 link can't be calculated accurately. One can set up an experiment with a paramagnetic thermometer such as Cerium Magnesium Nitrate running in an identical d.c. SQUID gradiometer setup with similar thermal links, and look at the deviations from this thermometer versus a calibrated resistance thermometer. This was attempted on the new dilution refrigerator setup, however sample quality issues with the Cerium Magnesium Nitrate crystals resulted in the experiment not working. Quantifying thermometry offsets due to the SQUID heating on the model GRAD 2D-10 gradiometers could be the subject of future work. In the case of this data, no plateau was seen in the low temperature relaxation frequencies (a sign of SQUID heating). Demagnetization effects act to increase the value of relaxation frequencies, shifting data points in Figure 5.5 upwards, and this effect becomes more severe as temperature is lowered. This is the most likely explanation of deviations between this work

and [64]. The uncertainty of ± 0.3 K was found by fitting minimally sloped and maximally sloped lines to the Arrhenius region, and taking the difference in these slopes from the line of best fit. A thorough analysis of the uncertainty on the barrier to relaxation was not mentioned in depth in [64] and [50].

In addition to the magnetic relaxation times, the shapes of the curves are also an important way to quantify the new setup. In Figure 5.6, subplot (a), the spectral widths of the data from Figure 5.4 (called dataset 1) and Figure 5.1 (called dataset 2) versus temperature are given. These widths are compared to the ones obtained on a different $Dy_2Ti_2O_7$ sample from [64]. The agreement is good, with spectral widths between $\sim$ $1.4-1.7$ decades for this data, in agreement with $\sim 1.35-1.6$ decades for $Dy_2Ti_2O_7$ reported in [64]. The difference in full-width-half-max values between datasets 1 and 2, which are both on the same sample, arises from dataset 2 having no background subtraction. The background subtraction affects the spectral width of all the data from at least 800 mK to 1.2 K, as can be seen in the raw data of Figure 5.1, as the hump in the high frequency regime around 100 Hz. Below 800 mK, the two datasets begin to agree with each other reasonably well because the background subtraction begins to affect the spectral width less and less as the χ'' peak moves to lower frequency as temperature is lowered. The spectral widths of dataset 1 are considered accurate, due to the data having a background subtraction. This small difference between datasets 1 and 2, and the data from [64], is most likely due to this data not having a demagnetization correction. The width of the spectra is related to the distribution of relaxation processes in the material, with a spectral width of 1.14 being the theoretical width for a single relaxation mode following a Casimir du Pre relation [56]. The spectral width of $\sim 1.4 - 1.7$ for this data is near to the single relaxation mode limit, and is seen clearly in the Cole-Cole plot for this data in Figure 5.7, where a single relaxation mode corresponds to a semicircle in the Cole-Cole plot. In Figure 5.7, the Cole-Cole plots for datasets 1 and 2 are shown. The data in Figure 5.1 had a constant of 25.7 mV subtracted away from χ' and 1.4 mV from χ'' as a 'background subtraction', as these were the values which would set the high frequency data of the lowest temperature scans of the data in dataset 2 to 0, as they should be in the high frequency limit. The data of dataset 2 was also divided by 10 to normalize it to the same amplitude as dataset 1, because a 10:1 voltage divider was used on dataset 1 but not 2. The semi-circular behavior is clearly seen in the Cole-Cole plots for both data sets, showing there is a narrow distribution of relaxations in this material, as was found in [64]. In addition to this, the Cole-Cole plot allows for the d.c. susceptibilities to be extracted, by looking at where the curves intercept the χ' axis at the non-zero χ' point. These are also shown in Figure 5.7. Also plotted is d.c. susceptibility data from [65], scaled by a factor of 31 to scale it down to arbitrary units to compare to this data. Once again we find

the agreement is good at high temperatures, and deviations appear at lower temperatures. The observed differences in the d.c. susceptibility values between this work and [65] can be explained as a demagnetization effect. Taking Equation 4.2 and looking at χ' in the case of χ'' is equal to 0, as it is in the d.c. limit, it is easy to show a demagnetization correction increases observed d.c. susceptibility values. This is consistent with the deviations seen in Figure 5.7.

(a) Spectra full-width-half-max

Dataset 1

Dataset 2

(b) Normalized χ'' curves
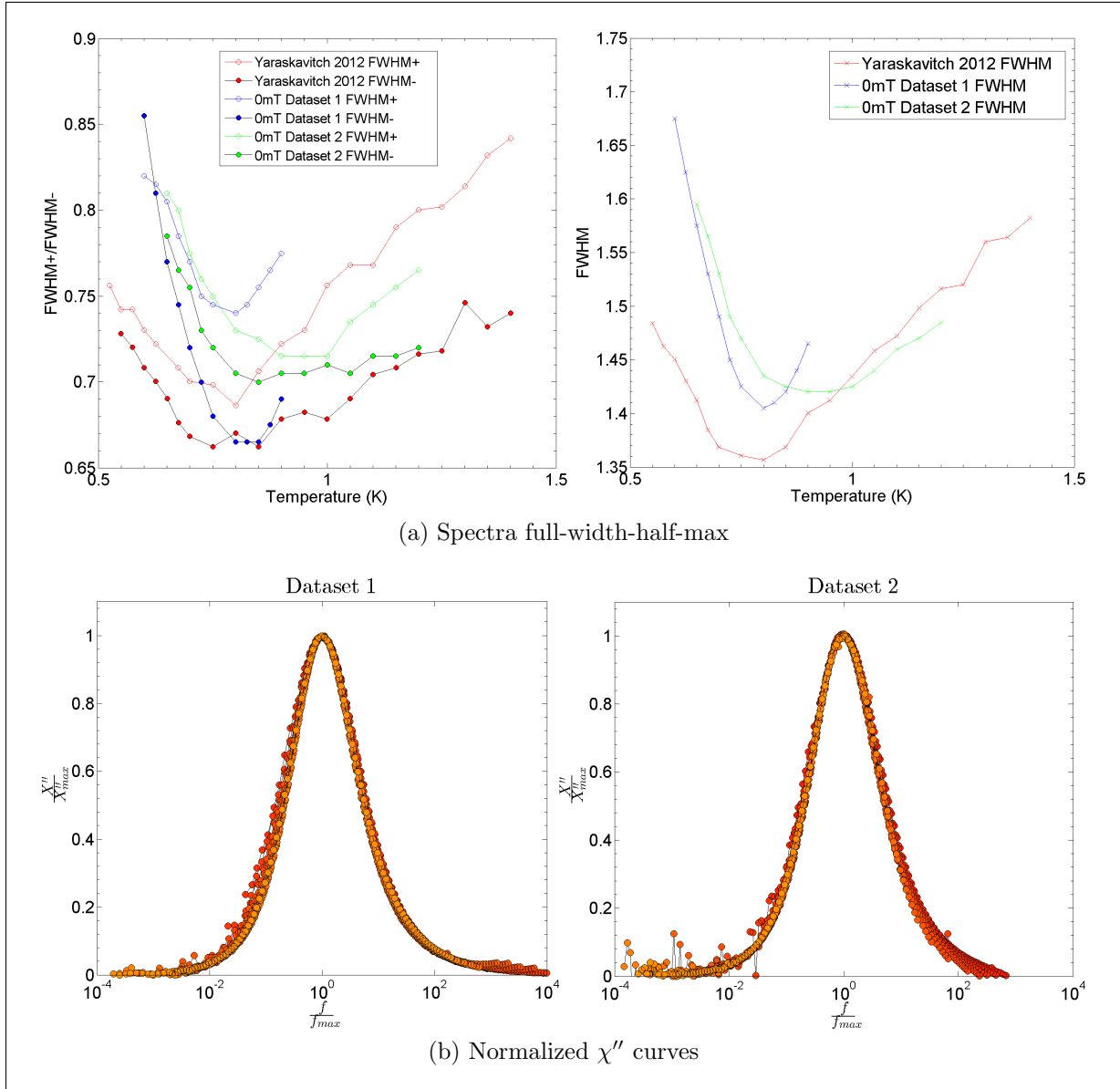
Figure 5.6: Full-width-half-max versus temperature (a), and normalized χ'' curves (b) for the data of Figure 5.4 (called dataset 1) between 600 mK and 900 mK and Figure 5.1 (called dataset 2) between 650 mK and 1200 mK. These values are compared to work done in [64]. The normalized curves are labeled as a gradient from red to orange with red being lower temperature.

(a) Cole-Cole plots

(b) D.c. susceptibilities
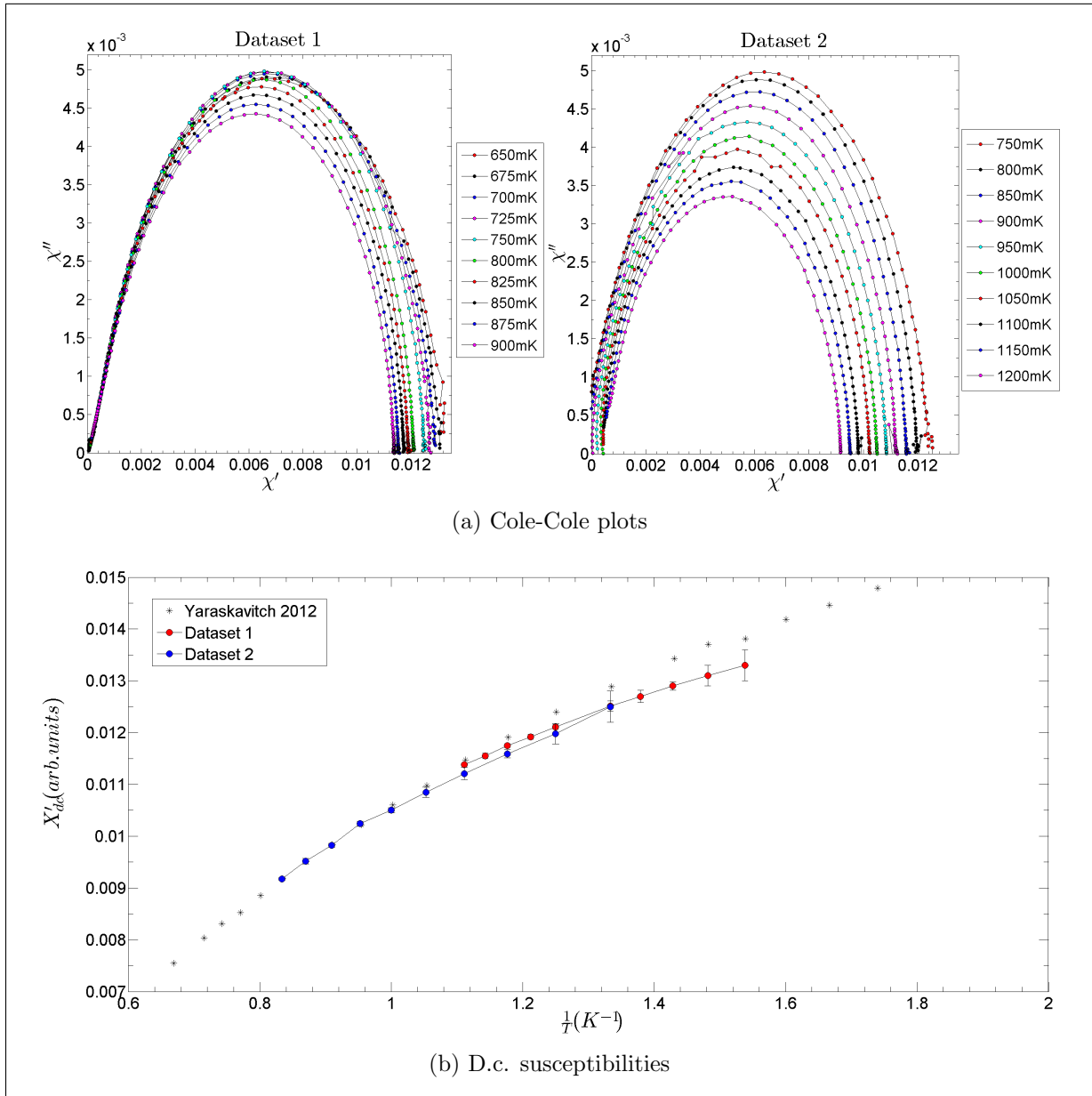
Figure 5.7: Cole-Cole Plots (a), and d.c. susceptibilities (b) for the data of Figure 5.4 (called dataset 1) between 650 mK and 900 mK and Figure 5.1 (called dataset 2) between 750 mK and 1200 mK. The d.c. susceptibilities are compared to those measured by [65], which are scaled by a factor of 31 to align the two data sets to the data measured in [65] at high temperatures, where demagnetization effects should have a smaller impact.

The correlation functions were calculated for the zero field data. The motivation for this was to look at possibly interesting behavior in their shapes given such a large (~ 2 K) change in the barrier to relaxation, compared to the work of [50]. To obtain the correlation function, one can use the fluctuation dissipation theorem [28] to derive an equation which transforms frequency domain a.c. susceptibility data to time domain d.c. magnetization data. The form of such a transformation is given in Equation 5.1.

$$C(t) = \langle M(t)M(0)\rangle = 2kT \int_{-\infty}^{\infty} \frac{\chi''(w)}{w} \cos(wt)dw \qquad (5.1)$$

To perform this Fourier transform, a suitable fitting function must be fit to the χ'' data in order to provide a continuous integrable function. The function that was chosen to fit the a.c. susceptibility data is given by Equation 5.2, and was used in the analysis of [50] as well, motivated by [5]. This function represents relaxation in a glassy system, and was found to fit to the experimental χ'' data better than a single or double Debye model. The resulting fits are presented below for the data of Figure 5.4 between 625 mK and 750 mK. The data between 525 mK and 600 mK was not included because of the χ'' curves being too close to the edge of the measurement bandwidth, resulting in inaccurate fits to Equation 5.2. The correlation functions for the data of Figure 5.1 were not calculated due to lack of a background subtraction, which could affect the shape of the χ'' curves and thus the correlation function. The results are presented below.

$$\chi''(w) = \frac{1}{[(\tau w)^{\alpha_1 n} + (\tau w)^{-\alpha_2 n}]^{\frac{1}{n}}} \qquad (5.2)$$

The correlation functions obtained in Figure 5.8 show similar behavior to those reported in [50], namely the correlation functions have stretched exponential behavior of the form $e^{-(\frac{t}{\tau})^{\beta}}$ over some time during the magnetization decay, and then the relaxation turns into a long-time algebraic tail. The stretched exponential behavior can be seen more clearly in a plot of $ln(-ln(C(t)))$ versus $ln(t)$, where according to the stretched exponential behavior, would show as a straight line with slope β and y-intercept of $-\beta ln(\tau)$. Here, τ is the relaxation time at that temperature. The corresponding τ values as a function of $\frac{1}{T}$, and the corresponding β values as a function of $\frac{1}{T}$ are presented in Figure 5.9, along with the linear fits represented as a black line with crosses. We see that the barrier to relaxation of these fits is found to be 10.8 K as seen in the top left inset of Figure 5.8, which is consistent with the a.c. susceptibility curves used to calculate them. Also, the measured β values were between approximately 0.73 and 0.77, which fall within the range of 0.7-0.8 measured in [50]. The correlation functions for the data below 625 mK were not calculated due to

67
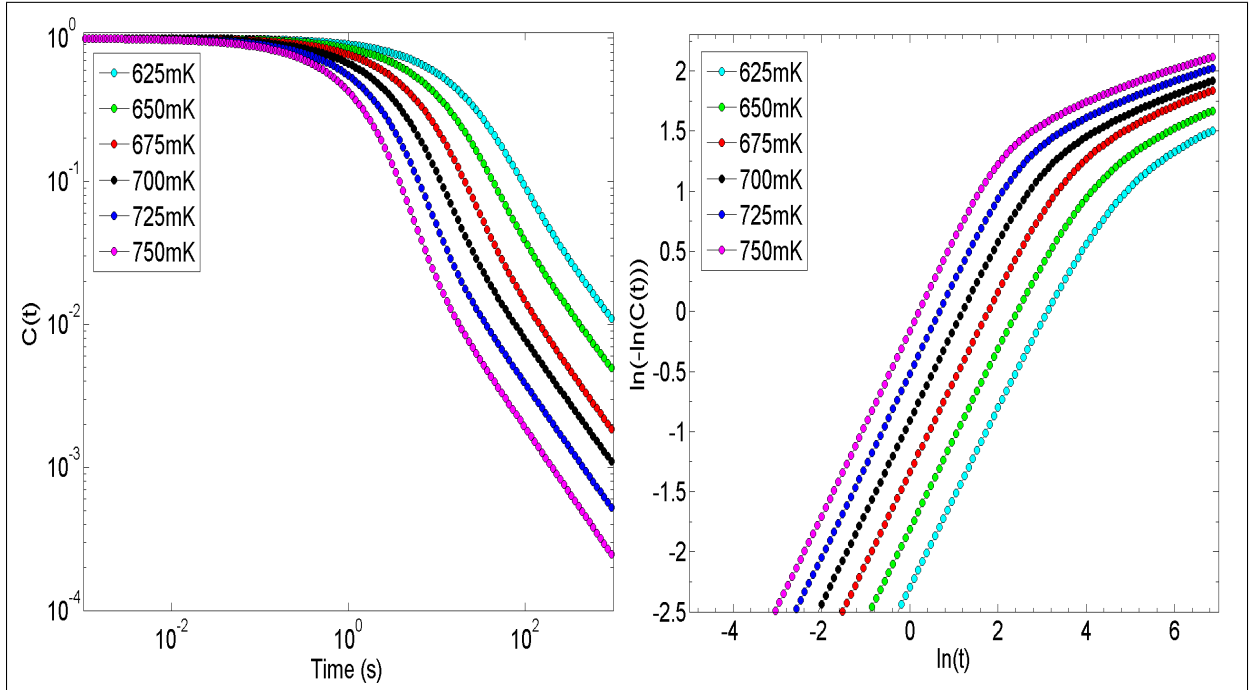
Figure 5.8: Correlation functions for the data of Figure 5.4, corresponding temperatures are shown in the legend, going from 750 mK on the left to 625 mK on the right.

the χ'' curves having peaks that are too close to the edges of the bandwidth measured, namely 1 mHz to 1 kHz. It was found that without at least one full-width-half-max of noise free frequency data centered around the χ'' peak, the shapes of the correlation functions at long times were strongly dependent on the number of data points in the tails on either side of the χ'' peak. Taking the same data set, but simply removing a few points at either end of the χ'' data (in the tail region) caused the correlation functions to deviate significantly with the removal of only a couple data points. In addition to this observation, it was found that the correlation functions cannot be calculated for data without a proper background subtraction (such as the data of Figure 5.1). The fit to Equation 5.2 is strongly dependent on the shape of the shape of χ'', but also the behavior of the tails, as mentioned before. Without a proper background subtraction, the tails aren't useful data, and so the correlation functions lose their meaning. In the end, the fits of Equation 5.2 were performed in Matlab, and the fit parameters were exported to Mathematica where the Fourier cosine transform function (Equation 5.1) was used to arrive at the correlation functions.

As can be seen through Figure 5.5, Figure 5.8, and Figure 5.9, the crystal of $Dy_2Ti_2O_7$ measured in this thesis has all the previously measured low temperature characteristics
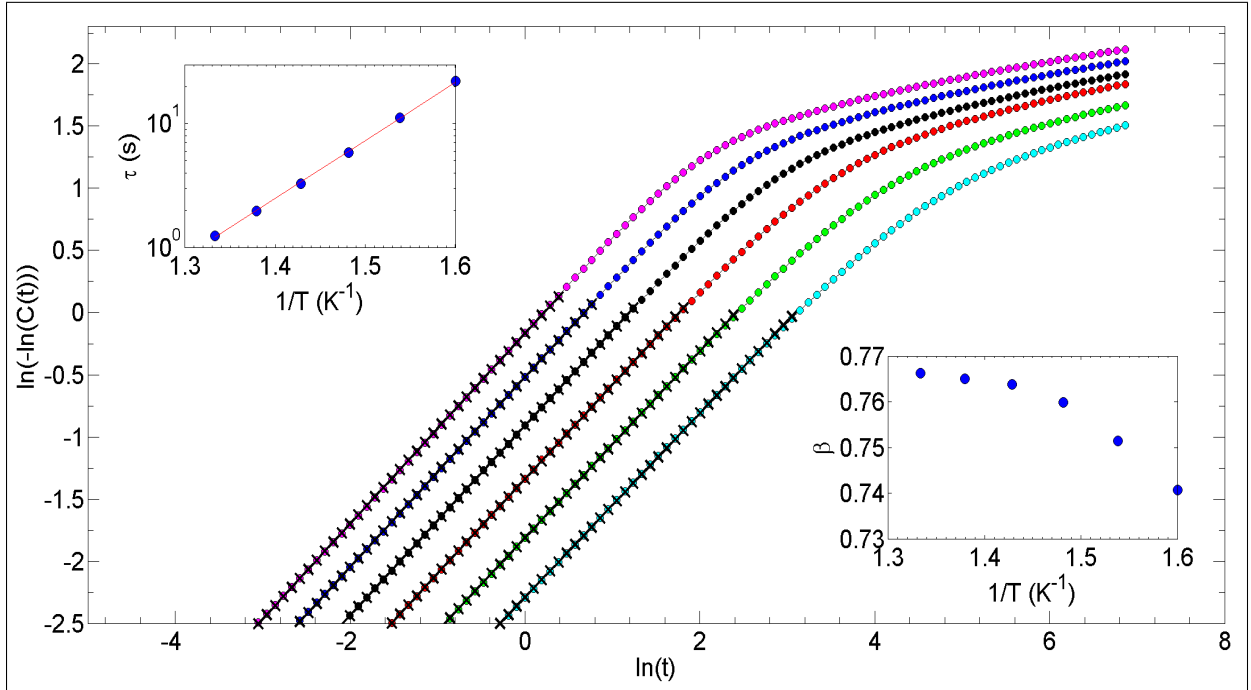
Figure 5.9: Correlation functions for the data of Figure 5.8 fitted to a stretched exponential. The temperatures are 750 mK, 725 mK, 700 mK, 675 mK, 650 mK, and 625 mK going from left to right. The linear fits appears as a black line with crosses. The stretch parameters are plotted in the bottom right inset as a function of $\frac{1}{T}$. The relaxation times are plotted in the top left inset as a function of $\frac{1}{T}$, and they give a barrier to relaxation of 10.8 K, consistent with the a.c. susceptibility data.

for $Dy_2Ti_2O_7$. The crystal has an Arrhenius relaxation regime below around 750 mK, with a barrier to relaxation of approximately 10.9 K, as compared to previously measured values of 9.8 K [64] and 9 K [50]. The crystal also has correlation functions which exhibit stretched exponential behavior when transformed to the time domain using the fluctuation dissipation theorem (Equation 5.1), followed by a long-time algebraic tail as seen before in [50]. The stretch exponents β of this crystal between 0.73 and 0.77 fall into the previously observed range of 0.7-0.8 [50], and the barrier to relaxation from the stretched exponential fits was found to be 10.8 K, consistent with the barrier from a.c. susceptibility measurements. In summary, it can then be said that this crystal of $Dy_2Ti_2O_7$ has all the same characteristics of previously measured $Dy_2Ti_2O_7$ data, and so is consistent with all the corresponding theories that were developed around this data. This also shows that the new SQUID magnetometer setup on a new dilution refrigerator has been successful, seeing

69

as how all the previously measured values were taken on different dilution refrigerators with different setups. With the zero field data for this crystal being well characterized, the next step was to turn on a strong magnetic field generated by the 8.5 T magnet along the [1 1 1] direction of the crystal. The results of this are presented in the next section.

5.2   In-field a.c. susceptibility of $Dy_2Ti_2O_7$

With the zero field, low temperature a.c. susceptibility data of $Dy_2Ti_2O_7$ very well characterized, it was found that the SQUID setup produced results which qualitatively agreed with previously measured values. The main difference was the barrier to relaxation was measured to be 10.9 K instead of the previously reported 9.8 K [64] and 9 K [50]. The data presented in this section of the thesis will look different from the data of the previous zero-field regime in a few ways. First, the data became much noisier when the magnetic field was turned on. Many noise reduction techniques such as the vibration isolation from the bungee cords, installation of the μ-metal shielding, improving the temperature control of the sample stage, etc., had to be done before any data below even 1 Hz could be taken in-field. With the noise reduction techniques in place, the measurement bandwidth of the in-field data was between 10 mHz and 1 kHz for all the measured data sets, as any data below 10 mHz was spurious noise at every field value. In addition to this, the data below 100 mHz began exhibiting strange behavior as the field was increased, and this behavior became more and more apparent up to the 1 T measured, this will be discussed more below. In addition to all of this, not being able to reach 1 mHz significantly affects the ability to extract the d.c. susceptibility value from the a.c. susceptibility data (it can be extrapolated, but not as accurately). This would have been an interesting property to quantify due to the Kagome ice phase transition occuring as the field is increased. The strange low frequency behavior as the field was increased prevented this analysis. A background subtraction was performed for all of the in-field data, except for the 500 mT data due to the fridge blocking before it could be taken (same cooldown as the data of Figure 5.1). Regardless of the above barriers, the noise on the setup due to vibrations, temperature control, grounding, etc. was reduced to the point where the characteristic relaxation times could be reliably extracted from the in-field a.c. susceptibility data. These relaxation times were measured as a function of temperature and applied magnetic field along the [1 1 1] direction in the Arrhenius relaxation regime of the crystal. The in-field $Dy_2Ti_2O_7$ a.c. susceptibility data is presented below.
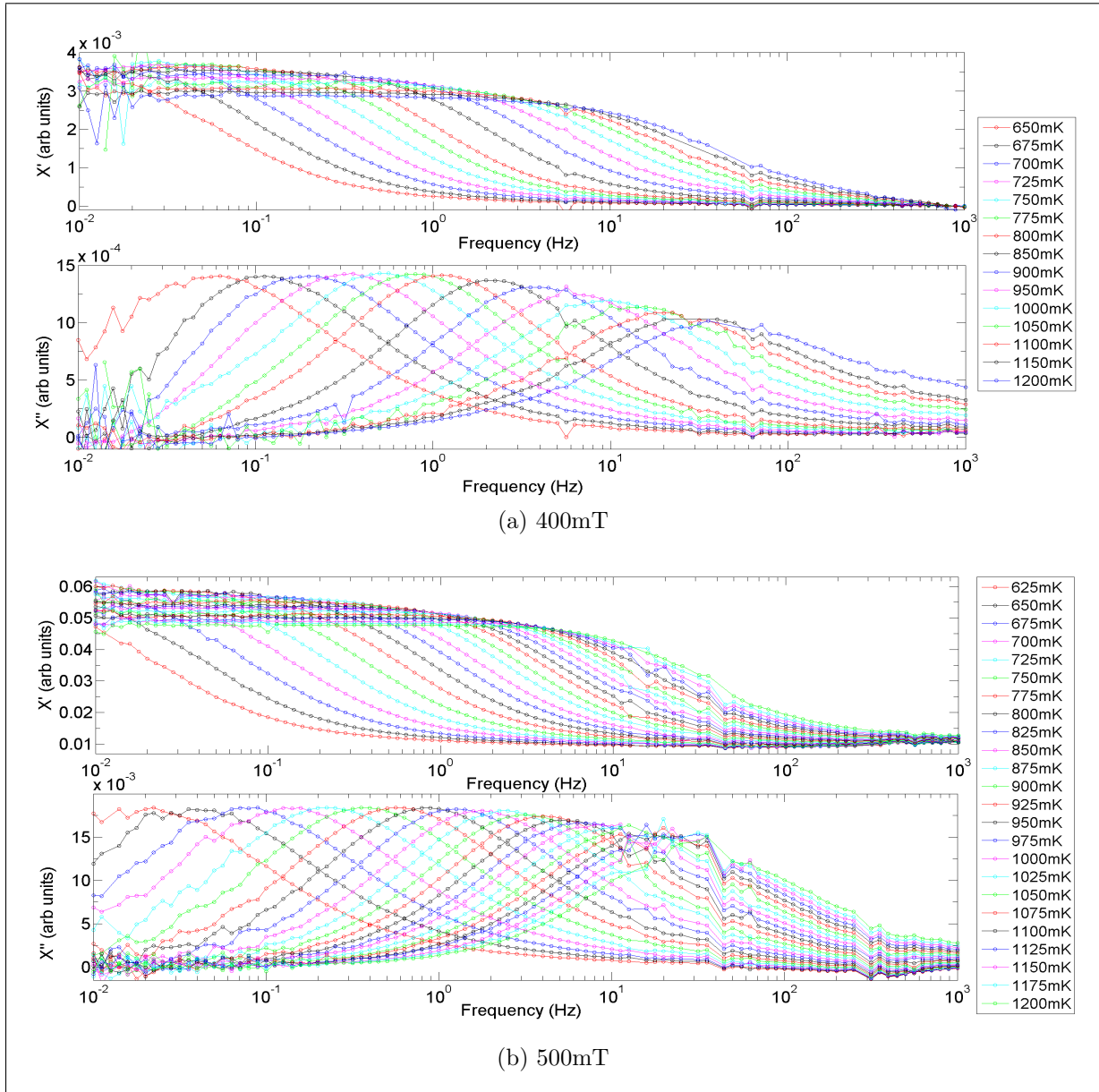
Figure 5.10: The a.c. susceptibility of $Dy_2Ti_2O_7$ measured along the $[1\,1\,\overline{2}]$ direction with an applied field of 400 mT along the $[1\,1\,1]$ direction in (a) and 500 mT along the $[1\,1\,1]$ direction in (b). The corresponding temperatures are shown in the legends, with the lower temperature scans corresponding to lower frequency peaks in χ''.

71
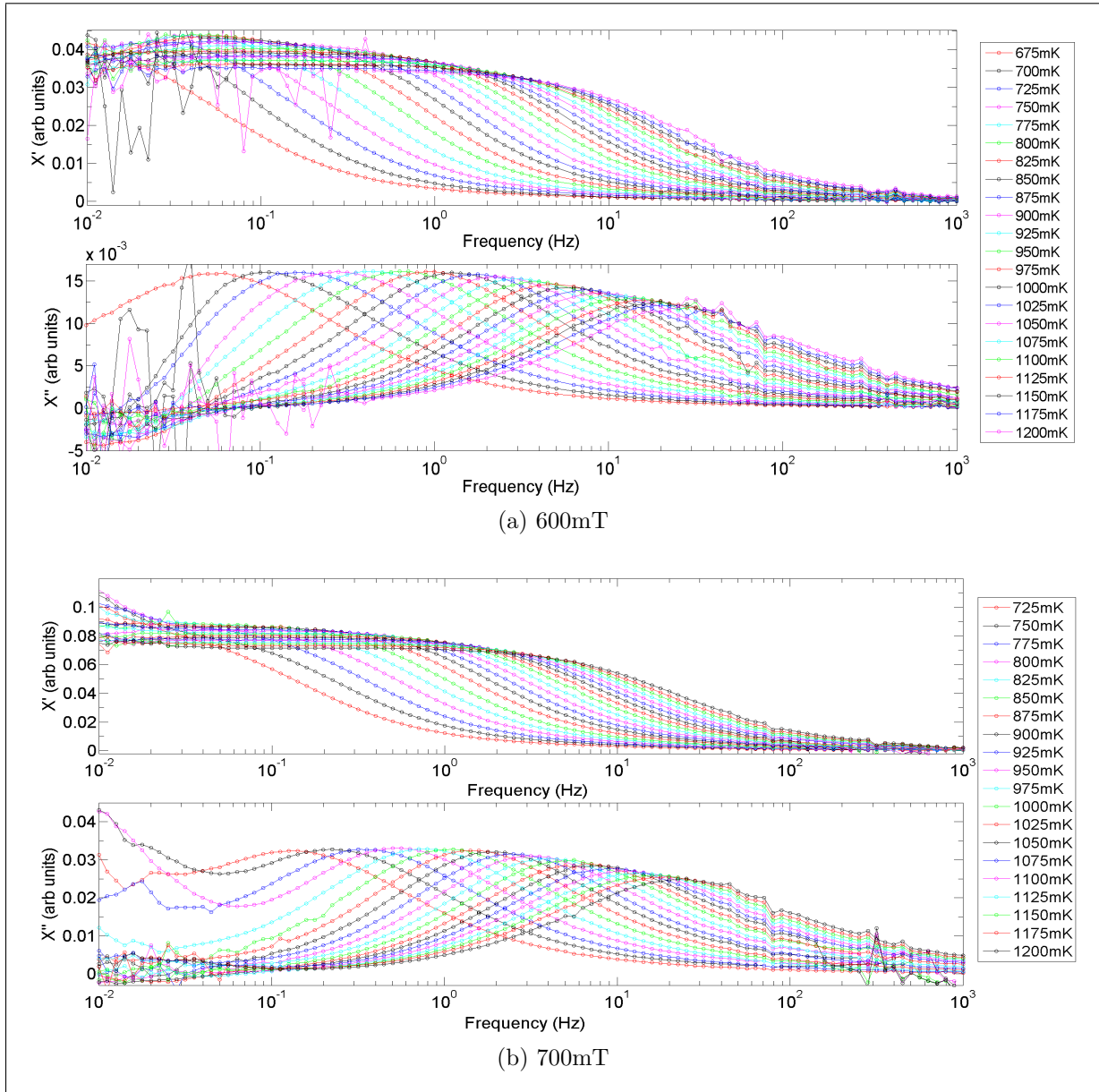
Figure 5.11: The a.c. susceptibility of $Dy_2Ti_2O_7$ measured along the $[11\bar{2}]$ direction with an applied field of 600 mT along the $[111]$ direction in (a) and 700 mT along the $[111]$ direction in (b). The corresponding temperatures are shown in the legends, with the lower temperature scans corresponding to lower frequency peaks in χ''.
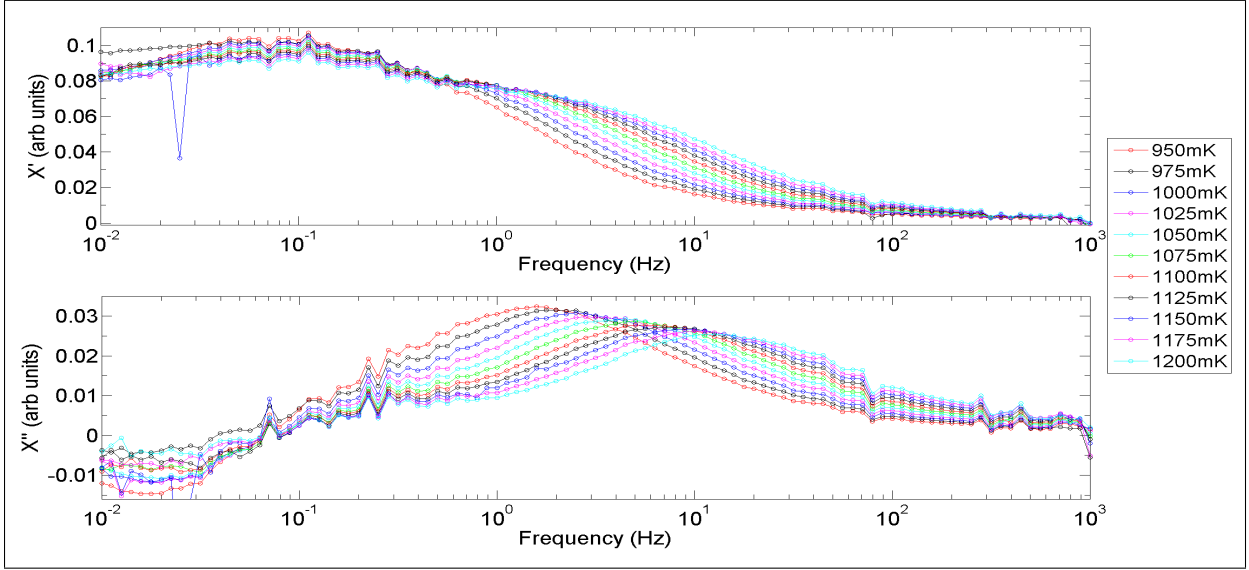
Figure 5.12: The a.c. susceptibility of $Dy_2Ti_2O_7$ measured along the $[1\,1\,\overline{2}]$ direction with an applied field of 1 T along the $[1\,1\,1]$ direction. The corresponding temperatures are shown in the legends, with the lower temperature scans corresponding to lower frequency peaks in χ''.

In Figure 5.10, Figure 5.11, and Figure 5.12, all of the in-field data taken is shown. There are a number of comments to make at this point. First, it is clear looking at the $\sim$600 mT - 1 T data that as the field was increased the data became drastically noisier. The shape of the χ'' curves were behaving strangely in the low frequency limit in the 700 mT and 1 T data. The normalized χ'' curves for the data between 400 mT and 700 mT are shown in Figure 5.14, giving full-width-half-max values between 1.5-1.8 decades for all the in-field data. This is in close agreement with the zero field full-width-half-max values of 1.4-1.7 decades for this crystal. The relaxation frequencies could still be accurately found from the in-field data, even with the large noise levels, by using the same method as in the zero-field data. This involved fitting the χ'' curves to Equation 5.2, and extracting the peak frequency from the fit. The resulting relaxation frequencies are shown in Figure 5.13, along with the zero-field data and the data of [64]. From this plot, it is clear that the $Dy_2Ti_2O_7$ magnetic relaxation times became slower at all measured temperatures between $\sim$600 mK - 1200 mK as the field was increased, including the temperatures considered outside of the Arrhenius region. In addition to this, Arrhenius relaxation is seen in the 400 mT, 500 mT, 600 mT and 700 mT data.

A number of interesting conclusions can be drawn from Figure 5.13. The barriers
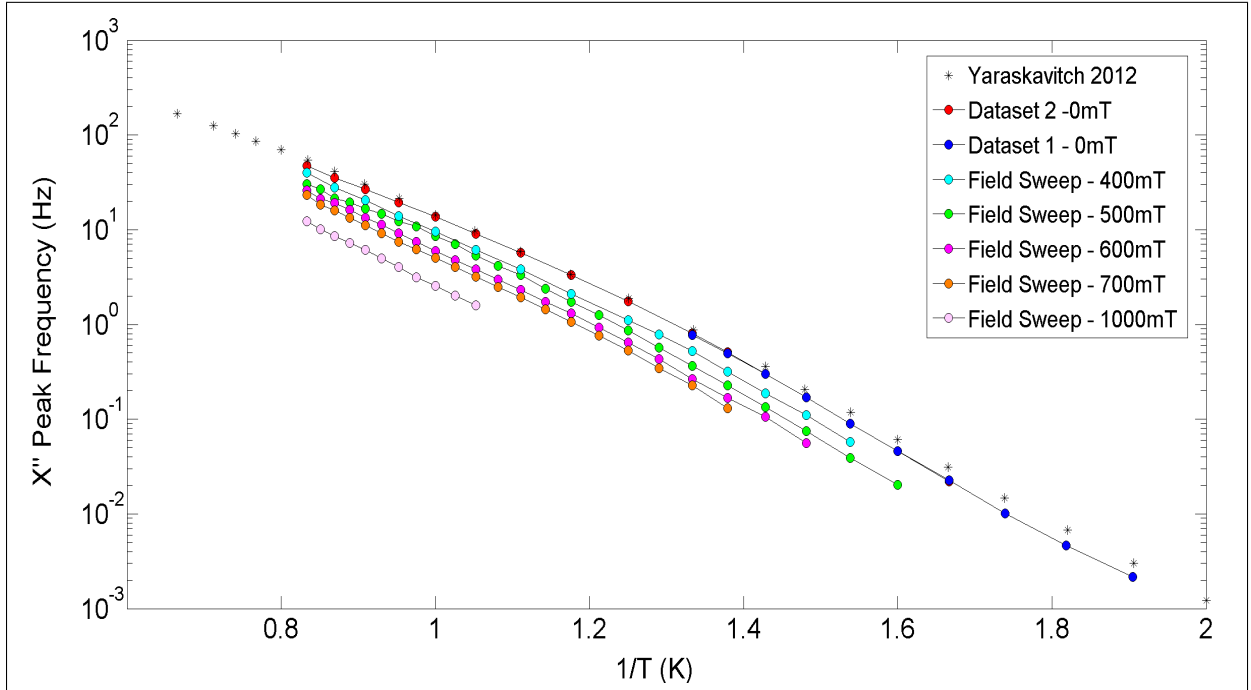
Figure 5.13: The characteristic relaxation rates of the same $Dy_2Ti_2O_7$ crystal measured in the zero field data of this thesis, measured in fields up to 1 T. The χ'' curves which were the most non-symmetrical were not included. The relaxation frequencies steadily dropped in value as the field along $[1\,1\,1]$ was increased, showing that the system becomes steadily slower as field is increased.

to relaxation along with the attempt frequencies and characteristic relaxation times are given in Table 5.1 for the zero field and in-field data. The uncertainties on these values were found by fitting maximally sloped lines and minimally sloped lines to the Arrhenius relaxation region, and taking the difference of those fits from the best fit to the Arrhenius region for each field value. Within the error bars, the barrier to relaxation for all four of the measured in-field values seems to be the same as the zero field value of 10.9 K. In addition to this, the attempt frequency steadily decreased in the Arrhenius region as the field was increased. This is best looked at on a plot of the attempt frequency (f_0) in the Arrhenius region versus field, or equivalently the characteristic relaxation time versus field, where they are related by $f_0 = \frac{1}{2\pi\tau_0}$. This is plotted in Figure 5.15. The increase in the characteristic relaxation time τ_0 could be attributed to a changing monopole density in accordance with the theory developed in [50], motivated from Debye-Hückel theory. In this article, the authors find that in order to get the experimentally observed shape to

74

Applied field along [1 1 1] (T)	Barrier to relaxation (K)	Attempt frequency (Hz)	Characteristic relaxation time (s)
0	10.9 ± 0.1	$1.8E + 06 \pm 1E + 04$	$8.8E - 8 \pm 4.9E - 10$
0.375	10.8 ± 0.3	$9.1E + 05 \pm 1.4E + 05$	$1.7E - 7 \pm 2.6E - 8$
0.475	10.8 ± 0.2	$6.6E + 05 \pm 4E + 04$	$2.4E - 7 \pm 1.4E - 8$
0.575	10.8 ± 0.3	$5.1E + 05 \pm 5E + 04$	$3.1E - 7 \pm 3.0E - 8$
0.675	10.9 ± 0.4	$4.3E + 05 \pm 6E + 04$	$3.7E - 7 \pm 5.1E - 8$

Table 5.1: Barriers to relaxation, attempt frequencies, and characteristic relaxation times for the in-field $Dy_2Ti_2O_7$ data of Figure 5.13, with demagnetization corrected applied fields along [1 1 1].
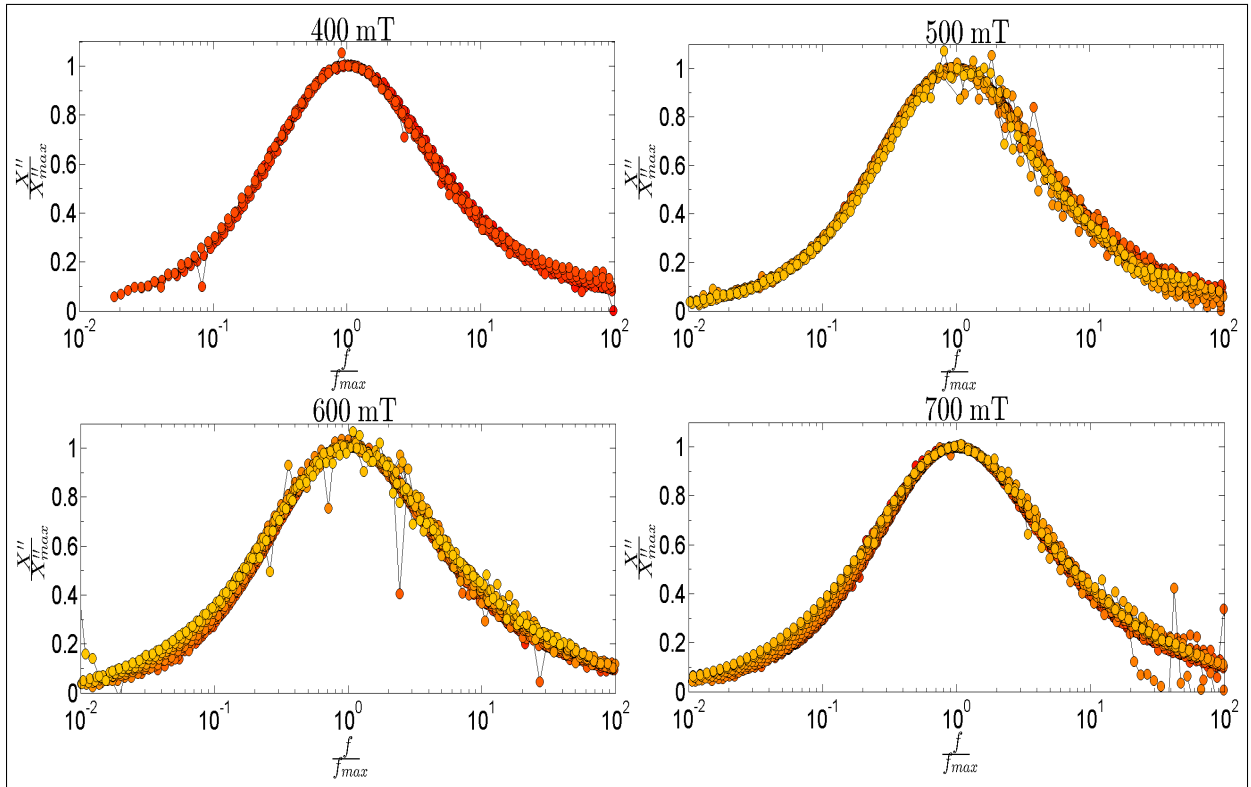
Figure 5.14: Normalized χ'' curves for the 400 mT - 700 mT Data, with red being lower temperature and yellow being higher temperature. The temperatures are: 400 mT - 650 mK to 950 mK, 500 mT - 725 mK to 1125 mK, 600 mT - 675 mK to 1200 mK, 700 mT - 725 mK to 1200 mK. The full-width-half-max values were between 1.5 and 1.8 decades for all the in-field data, with no clear correlation as a function of field.

the correlation functions (i.e. qualitatively the same as the ones as obtained in this thesis

from Figure 5.8) from a simulation of interacting monopoles, they had to make a number of assumptions. One was open-loop boundary conditions during the simulation, which could be a sign of surface effects becoming important in the Arrhenius relaxation regime. The second was the introduction of stuffed sites to the lattice. The third assumption was that not only was the relaxation Arrhenius, i.e. $\tau = \tau_0 e^{\frac{4J_{eff}}{k_B T}}$, but that τ_0 was proportional to one over the monopole density in the system; i.e. $\tau_0 \propto \frac{1}{p}$. In addition to this, they attributed $\frac{1}{p}$ as being proportional in an Arrhenius fashion to the monopole pair creation energy; i.e. $\tau_0 \propto \frac{1}{p} \propto e^{\frac{4J_{eff}}{k_B T}}$. This gave the correct shape to the correlation functions, with the correct barrier to relaxation of around ~ 9 K. These assumptions resulted in a successful theory to explain the low temperature Arrhenius regime as being an impurity effect, owed to stuffed sites. In the context of the present work, due to the correlation functions being qualitatively similar to the ones in [50], this could mean that the sample measured in this thesis follows a similar theory. If there was another way to tune the monopole density, then under the assumption that $\tau \propto p^{-2}$, one could see a change in the characteristic relaxation time as the monopole density was changed. This could be an explanation as to what is observed in Figure 5.15. Under this theory, the data suggests that the density of monopoles is decreasing as field along [1 1 1] is increasing. Since the system is not in the saturated state, where the monopole density becomes high due to the 3-in 1-out and 1-in 3-out defects occupying the whole lattice, the ice rules are still obeyed. In addition to this, the monopoles are confined to 2-D sheets in the Kagome ice state [25]. In [25], it has been theorized that there is an increase in the energy to create a monopole pair as the applied field along [1 1 1] is increased, owed to the Zeeman energy given to the Kagome plane spins from the applied magnetic field. This is owed to the fact that each spin in the 2-D Kagome layers still have a component of spin along the applied field direction when in the Kagome ice state. In this paper, the authors claim that the monopole creation cost could vary by as much as 2 K at 700 mT [25]. One can imagine a picture where a combination of these two effects should result in a decrease in the monopole density, due to an increase in the monopole creation energy but the same finite amount of thermal energy, which according to the above theory would mean an increase in the characteristic relaxation time. This could explain the behavior observed in Figure 5.15. In addition to this observation, the characteristic relaxation time seems to be following an exponential form with the applied field along [1 1 1] of the form $\tau_0 = \tau_{(B=0)} e^{\frac{B}{B_0}}$, with B_0 found to be 0.47 T. This is a very interesting number because it is very close to the field value corresponding to when the applied field gives an energy of J_{eff} to the field opposed spin in the Kagome ice state; i.e. the field value where the first magnetization plateau appears in the Kagome ice state. It is very interesting that the characteristic relaxation time fits an exponential law as a

function of field along [1 1 1]. There is no currently developed theory expecting this, and the fact that it has this characteristic field value B_0 is interesting. If this was a true law, then it could hold in $Dy_2Ti_2O_7$'s sister compound $Ho_2Ti_2O_7$, but with the critical Kagome ice field corresponding to that in $Ho_2Ti_2O_7$. The fact that the barrier to relaxation of the in-field data is the same as the zero field data, but τ is exponentially increasing with field, suggests that the equation for τ from [50] can be modified to $\tau = \tau_{0'}e^{\frac{8J_{eff}}{k_BT}+\frac{B}{B_0}}$, where now $\tau_{0'}$ is independent of temperature and field. This equation would qualitatively explain the observed in-field data, however, the zero field barrier was 10.9 K for this sample, instead of $\sim 9K$, similar to disagreement with the data of [64], who found a barrier of $\sim 9.8K$. If the barrier to relaxation was indeed proportional to the monopole pair creation cost, as was theorized in [23], then it should have changed by an appreciable amount as the field was increased. The monopole creation cost was measured in the heat capacity measurement of [25] as a function of field, and was found to change by almost 2 K at 700 mT; however, it was experimentally found that the barrier did not change to within 0.3 K. This suggests that the barrier to relaxation in the low temperature Arrhenius regime might not be correlated to the monopole pair creation cost to the degree that has been theorized thus far. In addition to this, a possible explanation for the changing monopole creation cost measured through heat capacity in [25] is that since the magnetic relaxation time is steadily increasing as field is increasing, there could be thermal equilibration issues with the heat capacity data of $Dy_2Ti_2O_7$ at low temperatures. In [46], it was found that the thermal relaxation time of $Dy_2Ti_2O_7$ in specific heat measurements was directly correlated with the magnetic relaxation time found through a.c. susceptibility measurements. If this is true, then according to the data of Figure 5.13, the thermal time constant of $Dy_2Ti_2O_7$ becomes exponentially longer both as temperature is lowered, and field is increased. Since the majority of the data presented in [25] is below 500 mK, and at high field values, where the thermal time constant is then predicted to be on the order of 10^4 s and longer, the heat capacity data taken using the quasi-adiabatic heat pulse method could have thermal equilibration issues. Thermal equilibration issues were found in other works using this method to measure the specific heat of $Dy_2Ti_2O_7$ [46].

The dynamical correlation functions were also calculated for the in-field data, with the 600 mT correlation functions plotted in Figure 5.16. The correlation functions of the other field values showed the same behavior, and so are not shown. The correlation functions could not be calculated accurately in the Arrhenius temperature regime for any field value. This is because at least a full-width-half-max worth of clean data about the χ'' peak was needed to get consistent values of the correlation function, and the data in the Arrhenius region had less than this due to being so close to the lower frequency bandwidth edge of 10 mHz. The temperature regime shown however is consistent with the Kagome ice state
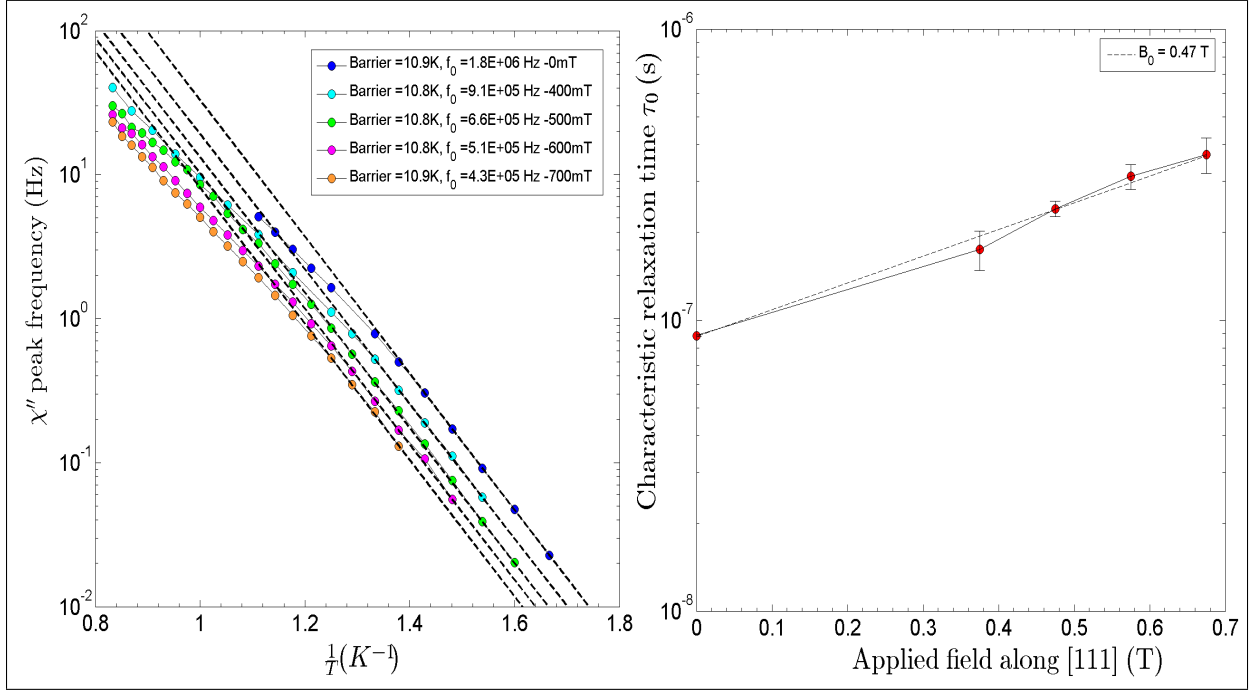
Figure 5.15: Left Figure: The Arrhenius relaxation fits to the in-field relaxation times of Figure 5.13. Right Figure: The corresponding characteristic relaxation times from the fits of the left figure, plotted versus demag corrected applied field along [111]. An exponential fit is found with a characteristic field of 0.47 T.

from the phase diagram in Figure 3.10. The same stretched exponential behavior leading into a long-time algebraic tail was seen for all the in-field data as was seen for the zero field data. The stretch factors were also very similar, between 0.68-0.70, close to the 0.73-0.77 found in the zero field data. This observation, along with the fact that the full-width-half-max of the χ'' peaks was found to be between 1.5 and 1.8 decades for the in-field data, very close to the zero field full-width-half-max of 1.4-1.7 decades for this sample, shows that the χ'' shape in the Kagome ice state is very similar to the χ'' shape in the regular spin ice state. The primary difference is thus the slowing down of the magnetic relaxation times when moving into the Kagome ice state. The d.c. susceptibilities could also show a sign of moving into the Kagome ice state, however as mentioned previously, they were not extracted from the in-field data due to the noise levels at low frequencies.

As mentioned in section 3.3, a scaling theory was developed in [41] for a.c. susceptibility data in the Kagome ice state, given by Equation 3.6. The form given in Equation 3.6 was fit to the 400 mT, 600 mT, and 700 mT data and is shown in Figure 5.17, with the red
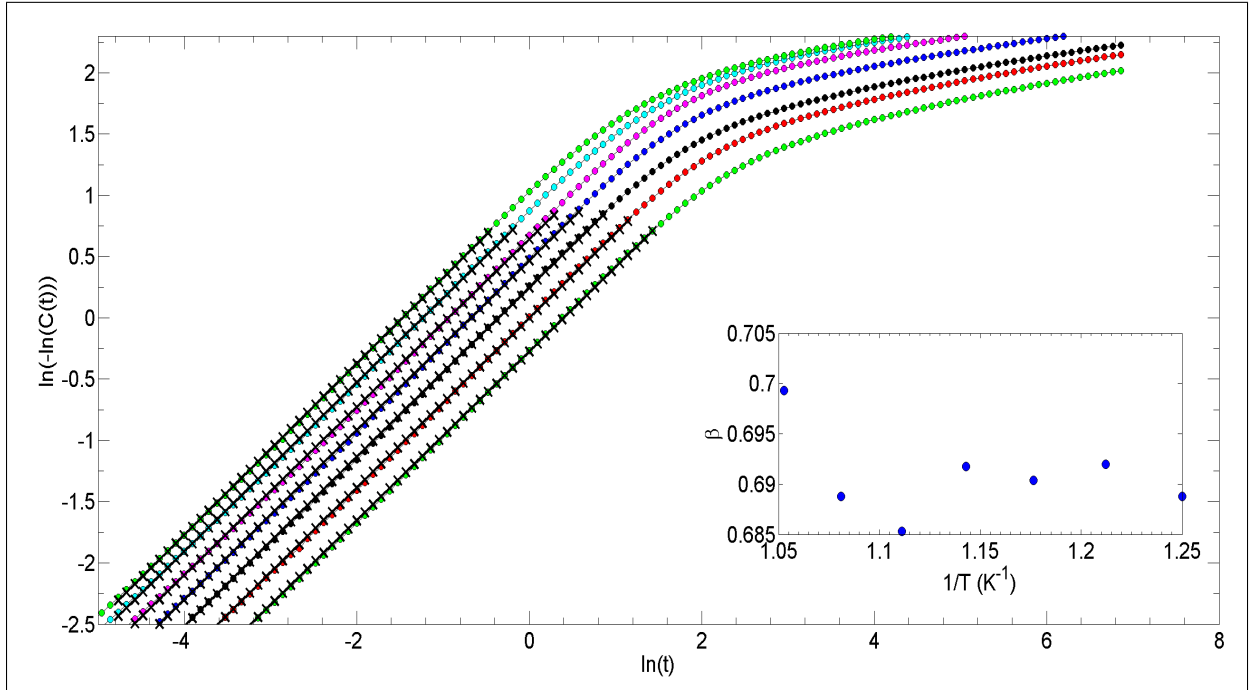
Figure 5.16: Correlation functions for the 600 mT data of Figure 5.11, going from 800 mK on the left to 950 mK on the right.

lines representing the fits. In addition to these three field values, the zero field data was also fit. As one can see, the scaling law was found to disagree with the measured data in the Kagome ice state. This is best seen by comparing the fits to the in-field data and the fit to the zero field data. No clear difference to the goodness of the fit was seen as the sample was moved towards the Kagome ice state. This does not mean the theory of [41] is incorrect however, two important factors are at play in the scaling plot. First, calculating the d.c. susceptibility values to do the scaling becomes more and more difficult as the field is increased due to the slowing down of the magnetic relaxation time. The values were read off of the Cole-Cole plots for the in-field data, but still there are inaccuracies on the order of $5 - 10\%$ for the lowest temperature, highest field data. An incorrect d.c. susceptibility would simply scale the whole curve by a constant however, it would not affect the shape, which for the in-field data disagrees with the expected shape from Equation 3.6 by a significant amount both on the high frequency and low frequency sides. More specifically, the experimental full-width-half-max of the in-field data is much larger than the theoretical expectation of approximately 1.4 decades. In the case of a small demag factor (N=0.042 for this sample) one can find for reasonable SQUID output voltage

to susceptibility calibration values (i.e. ones that will make the d.c. susceptibility values of Figure 5.7 agree with those from [64]), a demag correction alone is insufficient to explain the discrepancy. None of these reasonable calibration values, when used in Equation 4.2, will shift the full-width-half-max of the in-field χ'' data to the ~ 1.4 decades necessary for the scaling law to work. This is because the demagnetization correction is a more or less linear shift to the χ'' peaks for small N values. This scaling law should hold at frequencies less than the characteristic frequency w_1 of the scaling law, as mentioned in [41], defined as $w_1 = \frac{D}{\xi^2}$, where D is the diffusion constant of the monopoles and ξ is their correlation length. From the fits made to the in-field data, these values w_1 were on the order of 50 Hz - 1 KHz depending on the temperature and field value. If the scaling law form is fit to just the low frequency portion of the χ'' data, at frequencies less than w_1, they are improved, however there is no more improvement to those fits than there is to doing the same thing to the zero field data where the scaling law is not expected to hold. This is due to the Coulomb interactions being 3-D instead of 2-D when in zero field. Thus, the Kagome ice data obtained in this thesis does not agree with the predicted scaling law form from [41].
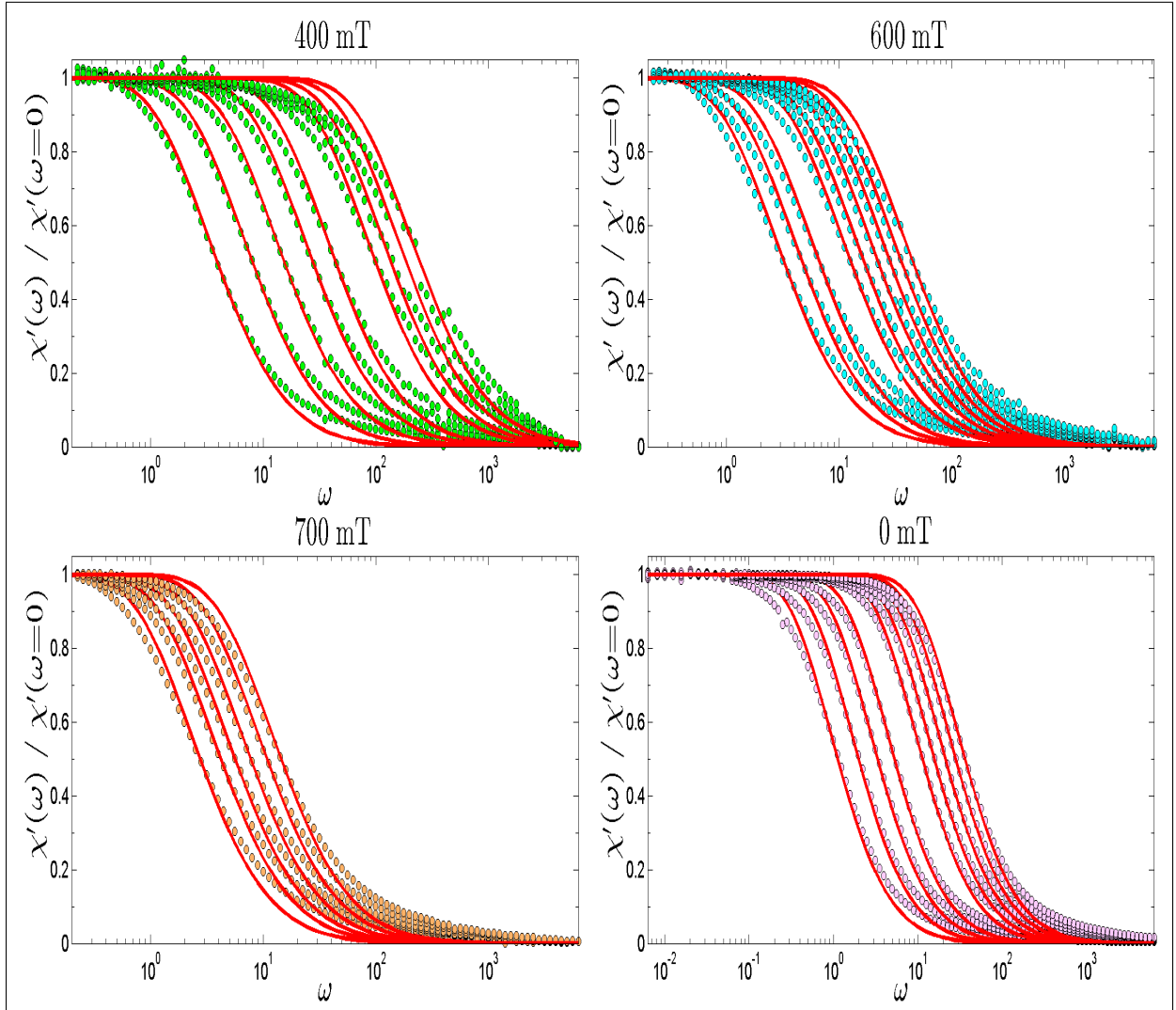
Figure 5.17: Plot of the scaling law given by $\frac{\chi'(w)}{\chi'(w=0)}$ for the 400 mT, 500 mT, and 700 mT in-field data. The fits to the form given in Equation 3.6 are shown with red lines. The temperatures are: 400 mT - 750 mK to 1.2 K, 600 mT - 775 mK to 1.1 K, 700 mT - 775 mK to 900 mK. The zero field data was also fit to Equation 3.6 as a comparison between 675 mK and 900 mK. The fits to the in-field data are no better than the fits to the zero field data, where the scaling law should not hold, thus, the scaling law disagrees with the in-field data.

Chapter 6

Conclusions and future work

- **A dilution refrigerator setup was modified for in-field a.c. susceptibility measurements.**
  With the addition of a 8.5 T superconducting magnet to a dilution refrigerator setup, almost all of the components had to be redesigned and installed to allow for the in-field measurements. This included the design of a new vacuum can and radiation shield with bevels allowing the dilution unit to fit into the compensated region and high field region of the magnet. All of the copper stages and legs running from the mixing chamber down to the high field region were machined and installed. The addition of magnetic shielding in the form of a μ-metal shield, and vibrational isolation in the form of bungee cords was used to improve the a.c. susceptibility data. The gas handling system for the dilution unit was modified with additional safety features and a manifold for cleaning the mix external to running it through the dilution unit, and a vapor booster diffusion pump was set up with an 8 inch pneumatic gate valve on the still side of the fridge in order to improve the circulation rate of the dilution unit. All of the NbTi wiring and coaxiable cable for thermometry and for running the SQUID susceptometers were installed with importance given to heat sinking. The dilution fridge setup, now capable of taking in-field heat capacity and a.c. susceptibility data, reached a base temperature of below 10 mK, achieving the main goal of this thesis.

- **The a.c. susceptibility of $Dy_2Ti_2O_7$ was measured in zero field to characterize the new setup.**
  The zero field a.c. susceptibility of $Dy_2Ti_2O_7$ was measured between 525 mK and 1.2 K, within a bandwidth of 1 mHz to 1 kHz, and was found to agree qualitatively

with previously measured results. This included the shapes of the χ'' curves agreeing with previous results as measured through a full-width-half-max of 1.4-1.7 decades in the Arrhenius relaxation regime, showing the narrow distribution of relaxations in $Dy_2Ti_2O_7$, as also seen through semicircular Cole-Cole plots. Also, the magnetic relaxation times were found to agree with previously measured values, with the main difference being that this new sample had a zero field barrier to relaxation of 10.9 K $\pm$ 0.3 K, compared to the previously measured 9.8 K [64] and 9 K [50]. The correlation functions were calculated for the zero field data and they showed the stretched exponential behavior and long-time algebraic tail reported previously in $Dy_2Ti_2O_7$, with similar stretch factors. These results verified the accuracy of the a.c. susceptibility measurement on the new dilution refrigerator setup, and characterized this sample very well for comparison to in-field a.c. susceptibility data. These results also suggested that the theoretical model proposed in [50] of dipolar spin ice interactions on the pyrochlore lattice with monopoles interacting with a small level of impurities known as stuffed sites was consistent with the experimental data on this sample as well. Once again, the main quantitative difference is the barrier to relaxation in the low temperature Arrhenius region of the sample was found to be 10.9 K.

- **The a.c. susceptibility of $Dy_2Ti_2O_7$ was measured in-field**
  The in-field a.c. susceptibility of $Dy_2Ti_2O_7$ was measured between 625 mK and 1.2 K, with field values between 0.4 T and 1 T along [1 1 1], and a bandwidth of 10 mHz to 1 kHz. The measurement of frustrated magnetic materials at such low temperatures, with such high fields, using a d.c. SQUID with such a large bandwidth, is a first in the world. While this data was significantly noisier, the shapes of the χ'' peaks in the imaginary portion of the susceptibility could still be accurately fit to a model following Equation 5.2, and thus allowed the extraction of the magnetic relaxation times, the full-width-half-max of the curves, and allowed the correlation functions to be calculated. It was found that the in-field χ'' curves were very similar to the zero-field curves at all the field values measured, namely, they had a full-width-half-max between 1.5-1.8 decades, and the correlation functions had a stretched exponential behavior leading into a long-time tail with stretch factors of 0.6-0.8, close to the zero field values of 1.4-1.7 decades and 0.7-0.8 respectively. The main difference was thus seen in the magnetic relaxation frequencies, which steadily decreased as the field along [1 1 1] was increased for all temperatures and field values measured. Arrhenius relaxation was seen at 400 mT, 500 mT, 600 mT, and 700 mT with barriers to relaxation equal to the zero-field barrier to relaxation to within the experimental certainty of $\sim$ 0.3 K. The characteristic relaxation times, τ_0, were found to steadily increase as the field along [1 1 1] was increased, and followed an exponential form,

with a characteristic field $B_0 = 0.47$ T. A scaling law for the a.c. susceptibility data proposed in [41] was fit to the in-field a.c. susceptibility data and was found to be a poor fit at all field values measured. In addition to this, the fits were found to agree with the in-field data just as well as the zero field data, where the scaling form is not expected to be true, thus, the proposed scaling law disagreed with the in-field data.

There are a number of improvements that could be made to the new fridge setup in the future to improve on the results presented here. The main improvement would be to increase the in-field bandwidth to go down to 1 mHz by getting rid of the in-field noise sources. This would allow for a demagnetization correction to the in-field data, and also allow data taking down to lower temperatures, allowing the Arrhenius region to be explored in more depth, and allowing the scaling law of Equation 3.6 to be explored with more accuracy. This could be achieved with the fridge improvements listed in section 4.1 of this thesis, with the idea that the most likely cause of the low frequency noise is a combination of temperature control for the data below 1 mHz, and relative motion between the SQUID susceptometer and the large background field for the higher frequency noise.

The main implications of this work are the following. First, the new dilution refrigerator setup was extremely successful in achieving the goal of measuring in-field a.c. susceptibility of $Dy_2Ti_2O_7$, meaning such a design could be implemented at other universities to do in-field SQUID magnetometry of other interesting materials at mK temperatures. Next, when the field was turned on in the [1 1 1] direction of $Dy_2Ti_2O_7$, and the a.c. susceptibility was measured in the predicted Kagome ice state, current models, which predict a barrier to relaxation in the low temperature Arrhenius region which is proportional to the creation cost of a monopole pair, seem to be in disagreement with these results. The monopole creation cost should have varied linearly with applied field and changed the barrier to relaxation by an amount much larger than the experimental uncertainty in the barrier to relaxation of ~ 0.3 K if this was true, following from arguments in [25]. A change of less than $\sim 0.3K$ in the barrier to relaxation was observed between the 700 mT data and the zero field data. The attempt frequency in the Arrhenius relaxation regime was found to drop steadily for all field values measured between 0.4 T and 0.7 T. The increase in the corresponding characteristic relaxation time seems to follow the rather simple form $\tau_0 = \tau_{(B=0)}e^{\frac{B}{B_0}}$, with B_0 found to be 0.47 T, a result not predicted by current theoretical models. According to Debye-Hückel theory, if the characteristic relaxation time is proportional to the inverse monopole density, then this result could mean that the density of monopoles is decreasing as the field along [1 1 1] was increased. This is different from currently discussed literature which predicts that the density of monopoles decreases for decreasing temperature, it has not been discussed in depth how it changes as a function of field, until one gets

84

into the monopole crystal state around 0.9 T where the monopole density increases with applied field [25]. Lastly, the scaling law predicted for a 2-D Coulomb gas was found to disagree with the in-field data, either suggesting the 2-D Coulomb gas of monopoles is not a good description of the a.c. susceptibility in the Kagome ice state, or suggesting that the theoretical model needs to be extended to include other effects.

APPENDICES

Appendix A

Heat capacity of UPt$_3$

A.1 UPt$_3$ theory

UPt$_3$ is an f-wave heavy fermion superconductor, whose superconducting properties have been studied for over 20 years. One of the first identifications of unconventional superconductivity in UPt$_3$ was non s-wave pairing (i.e. the superconducting transition didn't have the form $C \sim e^{-\frac{\Delta}{k_B T}}$), found through a double peaked superconducting transition in heat capacity around 500 mK. As with all superconductors, the properties of the superconducting phase transition is determined by the order parameter of the phase transition, called the superconducting gap. The gap is usually denoted by $\Delta(k)$, where the dependence on k denotes it is a function of direction in momentum space. The cooper pairing which happens in a superconducting transition, which is responsible for all the novel properties of superconductors, can form either S=0 (singlet) or S=1 (triplet) states owing to the two spin 1/2 electrons. In addition to a spin, the cooper pairs also have an angular momentum, which must be even (L=0, 2, etc.) for the singlet state or odd (L=1, 3, etc.) for the triplet state to preserve wavefunction symmetry. Singlet states with L=0 are called s-wave superconductors (superconductors following BCS theory) and singlet states with L=2 are called d-wave superconductors (many high T_c cuprates). The triplet states with L=1 are called p-wave superconductors (Sr$_2$RuO$_4$) and the triplet states with with L=3 are called f-wave superconductors. The nature of which type of superconductor the material is (s, d, p or f) has to do with the symmetries of the system. The symmetries determine the functional form for the order parameter, which then has experimentally measurable consequences. For example, symmetry could make the order parameter have nodes in it, regions where the order parameter is equal to precisely 0 along different momentum directions. In

the case of UPt_3, the major sign of non-conventional superconductivity can be seen as a tetracritical point in the H-T phase diagram of UPt_3, which separates 3 superconducting phases called the A,B, and C phase as seen below in Figure A.1. The points represent the two different peaks observed in the heat capacity near the superconducting transition.
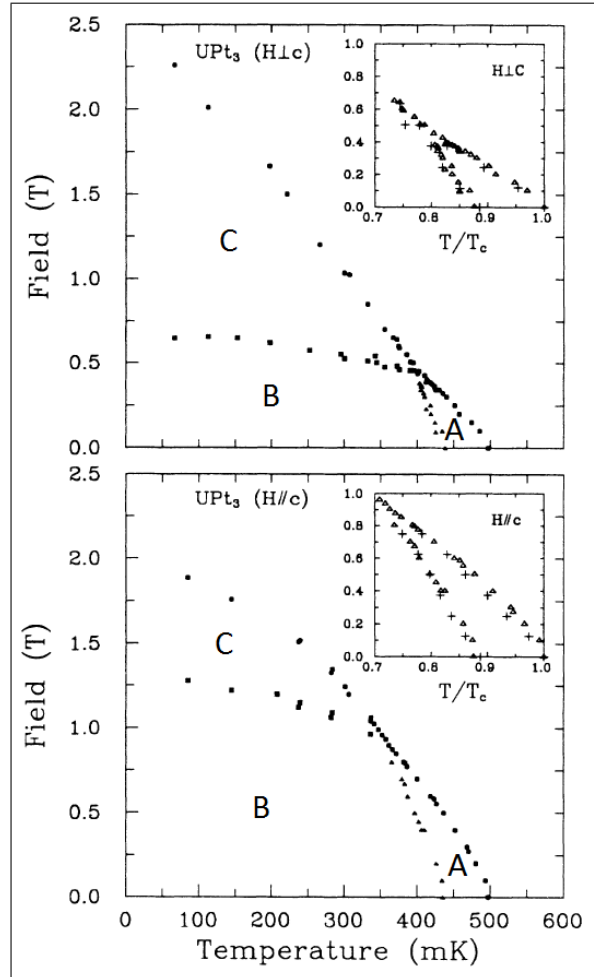
Figure A.1: The H-T phase diagram of UPt_3 from [1], with the A,B and C labels added in to show the 3 different superconducting phases.

Many different models have been made to explain the unconventional superconductivity in UPt_3 in the last 20 years. Unfortunately, no single theoretical model has been able to explain all observed data, most likely owing to the complex interplay of magnetism and superconductivity present in UPt_3. The role of magnetism in this superconductor comes

into play as UPt$_3$ orders into an anti-ferromagnetic state at low temperature with a Néel temperature of 5-6 K, and a magnetic moment along the basal plane of approximately 0.02 μ_B per U atom [24]. It is not obvious that this would have an effect on the superconducting transition, until the pressure v.s. temperature phase diagram was measured in [61] and is shown in Figure A.2. The fact that the double peak superconducting transition was suppressed at a critical pressure near 3 kbar, and at that same critical pressure, it was found that the weak anti-ferromagnetic order in UPt$_3$ below 5-6 K was suppressed [60], suggested that the double peak superconducting transition was coupled in a significant way to the anti-ferromagnetic order. This observation was strong evidence that the anti-ferromagnetic order is responsible for the complex behavior of the gap. Following the experimental observations of Figure A.1 and Figure A.2, and due in large part to thermal conductivity measurements [33] and ultrasound measurements mentioned in more detail in [20], only a certain class of theoretical models are able to explain the observed H-T and P-T diagrams, as well as the nodal behavior measured experimentally in the gap. This class of models of UPt$_3$ superconductivity are the 2 dimensional representations of the order parameter.

There are four 2 dimensional representations used to describe UPt$_3$, which belong to the normal state hexagonal point symmetry group D_6h, these are the irreducible representations E_{1g}, E_{1u}, E_{2g}, and E_{2u}. These representations simply limit the allowed functional form of the gap based on symmetry considerations. The 2 dimensional representations for the order parameter have a few things in common. Namely, the order parameter is a 2-component complex vector of the form $\overline{\eta} = (\eta_1, \eta_2)$, and the splitting of the superconducting critical temperatures of the A and B phases is due to a coupling between the order parameter and a symmetry breaking field (SBF). In this notation, the A phase is represented by components (1,0), the C phase by (0,1), and the B phase by (1,±i), where the difference in the phases is due to symmetries. It can be shown in [24] for example, that taking this two component order parameter and coupling it to a magnetization vector M, in a general free energy functional that preserves the symmetry of the problem, there is a symmetry breaking between the x and y (if the magnetization is directed along x for example) directions. This symmetry breaking results in two different minima in the free energy functional. This gives way to two superconducting transitions. This is a good motivation for the two component order parameter model, as the double peak transition is observed experimentally. All four of the 2-dimensional representations have this double transition behavior in the presence of a SBF, so to narrow down the possible representations even further, the nodal behavior of the gap can be analyzed. From thermal conductivity measurements, experimental evidence suggests the possible representations are brought down to only two, E_{1g} and a special case of E_{2u}, due to the nodal behavior being similar for these
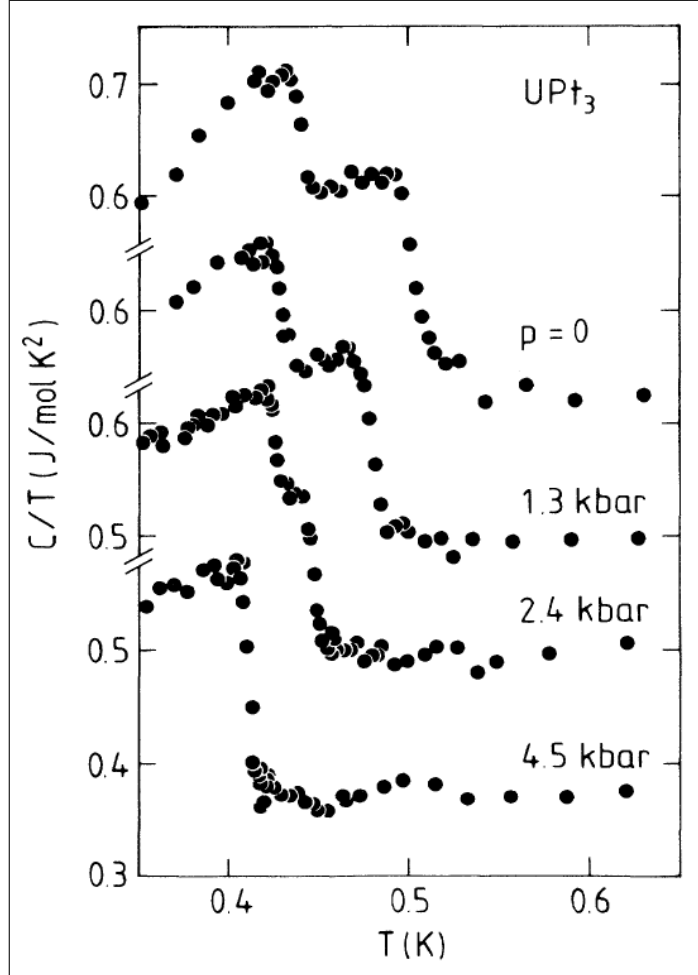
Figure A.2: The P-T Phase Diagram of UPt$_3$ from [61], showing the suppression of the double peak superconducting transition, with a critical pressure of ~ 3.7 kbar.

two representations. The nodal behavior is shown in Figure A.3. One interesting behavior of a gap with nodes is that the specific heat after the lower heat capacity transition varies as T^3 for point nodes and T^2 for line nodes for a superconductor with linear dispersion of the gap at the nodes. For hybrid type nodes such as the ones for E_{1g} and E_{2u} which have both line and point nodes, the T^3 term will dominate until temperature gets low enough, then the T^2 takes over.

Most of the work described above has been done many years ago, and as mentioned, is described well in [24]. More recent studies such as [59], [58], and [55] all point to the
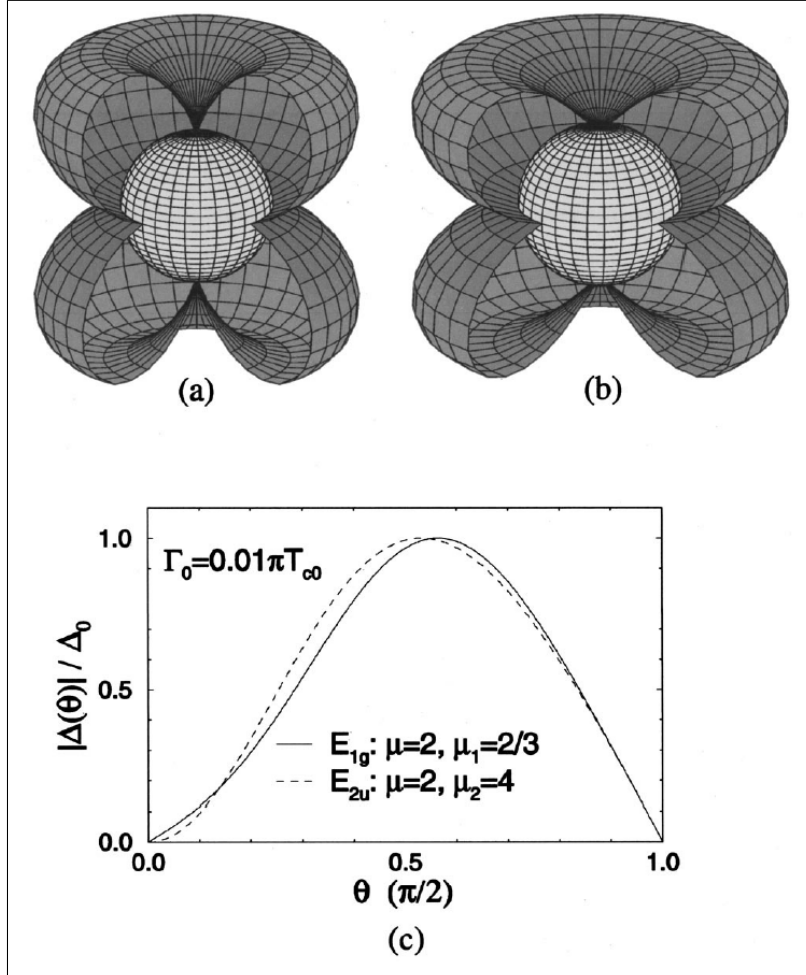
Figure A.3: The nodal behavior for (a) E_{1g} and (b) E_{2u} representations. The difference between the two types can be seen as the variation in the gap as a function of angle from the top nodes in (c). Both gaps vary linearly near the line node at the equator, and linear for E_{1g} and quadratic for E_{2u} near the point nodes at the poles. From [24].

E_{2u} representation being the correct one for UPt$_3$, and yet there are still other recent studies such as [34] which point to it not being E_{2u}. Clearly, even after over 20 years of work on this material, there are still many open questions remaining, most of which could likely be answered by discovering the nature of the SBF. Another question, is the double peak transition an extrinsic or intrinsic effect, or in other words, is the tetracritical point due to an effect such as impurities which cause the symmetry breaking field. This is the

91

motivation for the measurement of an ultra high purity UPt$_3$ crystal, along with the goal of characterizing the new dilution refrigerator setup through low temperature specific heat measurements.

A.2 UPt$_3$ experimental details and results

The specific heat of a ultra high purity single crystal of UPt$_3$ was measured below 1 K on the new dilution refrigerator setup using the quasi-adiabatic heat pulse method. This sample has a mass of 16.9 mg, it was annealed at 970°C, and it has a RRR of ~ 720. The growth process for this crystal is well described in [29] under the name ZR4. The UPt$_3$ crystal was set up in a heat capacity cell described well in [47], shown in Figure A.4. A Dale electronics RuO$_2$ resistance thermometer with a resistance of 1 kΩ at room temperature was glued onto the UPt$_3$ crystal with General Electric varnish 7301, as well as a metal oxide film resistive heater with a resistance of 10 kΩ. The sample was suspended from Nylon threads, and connected to the fridge using a Pt-W weak link with an experimentally measured thermal conductivity of $6.1e^{-9}\frac{J}{Ks}$ at 500 mK. The heat capacity of UPt$_3$ was measured experimentally to be 12.6 $\frac{\mu J}{K}$ at 500 mK, which gave a weak link thermal time constant ($\frac{C}{K}$) of around 35 minutes at 500 mK. The leads for the thermometer resistance measurement and for the heater were all 6 μm diameter NbTi wires. As mentioned, the specific heat was measured using the quasi-adiabatic heat pulse method where by a very precise amount of heat ΔQ is sent across the heater connected to the sample, and the resulting change in temperature ΔT is measured precisely using the thermometer on the sample. The resulting equation for the heat capacity (C_n) for a number of moles n (2.0528e-5 moles for this sample) is the simple form given in Equation A.1. The heat capacity of the addenda for such a setup is estimated to be less than 1%, and the heat flow out of the sample from the NbTi wiring and nylon leads is negligible, both following from measurements made in [47].

$$C_n = \frac{\Delta Q}{n\Delta T} \tag{A.1}$$

The heat pulses were applied using the arbitrary waveform generator toolbox in Labview, and was applied to the samples heater with a National Instruments BNC 2090-A box, with a current limiting resistor of 5 MΩ. The heat pulse heights varied between data sets, but had an value on average of around 2-7 V excitation for 1 second across the 5 MΩ current limiting resistor. This resulted in heat pulses of $\sim 1-20$ nJ and temperature jumps of $\sim 1-5$ mK for this UPt$_3$ crystal. The heat pulse was applied, and the resulting

92
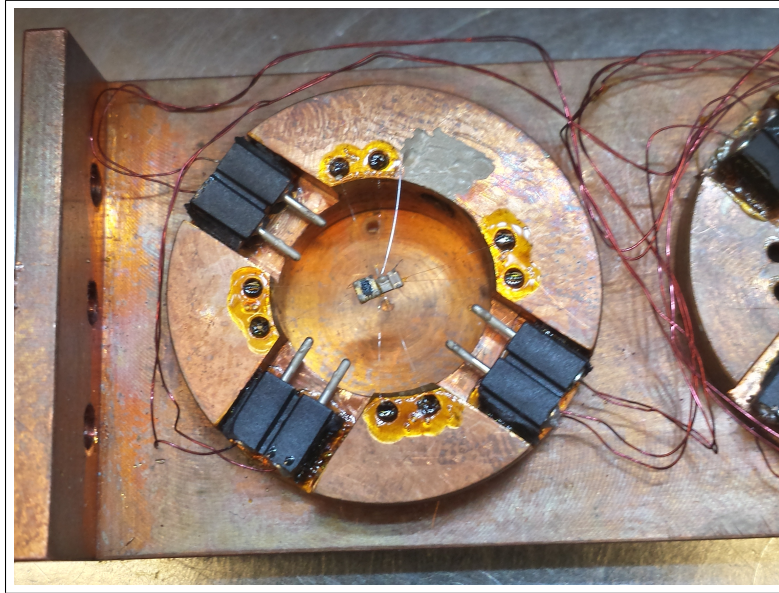
Figure A.4: The UPt$_3$ heat capacity measurement cell.

change in temperature of the sample was measured by measuring the resistance of the RuO$_2$ thermometer on the sample, and plugging it into a rough resistance to temperature calibration. The RuO$_2$ thermometer's resistance was measured using the 4-wire technique, where a 13 Hz current signal is provided by an SR830 lock-in amplifier with an amplitude of 1.2 V across a 100 $k\Omega$ resistor. The voltage was then measured using a low-noise pre-amplifier described in [7], which had a gain of 10000, and that signal was sent through a 1/500 voltage divider to the input of the SR830, measured in differential (A-B) mode. It was found that the noise of the setup was temperature independent and around 1.5 $\frac{nV}{\sqrt{Hz}}$, which was close to the spec of the noise on the preamplifier at the measurement frequency. Thus, the noise on the setup was very low, allowing for a very accurate heat capacity measurement. The raw data is shown below in Figure A.5 for a scan taken between 400 mK and 500 mK.

The fridge temperature is changed by 5 mK and the sample is allowed to equilibrate with the fridge over 2500 seconds before a heat pulse is applied. A polynomial fit is performed to the region just before the heat pulse is applied, which is used to extract the resistance value when the sample is in equilibrium with the fridge at the new temperature. Next a heat pulse is applied, and the RuO$_2$ thermometer is then calibrated on the fly against the very accurate Germanium resistance thermometer (GRT) on the sample stage using the extracted resistance value. The resulting calibration has the standard form for a
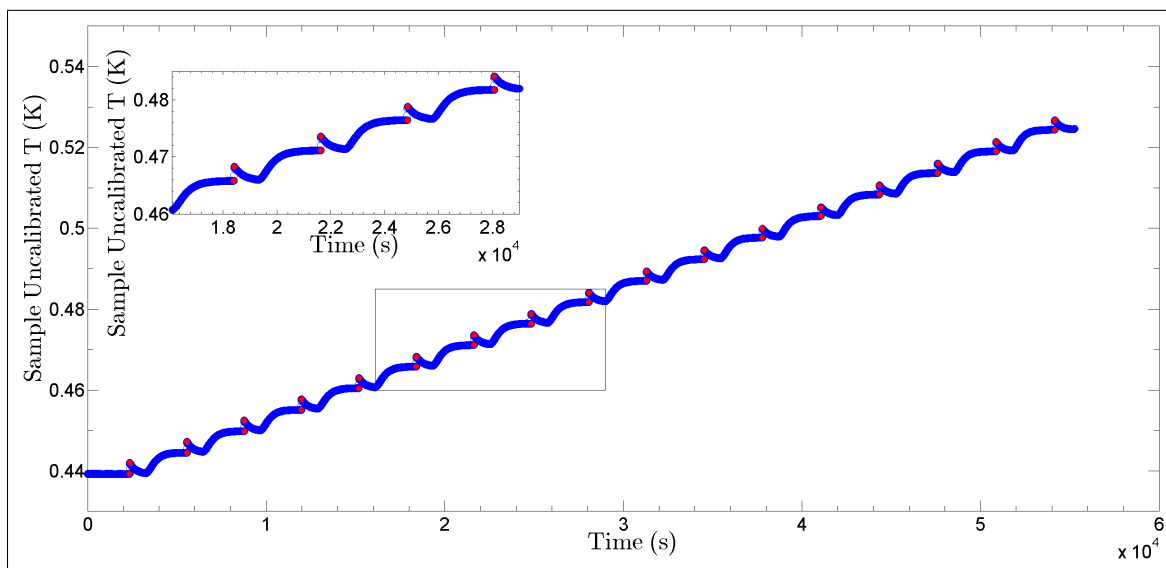
Figure A.5: The raw heat pulse data, with an uncalibrated sample temperature versus time.

RuO$_2$ thermometer, following from [45], namely Equation A.2. The resulting calibration for the data set of Figure A.5 is shown below in Figure A.6.

$$T = \sum_{i=0}^{3} A_i (ln(R))^i \tag{A.2}$$

Once the sample has equilibrated with the fridge, a heat pulse is applied over approximately 1 second (applied very accurately using the arbitrary waveform generator toolbox in Labview), which raises the samples temperature by approximately 3 mK. The heat is then turned off and the sample equilibrates with the fridge. The heat flows to the fridge through the weak link which has a time constant that ensures the sample is equilibrated with the applied heat. The relaxation between the sample and fridge when the heat is turned off is an exponential, and thus, an exponential is then fitted to the data after the heat pulse, and a polynomial is fit to the data before the pulse. They are then extrapolated to the half time of the pulse, which corrects for heat loss during application of the pulse. The polynomial fits to the data before the heat pulse, and the exponential fit to the data after the heat pulse are shown in Figure A.7 as black lines, as well as the resulting change in temperature ΔT, given as a green line. The heat capacity is also given in Figure A.7, calculated using the ΔT values and Equation A.1.

94

(a) On the fly calibration of the RuO$_2$ thermometer

(b) Calibrated sample temperature against fridge temperature
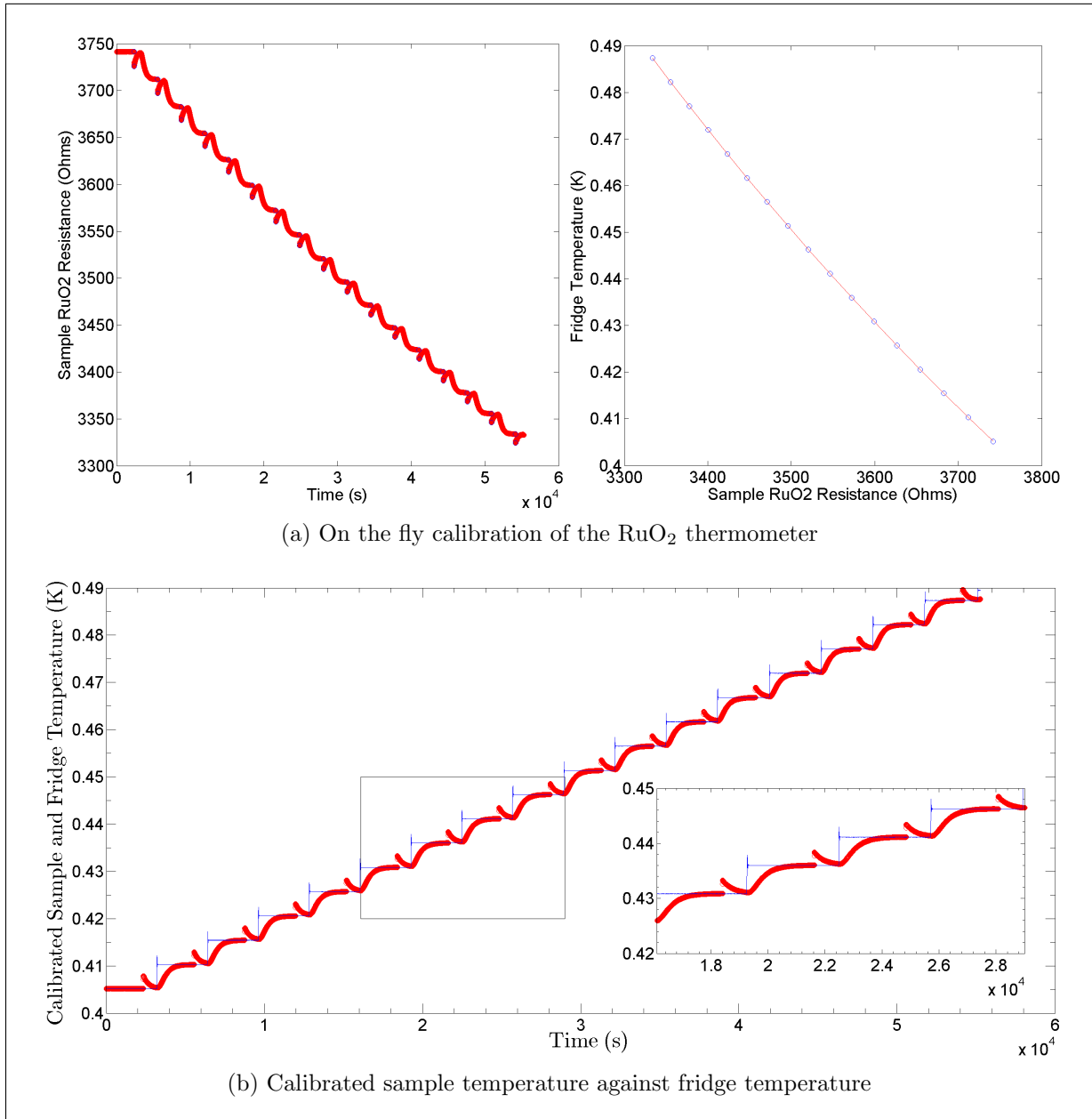
Figure A.6: On the fly calibration (a), and comparison of sample temperature against fridge temperature (b) for the data of Figure A.5 between 400 mK and 500 mK.

(a) Fits and the ΔT of the sample during a heat pulse

(b) Resulting heat capacity data using the ΔT of the above figure

Figure A.7: The change in temperature of the sample during a heat pulse (a), and the resulting heat capacity using the change in temperature data (b) for the data of Figure A.5 between 400 mK and 500 mK.

96

Reference	Annealing	T_c^-	T_c^+	ΔT_c	γ_N	$\Delta C^-/T_c^-$	$\Delta C^+/T_c^+$	ratio
Hasselbach et al. (1989)		434	490	56	0.45	0.10	0.21	0.48
Jin, Carter, et al. (1992)	950	464	515	51	0.41	0.12	0.24	0.50
Bogenberger et al. (1993)	1200	467	523	56	0.44	0.09	0.22	0.42
Brison et al. (1994b)	1200	480	530	50	0.44	0.12	0.23	0.52
Isaacs et al. (1995)	1230	460	510	50	0.44	0.11	0.23	0.48
Kimura et al. (1995)	1200	530	580	50	0.42	0.09	0.20	0.45
Taillefer, Ellman et al. (1997)		431	492	61	0.43	0.09	0.22	0.41
Kycia (1997)	900	495	545	50	(0.44)	0.13	0.25	0.52
This work (2015)	970	478±5	528±3	50±0.6	0.415±0.005	0.13±0.02	0.22±0.03	0.59±0.12

Table A.1: Table of various UPt$_3$ heat capacity results from [24], along with this measurement.

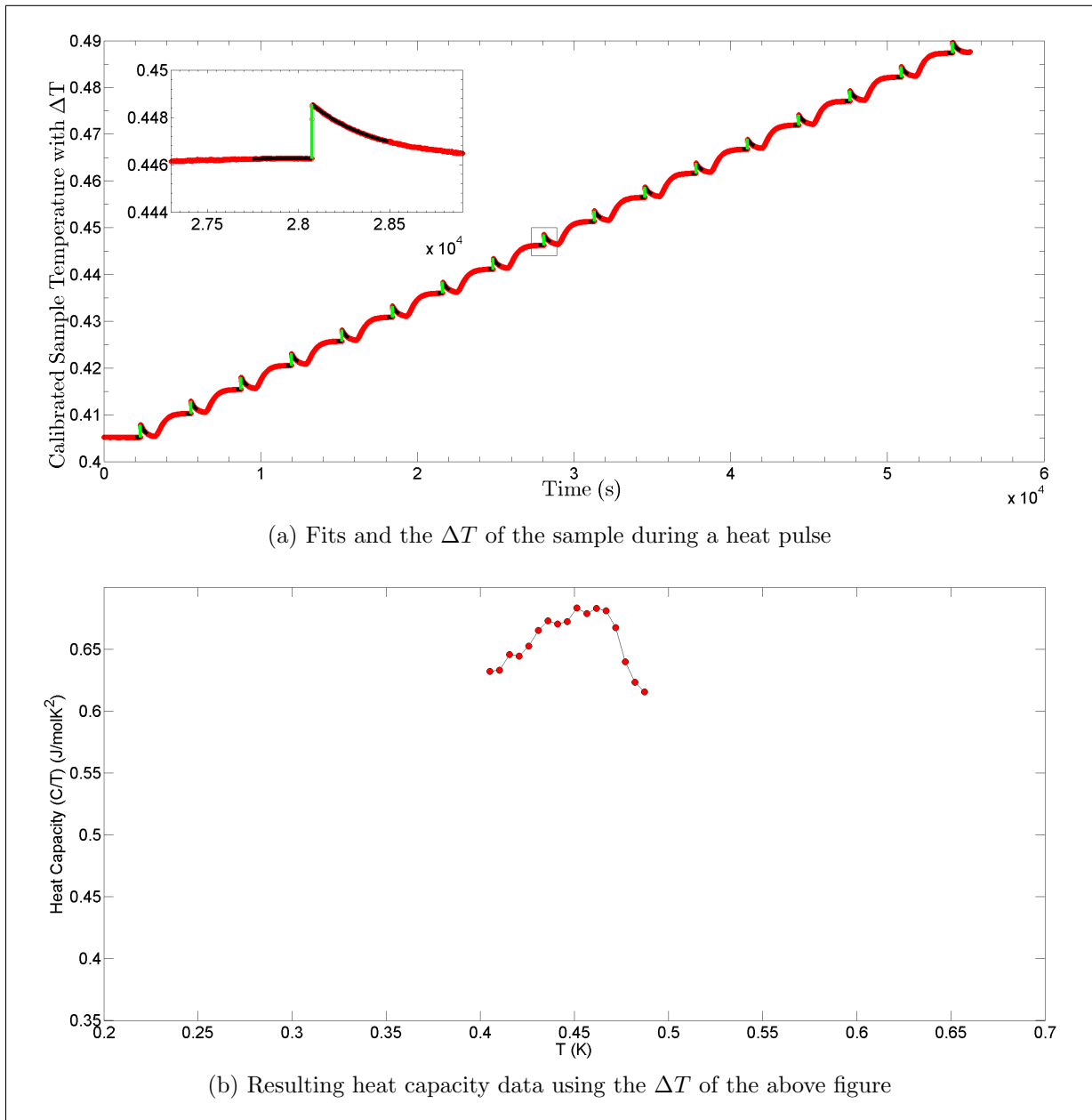The above describes how the data acquisition took place, and in Figure A.8, the specific heat data collected from 250 mK to 650 mK is shown. The data of Fisher [15] and Ott [42] is shown in Figure A.8 for comparison. As can be seen, the double superconducting transition was found for this crystal, with the expected shape in the expected temperature range. A number of important values can be obtained from this data, the fit to extract these values is shown in Figure A.9 and the results are summarized in Table A.1, compared to other works summarized in [24]. T_c^- and T_c^+ are the lower and upper transitions respectively. $\Delta C^-/T_c^-$ and $\Delta C^+/T_c^+$ are the heights of the specific heat jumps (in terms of C/T) at these two transitions, and their ratio is given. Below 1.5 K, UPt$_3$ is a Fermi liquid with a large effective mass, and so follows $C = \gamma_N T$, these are the γ_N values. The annealing temperatures for the various crystals are also shown in this table. As can be seen, the experimental values agree very well with previously measured UPt$_3$ crystals. As expected, the crystal has a high T_C^+ due to its purity. In addition to this, the region of the C/T curve after the double transition (between 250 mK to 450 mK) was fit to the form $\frac{C}{T} = \gamma_0 + aT$, and the parameters were found to be $\gamma_0 = 0.13$ and $a = 1.26$. As argued in [24], the fact that this portion of the heat capacity can be well fit to a T^3/T^2 shape is not a strict enough fit to distinguish between line nodes or point nodes in the gap, however the heights of the specific heat jumps suggest an anisotropic gap due to it deviating from the expected BCS theory value of $\frac{\Delta C(T_c)}{C(T_c)} = 1.43$. Overall, the data on this UPt$_3$ crystal is consistent with previously measured values, showing consistency with current models of superconductivity in UPt$_3$ based on specific heat data. The quality of the data shows the accurate specific heat data taking capabilities of the new dilution refrigerator setup.
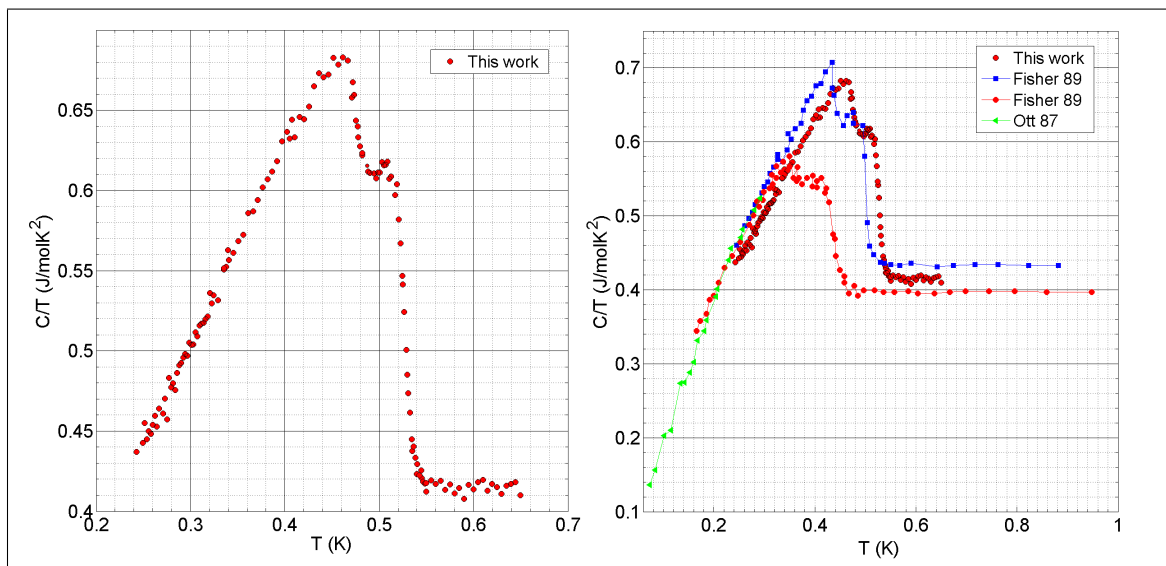
Figure A.8: Left figure: the specific heat of the ZR4 crystal annealed at 970°C. Right figure: the specific heat of this work alongside the work of [15] and [42].
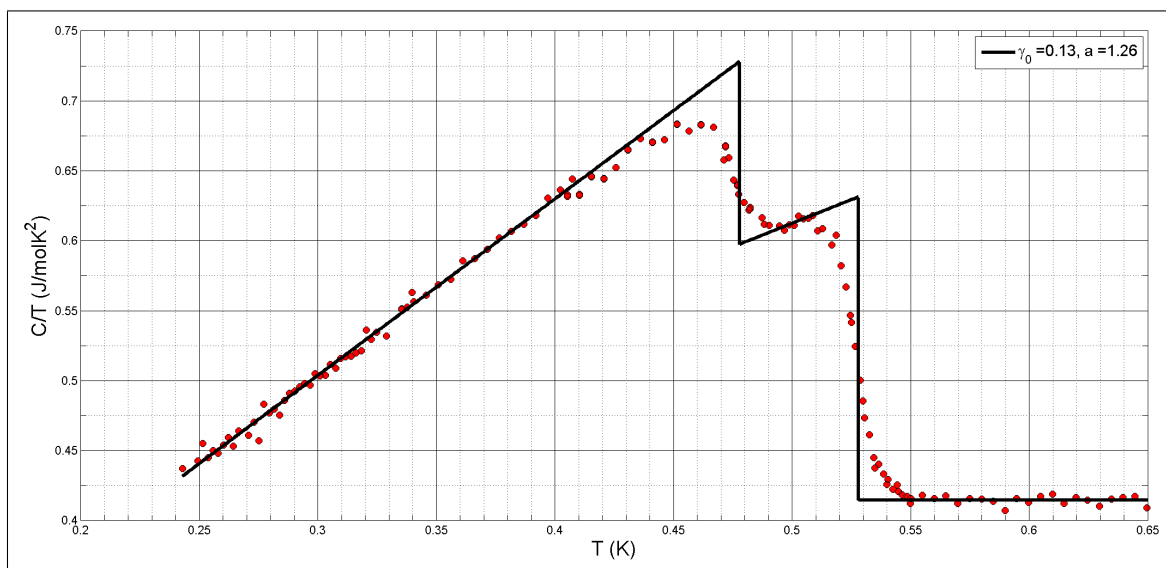

Figure A.9: The heat capacity curve analysis.

References

[1] S. Adenwalla, S. W. Lin, Q. Z. Ran, Z. Zhao, J. B. Ketterson, J. A. Sauls, L. Taillefer, D. G. Hinks, M. Levy, and Bimal K. Sarma. Phase diagram of upt_3 from ultrasonic velocity measurements. *Phys. Rev. Lett.*, 65:2298–2301, Oct 1990.

[2] Amikam Aharoni. Demagnetizing factors for rectangular ferromagnetic prisms. *Journal of Applied Physics*, 83(6), 1998.

[3] P. W. Anderson. Ordering and antiferromagnetism in ferrites. *Phys. Rev.*, 102:1008–1013, May 1956.

[4] Hidekazu Aoki, Toshiro Sakakibara, Kazuyuki Matsuhira, and Zenji Hiroi. Magnetocaloric effect study on the pyrochlore spin ice compound dy2ti2o7 in a [111] magnetic field. *Journal of the Physical Society of Japan*, 73(10):2851–2856, 2004.

[5] A. Biltmo and P. Henelius. Unreachable glass transition in dilute dipolar magnet. *Nat Commun*, 3:857, May 2012.

[6] S. T. Bramwell, M. J. Harris, B. C. den Hertog, M. J. P. Gingras, J. S. Gardner, D. F. McMorrow, A. R. Wildes, A. L. Cornelius, J. D. M. Champion, R. G. Melko, and T. Fennell. Spin correlations in $ho_2ti_2O_7$: A dipolar spin ice system. *Phys. Rev. Lett.*, 87:047205, Jul 2001.

[7] G. Cannata, G. Scandurra, and C. Ciofi. An ultralow noise preamplifier for low frequency noise measurements. *Rev.Sci.Instrum.*, 80, Nov 2009.

[8] J. Carrasquilla, Z. Hao, and R.G. Melko. A two dimensional spin liquid in quantum kagome ice. *Nat Commun*, 6, Jun 2015.

[9] C. Castelnovo, R. Moessner, and S. L. Sondhi. Debye-hückel theory for spin ice at low temperature. *Phys. Rev. B*, 84:144435, Oct 2011.

[10] C. Castelnovo, R. Moessner, and S.L. Sondhi. Magnetic monopoles in spin ice. *Nature*, 451, Jan 2008.

[11] Lei Chen, Wolfgang Wernsdorfer, Christos Lampropoulos, George Christou, and Irinel Chiorescu. On-chip squid measurements in the presence of high magnetic fields. *Nanotechnology*, 21(40):405504, 2010.

[12] John Clarke and Alex Braginski. *The SQUID Handbook: Applications of SQUIDS and SQUID systems*, volume 2. John Wiley and Sons, Incorporated, 2006.

[13] M F Collins and O A Petrenko. Review/synthse: Triangular antiferromagnets. *Canadian Journal of Physics*, 75(9):605–655, 1997.

[14] G Ehlers, A L Cornelius, M Orendc, M Kajnakov, T Fennell, S T Bramwell, and J S Gardner. Dynamical crossover in 'hot' spin ice. *Journal of Physics: Condensed Matter*, 15(2):L9, 2003.

[15] R. A. Fisher, S. Kim, B. F. Woodfield, N. E. Phillips, L. Taillefer, K. Hasselbach, J. Flouquet, A. L. Giorgi, and J. L. Smith. Specific heat of upt3: Evidence for unconventional superconductivity. *Phys. Rev. Lett.*, 62:1411–1414, Mar 1989.

[16] H. Fukazawa, R. G. Melko, R. Higashinaka, Y. Maeno, and M. J. P. Gingras. Magnetic anisotropy of the spin-ice compound $dy_2ti_2o_7$. *Phys. Rev. B*, 65:054410, Jan 2002.

[17] W. F. Giauque and J. W. Stout. The entropy of water and the third law of thermodynamics. the heat capacity of ice from 15 to 273k. *Journal of the American Chemical Society*, 58(7):1144–1150, 1936.

[18] S. R. Giblin, S. T. Bramwell, P. C. W. Holdsworth, D. Prabhakaran, and I. Terry. Creation and measurement of long-lived magnetic monopole currents in spin ice. *Nat Phys*, 7(3):252–258, Mar 2011.

[19] Michel J. P. Gingras. Spin ice, 2009.

[20] Matthias J. Graf, S.-K. Yip, and J. A. Sauls. Identification of the orbital pairing symmetry in upt_3. *Phys. Rev. B*, 62:14393–14402, Dec 2000.

[21] Zenji Hiroi, Kazuyuki Matsuhira, Seishi Takagi, Takashi Tayama, and Toshio Sakakibara. Specific heat of kagom ice in the pyrochlore oxide dy2ti2o7. *Journal of the Physical Society of Japan*, 72(2):411–418, 2003.

[22] Wayne R. Hudson and Russell J. Jirberg. Superconducting properties of niobium films. http://ntrs.nasa.gov/archive/nasa/casi.ntrs.nasa.gov/19710018646.pdf. Report No. NASA TN D-6380. Accessed: 2015-08-15.

[23] L D C Jaubert and P C W Holdsworth. Magnetic monopole dynamics in spin ice. *Journal of Physics: Condensed Matter*, 23(16):164222, 2011.

[24] Robert Joynt and Louis Taillefer. The superconducting phases of upt3. *Rev. Mod. Phys.*, 74:235–294, Mar 2002.

[25] Hiroaki Kadowaki, Naohiro Doi, Yuji Aoki, Yoshikazu Tabata, Taku J. Sato, Jeffrey W. Lynn, Kazuyuki Matsuhira, and Zenji Hiroi. Observation of magnetic monopoles in spin ice. *Journal of the Physical Society of Japan*, 78(10):103706, 2009.

[26] Ethan R. Kassner, Azar B. Eyvazov, Benjamin Pichler, Timothy J. S. Munsie, Hanna A. Dabkowska, Graeme M. Luke, and J. C. Samus Davis. Supercooled spin liquid state in the frustrated pyrochlore dy2ti2o7. *Proceedings of the National Academy of Sciences*, 112(28):8549–8554, 2015.

[27] B. Klemke, M. Meissner, P. Strehlow, K. Kiefer, S.A. Grigera, and D.A. Tennant. Thermal relaxation and heat transport in the spin ice material dy2ti2o7. *Journal of Low Temperature Physics*, 163(5-6):345–369, 2011.

[28] R. Kubo. The fluctuation-dissipation theorem. *Rep. on Prog. in Phys.*, 29:255–284, 1966.

[29] J.B. Kycia. *Growth and Characterization of high quality UPt3 single crystals and high resolution NMR study of superfluid 3He-B*. PhD thesis, NorthWestern University, Evanston, Illinois, 1997.

[30] Jaubert L.D.C. and P.C.W. Holdsworth. Signature of magnetic monopole and dirac string dynamics in spin ice. *Nat Phys*, 5:258–261, April 2009.

[31] E. Lhotel, C. Paulsen, P. Dalmas de Réotier, A. Yaouanc, C. Marin, and S. Vanishri. Low-temperature magnetization in geometrically frustrated tb$_2$ti$_2$o$_7$. *Phys. Rev. B*, 86:020410, Jul 2012.

[32] O.V. Lounasmaa. The he3/he4 dilution refrigerator. *Helvetica Physica Acta*, 41, 1968.

[33] Benoit Lussier, Brett Ellman, and Louis Taillefer. Determination of the gap structure in upt$_3$ by thermal conductivity. *Phys. Rev. B*, 53:5145–5148, Mar 1996.

[34] Y. Machida, A. Itoh, Y. So, K. Izawa, Y. Haga, E. Yamamoto, N. Kimura, Y. Onuki, Y. Tsutsumi, and K. Machida. Twofold spontaneous symmetry breaking in the heavy-fermion superconductor upt$_3$. *Phys. Rev. Lett.*, 108:157002, Apr 2012.

[35] K Matsuhira, Y Hinatsu, and T Sakakibara. Novel dynamical magnetic properties in the spin ice compound dy2 ti2 o7. *Journal of Physics: Condensed Matter*, 13(31):L737, 2001.

[36] Kazuyuki Matsuhira, Carley Paulsen, Elsa Lhotel, Chihiro Sekine, Zenji Hiroi, and Seishi Takagi. Spin dynamics at very low temperature in spin ice dy2ti2o7. *Journal of the Physical Society of Japan*, 80(12):123711, 2011.

[37] Roger G. Melko, Byron C. den Hertog, and Michel J. P. Gingras. Long-range order at low temperatures in dipolar spin ice. *Phys. Rev. Lett.*, 87:067203, Jul 2001.

[38] Roger G Melko and Michel J P Gingras. Monte carlo studies of the dipolar spin ice model. *Journal of Physics: Condensed Matter*, 16(43):R1277, 2004.

[39] Elena Mengotti, Laura J. Heyderman, Arantxa Fraile Rodriguez, Frithjof Nolting, Remo V. Hugli, and Hans-Benjamin Braun. Real-space observation of emergent magnetic monopoles and associated dirac strings in artificial kagome spin ice. *Nat Phys*, 7(1):68–74, Jan 2011.

[40] D. J. P. Morris, D. A. Tennant, S. A. Grigera, B. Klemke, C. Castelnovo, R. Moessner, C. Czternasty, M. Meissner, K. C. Rule, J.-U. Hoffmann, K. Kiefer, S. Gerischer, D. Slobinsky, and R. S. Perry. Dirac strings and magnetic monopoles in the spin ice dy2ti2o7. *Science*, 326(5951):411–414, 2009.

[41] Hiromi Otsuka, Hiroshi Takatsu, Kazuki Goto, and Hiroaki Kadowaki. Scaling ansatz for the ac magnetic response in two-dimensional spin ice. *Phys. Rev. B*, 90:144428, Oct 2014.

[42] H. R. Ott, E. Felder, A Bernasconi, Z. Fisk, J. L. Smith, L. Taillefer, and G. G. Lonzarich. Specific heat and thermal conductivity of superconducting ube 13 and upt 3 at very low temperatures. *Japanese Journal of Applied Physics*, 26(S3-2):1217, 1987.

[43] Linus Pauling. The structure and entropy of ice and of other crystals with some randomness of atomic arrangement. *Journal of the American Chemical Society*, 57(12):2680–2684, 1935.

[44] O. A. Petrenko, M. R. Lees, and G. Balakrishnan. Magnetization process in the spin-ice compound ho$_2$ti$_2$o$_7$. *Phys. Rev. B*, 68:012406, Jul 2003.

[45] Frank Pobell. *Matter and Methods at Low Temperatures.* Springer-Verlag Berlin Heidelberg, 3 edition, 2007.

[46] D. Pomaranski, L.R. Yaraskavitch, S. Meng, K.A. Ross, H.M.L. Noad, B. Dabkowska, B.D. Gaulin, and J.B. Kycia. Absence of pauling's residual entropy in thermally equilibrated dy2ti2o7. *Nat Phys*, 9, June 2013.

[47] J.A. Quilliam. Specific heat of the dilute, dipolar-coupled, ising magnet lihoxy1-xf4. Master's thesis, University of Waterloo, Waterloo Ontario, 2006.

[48] A. P. Ramirez, A. Hayashi, R. J. Cava, R. Siddharthan, and B. S. Shastry. Zero-point entropy in /'spin ice/'. *Nature*, 399, May 1999.

[49] H Revell. The low temperature magnetic relaxation of dy2ti2o7. Master's thesis, University of Waterloo, Waterloo Ontario, 2012.

[50] H. M. Revell, L. R. Yaraskavitch, J. D. Mason, K. A. Ross, H. M. L. Noad, H. A. Dabkowska, B. D. Gaulin, P. Henelius, and J. B. Kycia. Evidence of impurity and boundary effects on magnetic monopole dynamics in spin ice. *Nat Phys*, 9:34–37, Jan 2013.

[51] H. M. Revell, L. R. Yaraskavitch, J. D. Mason, K. A. Ross, H. M. L. Noad, H. A. Dabkowska, B. D. Gaulin, P. Henelius, and J. B. Kycia. Vacancy defects and monopole dynamics in oxygen-deficient pyrochlores. *Nat Mater*, 13:488–493, May 2014.

[52] Robert Richardson and Eric Smith. *Experimental Techniques in Condensed Matter Physics at Low Temperatures.* Addison-Wesley, 1998.

[53] Eugene I. Rivin. *Passive vibration isolation.* Amer Soc Mechanical Engineers, 2003.

[54] T. Sakakibara, T. Tayama, Z. Hiroi, K. Matsuhira, and S. Takagi. Observation of a liquid-gas-type transition in the pyrochlore spin ice compound dy$_2$ti$_2$o$_7$ in a magnetic field. *Phys. Rev. Lett.*, 90:207205, May 2003.

[55] E. R. Schemm, W. J. Gannon, C. M. Wishne, W. P. Halperin, and A. Kapitulnik. Observation of broken time-reversal symmetry in the heavy-fermion superconductor upt3. *Science*, 345(6193):190–193, 2014.

[56] J. Snyder, J.S. Slusky, R.J. Cava, and P. Schiffer. How 'spin ice' freezes. *Nature*, 413, Sep 2001.

[57] J. Snyder, B. G. Ueland, J. S. Slusky, H. Karunadasa, R. J. Cava, and P. Schiffer. Low-temperature spin freezing in the $dy_2ti_2o_7$ spin ice. *Phys. Rev. B*, 69:064414, Feb 2004.

[58] J. D. Strand, D. J. Bahr, D. J. Van Harlingen, J. P. Davis, W. J. Gannon, and W. P. Halperin. The transition between real and complex superconducting order parameter phases in upt3. *Science*, 328(5984):1368–1369, 2010.

[59] J. D. Strand, D. J. Van Harlingen, J. B. Kycia, and W. P. Halperin. Evidence for complex superconducting order parameter symmetry in the low-temperature phase of upt_3 from josephson interferometry. *Phys. Rev. Lett.*, 103:197002, Nov 2009.

[60] L. Taillefer, K. Behnia, K. Hasselbach, J. Flouquet, S.M. Hayden, and C. Vettier. On the superconducting phase transitions of upt3. *Journal of Magnetism and Magnetic Materials*, 9091:623 – 627, 1990.

[61] T. Trappmann, H. v. Löhneysen, and L. Taillefer. Pressure dependence of the superconducting phases in upt_3. *Phys. Rev. B*, 43:13714–13716, Jun 1991.

[62] G. H. Wannier. Antiferromagnetism. the triangular ising net. *Phys. Rev. B*, 7:5017–5017, Jun 1973.

[63] G. E. Watson, J. D. Reppy, and R. C. Richardson. Low-temperature density and solubility of he3 in liquid he4 under pressure. *Phys. Rev.*, 188:384–396, Dec 1969.

[64] L. R. Yaraskavitch, H. M. Revell, S. Meng, K. A. Ross, H. M. L. Noad, H. A. Dabkowska, B. D. Gaulin, and J. B. Kycia. Spin dynamics in the frozen state of the dipolar spin ice material $dy_2ti_2o_7$. *Phys. Rev. B*, 85:020410, Jan 2012.

[65] Luke Yaraskavitch. An experimental investigation of the spin dynamics of dipolar spin ice. Master's thesis, University of Waterloo, Waterloo Ontario, 2009.